Characterization of the thermo-viscoplastic behavior of a reinforced thermoplastic subjected to in-plane biaxial loading : application to heat assisted incremental forming

Joséphine Faddoul

To cite this version:

Joséphine Faddoul. Characterization of the thermo-viscoplastic behavior of a reinforced thermoplastic subjected to in-plane biaxial loading : application to heat assisted incremental forming. Mechanical engineering [physics.class-ph]. INSA de Rennes, 2023. English. NNT : 2023ISAR0030 . tel-04704059

HAL Id: tel-04704059
https://theses.hal.science/tel-04704059v1

Submitted on 20 Sep 2024

THESE DE DOCTORAT DE

L'INSTITUT NATIONAL DES SCIENCES
APPLIQUEES DE RENNES

ECOLE DOCTORALE N° 647
Sciences pour l'Ingénieur
Spécialité : *Génie Mécanique*

Par
« Joséphine FADDOUL »

« Characterization of the thermo-viscoplastic behavior of a reinforced thermoplastic subjected to in-plane biaxial loading: application to heat assisted incremental forming»

Thèse présentée et soutenue à Rennes, le 06/12/2023
Unité de recherche : Laboratoire de Génie Civil et Génie Mécanique (LGCGM), INSA Rennes
Thèse N° : 23ISAR 35 / D23 - 35

Rapporteurs avant soutenance :

Nadia BAHLOULI	Professeur, Université de Strasbourg
Abel CHEROUAT	Professeur, Université de Technologie de Troyes

Composition du Jury :

Présidente :	Nadine ALLANIC	Professeur, Nantes Université
Examinateurs :	Nadine ALLANIC	Professeur, Nantes Université
	Nadia BAHLOULI	Professeur, Université de Strasbourg
	Abel CHEROUAT	Professeur, Université de Technologie de Troyes
	Khaled KHALIL	Professeur, Université Libanaise
Dir. de thèse :	Lionel LEOTOING	Professeur, INSA Rennes
Co-dir. de thèse :	Pierre RAHME	Professeur, Université Libanaise

ACKNOWLEDGEMENT

I would like to express my sincere gratitude to all those who have contributed to the completion of this thesis. First and foremost, I am deeply thankful to my supervisors: Lionel Leotoing, Pierre Rahme and Dominique Guines for their invaluable guidance, support, and constructive feedback throughout the research process. Their expertise and encouragement have been essential in shaping the direction of this work. Additionally, I want to acknowledge the technical support received from the dedicated teams in the lab.

I am extremely grateful to my parents, my sister and my family for their continuous encouragement, love, and understanding during the ups and downs of this academic journey. Their support provided the emotional strength needed to persevere through the challenges. I also like to thank my Lebanese friends that I met in Rennes. Their companionship and constant support were a source of comfort when I felt alone. I am also grateful for my PhD colleagues with whom I shared the office. The talks and mutual support have made this journey more enjoyable.

RÉSUMÉ

Les thermoplastiques renforcés par des fibres présentent de bonnes propriétés mécaniques et une bonne aptitude à la recyclabilité. Néanmoins, la mise en forme de pièces complexes reste difficile. La mise en forme à chaud de ces matériaux est essentielle. La simulation par éléments finis des procédés est indispensable mais nécessite une caractérisation précise du matériau sous conditions réelles : chargement multiaxial avec grandes déformations, conditions variées de température et de vitesse de déformation. Les essais uniaxiaux classiques sont simples mais peuvent conduire à une caractérisation partielle du matériau sous chargement multiaxial. Les essais de traction biaxiale plane sur éprouvettes cruciformes permettent une caractérisation plus riche.

Ce travail vise à caractériser le comportement mécanique d'un polypropylène renforcé de fibres de verre discontinues pour différentes températures et vitesses de déformation. Le modèle modifié de G'Sell et Jonas, associé au critère anisotrope de Hill48, est calibré à partir d'essais de traction uniaxiale pour diverses conditions de température (jusqu'à 120°C) et de vitesse de déformation (jusqu'à 10 s^{-1}).

Les simulations numériques de l'essai biaxial, réalisées à partir d'un modèle de comportement calibré à partir des essais uniaxiaux, montrent un écart important avec les résultats expérimentaux. Il est donc nécessaire d'intégrer les résultats biaxiaux dans la procédure d'identification des paramètres rhéologiques du matériau, à partir d'une procédure d'analyse inverse. Finalement, les deux méthodes d'identification sont évaluées à partir de la prédiction des efforts de formage et de la forme finale d'une pièce formée par un procédé incrémental à chaud original.

ABSTRACT

Fiber reinforced thermoplastics offer good mechanical properties and the ability to be recycled. However, shaping complex parts remains challenging. Hot forming of these materials is crucial. Finite element simulation of processes is essential, but it requires accurate characterization of materials under real conditions: multiaxial loading with large deformations, varying temperature, and strain rates. Conventional uniaxial tests are simple but may lead to partial material characterization under multiaxial loading. In-plane biaxial tensile tests on cruciform specimens allow for a more comprehensive characterization.

This work aims to characterize the mechanical behavior of discontinuous glass fiber reinforced polypropylene at different temperatures and strain rates. The modified G'Sell and Jonas model, coupled with the anisotropic Hill48 criterion, is calibrated based on uniaxial tensile tests under various temperature conditions (up to 120°C) and deformation speeds (up to 10 s^{-1}).

Numerical simulations of the biaxial test, carried out using a behavior model calibrated from uniaxial tests, show a significant disagreement with the experimental results. Therefore, it is necessary to integrate biaxial results into the material's rheological parameter identification procedure through an inverse analysis process. Finally, both identification methods are evaluated based on the prediction of forming force and final geometry of a part formed using an original heat assisted forming process.

TABLE OF CONTENTS

LIST OF FIGURES

LIST OF TABLES

NOTATIONS

$\bar{\varepsilon}$	Equivalent strain
$\bar{\varepsilon}_p$	Equivalent plastic strain
$\dot{\bar{\varepsilon}}$	Equivalent strain rate
ε_i	principal strain component
$\bar{\sigma}$	Equivalent stress
σ_y	Yield stress
σ_{ult}	Ultimate tensile strength
E	Young's modulus
ν	Poisson's ratio
T	Temperature
RT	Room Temperature
GF/PP	Glass fiber reinforced polypropylene
DIC	Digital Image Correlation
HAISF	Heat-Assisted Incremental Sheet Forming

GENERAL INTRODUCTION

Fiber reinforced thermoplastics are widely recognized across various engineering applications, thanks to their good mechanical properties and recyclability. The challenge lies in shaping these materials into complex parts. Heat assisted forming emerges as an interesting approach to address this concern. As an attempt to minimize time-consuming and costly trial and error processes, Finite Element (FE) simulations have emerged as essential tools for analyzing the capabilities of sheet forming processes. To enhance the accuracy of FE models, it is essential to characterize the material behavior under actual operational conditions. In such scenarios, materials are typically subjected to biaxial loading states and exhibit significant deformations. Consequently, the identification of material constants associated with rheological models, particularly those accounting for temperature and strain rate dependencies, has become fundamental for the material characterization.

Biaxial tensile states can be achieved through various testing methods. One promising technique involves in-plane biaxial tensile tests using flat cruciform specimens. It involves the direct application of loads along perpendicular arms of the specimen. This technique offers several advantages. It is a frictionless test that doesn't involve any contact between the specimen and tools. Additionally, multiple strain paths can be followed, ranging from uniaxial stretching to equi-biaxial stretching. By adjusting the displacement ratio between the two perpendicular axes, various linear and nonlinear strain and stress states can be generated in the central region of the specimen. Nevertheless, the design of the cruciform specimen poses challenges. Over the years, there have been numerous efforts to enhance the design of cruciform specimens mainly for metallic alloys. The design optimization can be motivated by various applications, such as determining forming limit strains, calibrating anisotropic plastic yield criteria, and identifying hardening behavior for large strains.

This work aims to propose a calibration method of a phenomenological constitutive model to represent the temperature and strain rate dependent behavior of discontinuous glass fiber reinforced polypropylene. To achieve this goal, an experimental database is established, involving both conventional uniaxial tensile tests and in-plane equi-biaxial tensile tests conducted on flat cruciform specimens, for different temperatures and strain rates. Based on the experimental database, various calibration strategies are evaluated and discussed. The purpose is to define the best calibration technique by simulating a forming process using the identified model. The innovative Heat Assisted Incremental Sheet Forming (HAISF) process is tested in this work to form a fiber reinforced thermoplastic part. An experimental setup of the forming operation and a FE model are implemented to examine the effect of the material model and temperature on the forming force of the formed part.

The manuscript consists of four chapters, as outlined below:
Chapter 1 briefly discusses general characteristics and applications of fiber reinforced thermoplastic polymers. Main manufacturing techniques are also recalled. In addition, this chapter provides a brief overview of material models, covering both physical and phenomenological models, with particular emphasis on those that take into account the effect of temperature and strain rate. To establish a comprehensive base, various characterisation techniques and experimental test methods are reviewed, including both conventional and non-conventional approaches. The literature emphasises on the use of in-plane biaxial tensile test on cruciform specimens designed for polymer composites.

Chapter 2 presents the results of the uniaxial tensile tests carried out at different strain rates, quasi-static and intermediate (0.001/s, 1/s and 10/s). Each strain rate condition is tested for three different temperatures: room temperature (20°C), 70°C and 120°C. Anisotropy is examined by performing tests at room temperature along three orientations. The G'Sell and Jonas model, originally designed to describe the viscoplastic behaviour of semi-crystalline thermoplastics, is then adopted and modified on the basis of the empirical stress-strain results obtained at different strain rates and temperatures.

In Chapter 3, the mechanical behaviour of the material is characterized by a non-conventional testing technique involving in-plane biaxial tensile tests on a dedicated cruciform specimen. The choice of this specimen geometry is based on a previous work conducted by the team on metallic alloys. This chapter checks the applicability of the material model identified in Chapter 2 (based on the uniaxial tensile tests database) by simulating the in-plane biaxial tensile tests. Significant differences between experimental and numerical results (temporal evolution of principal strains) require re-evaluation of the material parameters. This involves incorporating the results of in-plane biaxial tests into the identification process using the inverse analysis approach based on the Finite Element

Model Update (FEMU) method.

Chapter 4 focuses on the practical application of the identified models in the simulation of heat-assisted incremental forming of glass fiber reinforced polypropylene plate. The forming operation is applied experimentally to form a truncated cone under specific operating conditions. For the numerical approach, a FE model is established for a parametric study to investigate the effect of the constitutive behavior law and temperature on the forming force, thickness variation and final geometry. Finally, the experimental results are compared with the numerical results. This comparative analysis is used to discuss the reliability of the phenomenological model. It is associated with the proposed identification procedure to accurately predict the complex thermo-mechanical interactions that occur during heat-assisted incremental sheet forming.

Chapter 1

STATE OF THE ART

1.1 Introduction

The good mechanical properties of composite materials, in particular the strength-to-weight ratio, have driven them into new fields. They offer a promising solution to address the environmental and economic challenges associated with transportation (limitation of greenhouse gas emissions and fuel efficiency). The aerospace industry has been progressively incorporating composite materials into its designs. As an example, Figure 1.1 shows the high content (more than 50%) of carbon fiber reinforced polymers used in Airbus A350 [1].

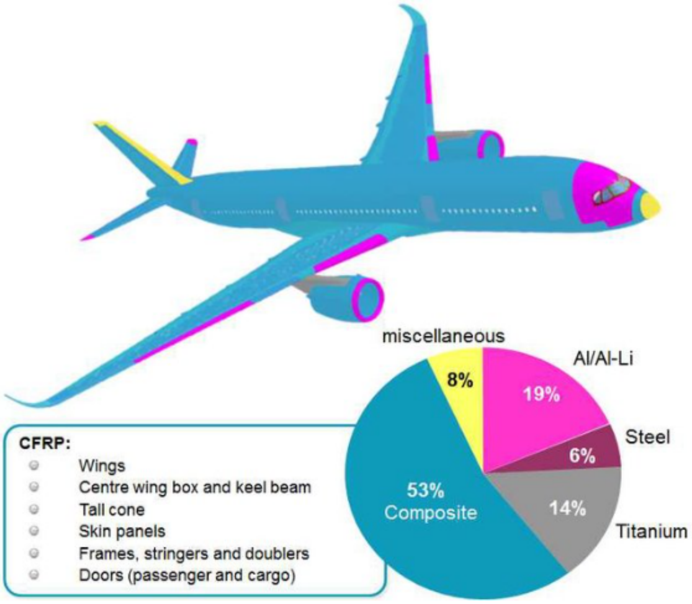

Figure 1.1: Distribution of materials in Airbus A350 XWB [1]

Additional characteristics, including effective vibration absorption, durability against fatigue, capacity to withstand extreme temperatures, corrosion resistance, and resilience against wear, are particularly valuable within industrial environments. These attributes significantly contribute to the reduction of product life cycle expenses [2].

What sets composites apart from traditional materials is their composition, which consists of two distinct components: reinforcements and a matrix material. When these components are combined, they create a new material. Importantly, the properties of the resulting composite cannot be predicted by summing up the properties of its individual components [2]. Composites exhibit anisotropic properties in which reinforcements can be adapted in specific orientations to provide the best mechanical properties along the loading direction.

1.2 Types of composite materials

Composite materials may be classified according to the matrix material or the reinforcement (Figure 1.2). The matrix can be polymeric, ceramic or metal ([3], [4]). Its role is to bind the reinforcements, give the composite its shape and guarantee its surface quality. Fibers are the most common type of reinforcements which enhance the overall mechanical characteristics of the matrix [4]. They usually come in two main forms: discontinuous or continuous, while their distribution can be different according to the desired application-randomly oriented discontinuous fibers, randomly oriented continuous fibers, unidirectional continuous fibers and bi-directional fabric [5].

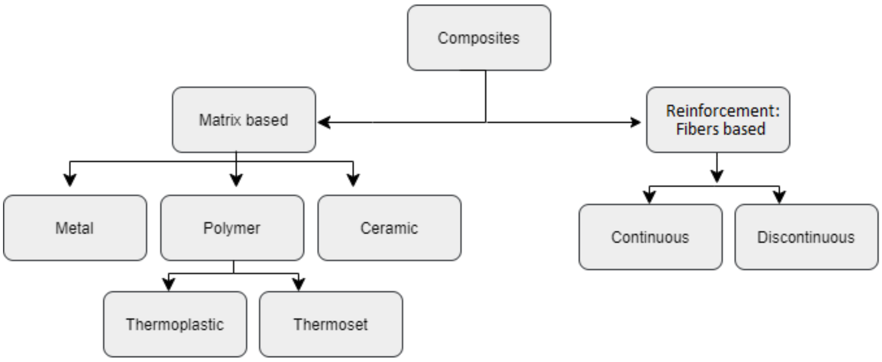

Figure 1.2: Types of composite materials

Polymer matrix composites (PMCs) are the most common in the market since lightweight is an important feature of polymers. These materials are nowadays introduced into many sectors such as automotive, aerospace, marine, mechanical structures, sports, construction, military equipment and many more [6]. PMCs consist of thermoplastic (polyamide, polypropylene, polysulfone, polyimide...) or thermoset (polyester, vinyl ester, polybutadiene, epoxy, amino, phenol...) polymers as a matrix with fiber reinforcements, such as carbon, glass, kevlar, polymeric or natural fibers ([4], [6]).

1.2.1 Thermoset composites

Thermoset composites are nowadays considered as alternatives for traditional metallic materials. They are primarily employed in aircrafts, wind turbines, as well as in military and defense [7]. They primarily include epoxies, polyurethanes, silicones, and polyesters. Epoxy-based composites are considered as high-performance engineering materials [7]. Polyester composites on the other hand, are known for their wide distribution but are attributed to lower or limited performance applications compared to epoxies ([8], [9]).

Thermoset composites can be thermally or chemically hardened. The resin is initially soft and mobile until cured with a cross-linking reaction (polymerisation) [4]. The resulting composite is characterized by its high rigidity and elevated strength to weight ratio. However, such material is known to be extremely brittle with low impact-toughness [10]. Moreover, the curing phase is irreversible which means that the composite cannot be remolded or reshaped. Consequently, the recyclability of this type of material is very difficult, which doesn't align with the latest environmental regulations. These limitations can potentially be avoided by substituting the thermoset resin with a thermoplastic matrix.

1.2.2 Thermoplastic composites

Contrarily to thermosets, thermoplastic composites are known to become flexible at high temperatures and solid upon cooling [11]. Additionally, no further chemical reactions are necessary to achieve the full mechanical properties of the polymer. The part becomes consolidated by simply heating, melting and cooling the material under a certain degree of contact pressure enough to achieve crystallinity. Thermoplastic composites have a relatively good strength to weight ratio. They are also known for their good chemical and impact resistance. They offer greater design flexibility where it is possible to reprocess failures within the composite part by repeat moulding procedures making the composite material fully recyclable ([12], [13]). The reduction in production cycle times also favours thermoplastic composites over thermosets.

While thermoset composites continue to hold a dominant position in various sectors (automotive, aerospace, transportation, construction...), there's a rapid expansion of applications involving thermoplastic composites. These emerging applications are providing new solutions to the previously mentioned limitations associated with the use of thermoset composites. The aircraft industry is currently undergoing a transition, shifting from the use of metal components to reinforced plastics, and from employing thermoset materials to utilizing thermoplastic matrices [14]. The leading edges of Airbus wings are constructed using glass fiber reinforced polyphenylene sulfide (PPS) materials. This innovation was initially introduced on the A340 series. Subsequently, on the A380, the entire wingspan leading edges transitioned to PPS, replacing what used to be a riveted aluminum component. This shift represents a significant change, especially considering that it is a critical and load-bearing component. The "Verified Market Research" determined growth factors for thermoplastic composites which is expected to grow at a Compound Annual Growth Rate (CAGR) of 7.7% from 2022 to 2030 [15]. This means that the market demands for thermoplastic composites is increasing over the years and is rapidly growing compared to thermosets.

1.3 Discontinuous fiber reinforced thermoplastic polymers

The challenge in producing continuous fiber reinforced thermoplastics comes from the notably high viscosity of liquid thermoplastics. In contrast, continuous fibers are typically integrated into thermoset polymers while the polymers are in a low-viscosity state, which subsequently solidifies through a chemical reaction. Liquid thermoplastics, on the other hand, possess viscosities that are several orders of magnitude higher than those of liquid thermosets. This high viscosity makes it difficult to impregnate the fiber bundles and ensure proper wetting of the fibers. As a result, the use of randomly dispersed discontinuous fibers in thermoplastics is common, as they can be processed using conventional injection molding techniques.

The mechanical properties of discontinuous fiber reinforced thermoplastics are indeed inferior to those of continuous fiber reinforced thermoplastics (lower strength and modulus). However, they are still sufficiently robust for a wide range of applications. In the automo-

tive sector for instance, the application of these composites is found in the seat structures of the car, door modules, dashboard carriers, front end modules and bumper beams ([5], [16]).
Generally, the matrix material significantly influences the overall performance of a thermoplastic composite. Subsequently, the following sections offer a brief overview of the fundamental characteristics of thermoplastic polymers, discuss the factors influencing their behavior, and examine how these factors affect the behavior of the resulting composites. Additionally, some of the techniques used in the manufacturing of these types of composites are addressed.

1.3.1 General characteristics of thermoplastic polymers

When heat is applied to thermoplastic polymers, they soften or melt and they can be processed whether they are in a heat-softened state (thermoforming) or in a melted state (injection molding). Contrary to thermosets, new products can be processed by means of heat application and recycling. However, repeatedly recycling thermoplastic parts causes some of the mechanical properties to deteriorate. Thermoplastic polymers can be classified in terms of performance in a “polymer performance pyramid” as commodity, engineering and high performance thermoplastics, with the latter being on top of the pyramid shown in Figure 1.3. Two categories are shown in this pyramid: amorphous (ABS, polystyrene, polycarbonate...) and semi-crystalline (Polypropylene, High density polyethylene...). Semi-crystalline materials possess a well-organized molecular structure characterized by distinct melting points. Unlike materials that gradually soften with rising temperatures, they maintain their solid state until they absorb a specific amount of heat, at which point they swiftly transition into a low-viscosity liquid. These materials exhibit anisotropic flow behavior, contracting less along the direction of flow compared to the transverse direction. Moreover, they demonstrate remarkable resistance to chemical degradation. When reinforced, semi-crystalline materials maintain noteworthy levels of strength and stiffness well beyond their glass transition temperature (T_g) ([17], [18]). On the other hand, amorphous polymers possess a molecular structure that lacks ordered patterns, and they do not exhibit a distinct melting point. Instead, they undergo a gradual softening process as temperature increases. They experience a rapid decrease in strength once they exceed their T_g [17]. When heated, these materials undergo a change in viscosity, but they generally do not flow as easily as semi-crystalline materials. They display isotropic flow behavior, meaning they uniformly shrink both in the direction of flow and transverse to it. Consequently, amorphous materials typically experience reduced mold shrinkage and demonstrate a lower tendency to warp compared to semi-crystalline counterparts [18].

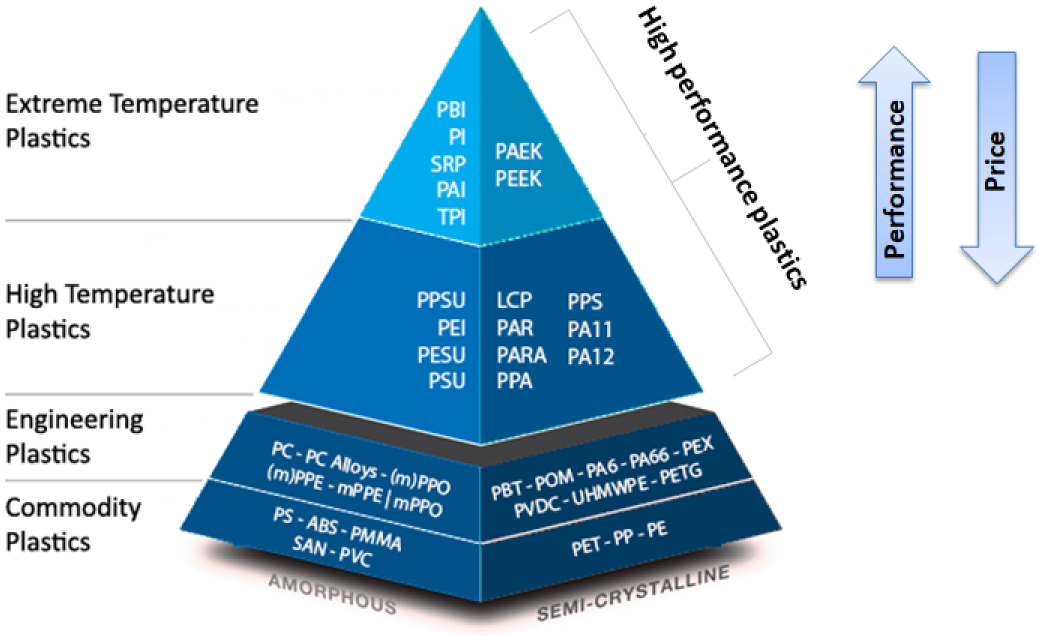

Figure 1.3: Performance pyramid of thermoplastic polymers [19]

1.3.2 Factors affecting the behavior of thermoplastic polymers and their corresponding composites

In general, the behavior of a polymer, particularly a thermoplastic, is primarily influenced by temperature and strain rate. Additionally, several other factors can play a role in controlling the material's response. These factors include the type of loading (tension, compression, shear...), the thermomechanical conditions to which it was exposed during the fabrication process, and environmental variables like humidity, which can be especially relevant for hydrophilic polymers [20]. It's noteworthy that thermoplastic polymers may not be sensible to all of these factors in the same proportions. However, this polymer sensitivity to the aforementioned factors will undoubtedly manifest in the overall behavior of the corresponding fiber reinforced thermoplastic ([21], [22]). Atmani et al. [22] performed an experimental and numerical study to describe the behavior of an unreinforced thermoplastic polymer (high impact polystyrene HIPS) during plug-assisted thermoforming. In the experimental part of their study, they investigated the elastic properties by performing uniaxial tensile tests at different temperatures, from 80°C to 140°C, and at three different strain rates: $0.0167s^{-1}$, $0.033s^{-1}$, and $0.167s^{-1}$. They noticed that the elastic modulus and the yield strength increased by 67% and 50%, respectively, as the strain rate increased by a factor of 10. Moreover, a temperature increment of 20°C at the lowest strain rate, caused a decrease in the values of Young's modulus and yield strength by 67% and 54%, respectively. Furthermore, Wang et al. [23], studied the effect of temperature (ranging from 21°C to 100°C) and strain rate (0.05 min^{-1}, 0.5 min^{-1}, 5 min^{-1}) on the mechanical behavior of short glass fiber reinforced polyamide-6. They concluded that increasing the strain rate by a factor of 100 at a temperature of 21°C, induces an increase of 16% and 18% for both Young's modulus and tensile strength, respectively. Whereas, an elevation of temperature from 21°C to 100°C causes a decrease of 75% in Young's modulus and 43% in the tensile strength. Duan et al. [24], investigated the effect of uniaxial strain rate on the mechanical properties of glass fiber reinforced polypropylene at RT. They showed that increasing the strain rate from $0.001s^{-1}$ to $50s^{-1}$ increases the ultimate tensile strength by 84% while having a negligible effect on Young's modulus. Similarly, Cui et al. [25], studied the tensile behavior of long glass fiber reinforced polypropylene at RT for strain rates ranging between $0.001s^{-1}$ and $400s^{-1}$. Results showed that the ultimate strength, fracture strain, and Young's modulus increase with the strain rate. The study of Yu and Ma [26] investigated the influence of loading rate and temperature on the static flexural modulus and strength of discontinuous glass fiber reinforced polypropylene composite. The authors performed three-point bending tests for unreinforced polypropylene as well as for the composite. Results showed that whether considering polypropylene alone or polypropylene composite, the flexural modulus and strength tend to rise as the loading rate increases from 0.1 mm/min to 10 mm/min. Conversely, these properties tend to decrease as the experimental temperature is raised from 25°C to 100°C.

Another important factor that has an impact on the mechanical behavior of discontinuous fiber reinforced polymers is the properties of fibers (concentration, length, orientation). Thomason [27] examined the performance and mechanical characteristics of injection-molded polypropylene reinforced with long glass fibers with fiber content ranging from 0% to 73% by weight. The results revealed that the composite modulus experienced a linear rise in correlation with the fiber volume fraction throughout the entire range under investigation. However, the behaviors of strength and impact performance displayed non-linear relationships with the fiber content.

1.3.3 Manufacturing techniques of FRPs

Various methods exist for the production of PMCs. The choice of the processing technique depends on the material's properties and intended applications. Figure 1.4 presents different manufacturing techniques applied for both thermosetting and thermoplastic matrix composites. Some techniques are suitable for one category (thermoset comosites) but may not be very well adapted for the other (thermoplastic composites). Processing thermoplastic composites can take place in a matter of seconds and is considered as an entirely physical operation since no chemical reaction is involved as in the case of thermosets.

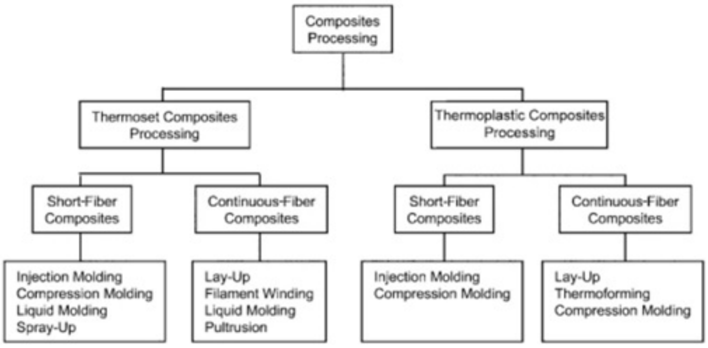

Figure 1.4: Common manufacturing techniques of composites [28]

The predominant thermoplastic manufacturing techniques include injection molding, compression molding, and thermoforming. In the following subsections, the well known manufacturing techniques will be briefly discussed.

1.3.3.1 Injection molding

Injection molding is very common manufacturing technique used to form thermoplastics and fiber reinforced thermoplastics. The initial composite used in this process comes in the form of pellets or granules. Generally, glass fibers are used with various thermoplastic matrices such as Polypropylene, Polyamide-6, Polyethylene therephtalate... Pellets with carbon and Kevlar fibers are also available. The basic principle of injection molded is represented in Figure 1.5. The melted material is pressurized and pushed towards the mold via a screw. When the part is cooled down to below glass transition temperature (for amorphous polymers) or melt temperature (for semi-crystalline polymers), the mold opens and the product is removed. Cycle times can range from 10 to 100s and are mainly controlled by the cooling time [29], [30]. Usually, minimal post-production work is neces-

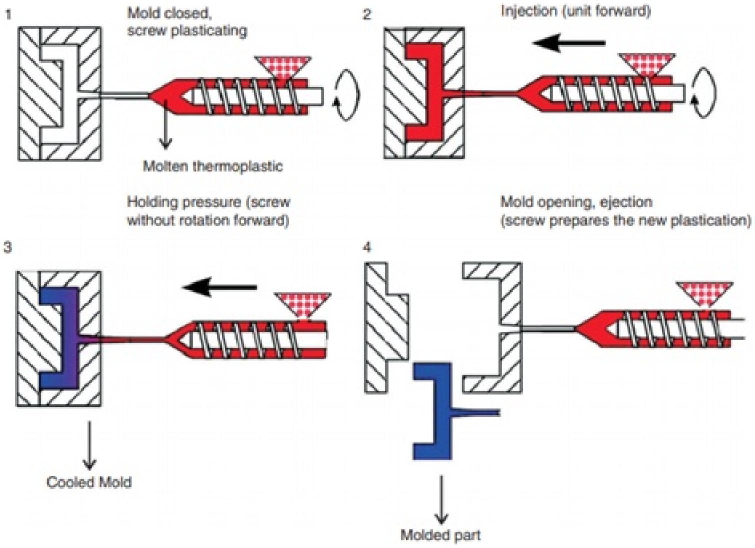

Figure 1.5: Processing of injection molding for thermoplastic composites [29]

sary because parts typically have a highly finished appearance once they are ejected from the mold. Injection molding is used to manufacture a wide range of fiber reinforced parts with good physical and mechanical properties, in large quantities for diverse applications across industries. These include the aerospace industry, automotive sector (for components like air intake manifolds, rocker covers, and cooling modules), electrical and electronic industries (especially for connectors), medical and dental product manufacturing (including components for blood analyzer equipment, heart pump parts, and orthopedic devices), as well as household appliances [30].

1.3.3.2 Compression molding

Compression molding is a manufacturing process used to shape thermoplastic or thermosetting materials into specific forms using heat and pressure. In the context of fiber reinforced thermoplastic polymers, this method involves placing the composite material between two heated mold halves. The mold is then closed, and pressure and heat are applied to consolidate the material. The heat causes the thermoplastic polymer to melt and bond with the reinforcing fibers, resulting in a solid and strong composite part [31]. Figure 1.6 shows a schematic of the compression molding process. Cycle times typically range from 30 to 60s. The Key points about compression molding are: i) high-pressure process, ii) the material is typically heated above the melting point of the thermoplastic

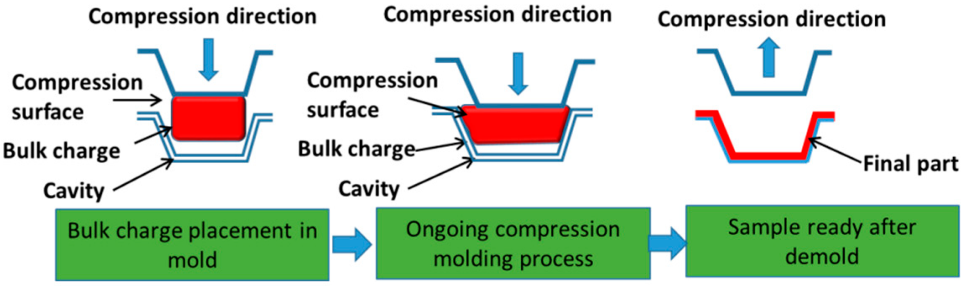

Figure 1.6: Schematic of compression molding [31]

matrix, and iii) the final part tends to have good mechanical properties. However, intermediate surface finish is obtained (imperfections such as pits and wrinkles). Furthermore, due to the high viscosity of the polymer, a typical fiber volume fraction between 20% and 30% is used. This technique is for high production rates and is used in the industry to manufacture structural thermoplastic composite parts such as bumper beams, dashboards and other automotive structural components [29].

1.3.3.3 Thermoforming/ Thermostamping

The main difference between compression molding and thermoforming of fiber reinforced thermoplastic polymers lies in the process itself. As compression molding involves melting the thermoplastic and consolidating it under high pressure , thermoforming, on the other hand, relies on heating the material below its melting point and using vacuum or pressure. Figure 1.7 shows the principle of thermostamping which consists in applying pressure to force the flat plate into the die to shape it. This technique is more suitable for larger and less structurally demanding parts. The fibers in the preform can be discontinuous or continuous, in a random orientation, aligned in one direction, or in a structured textile. Both thermoset and thermoplastic can be used as matrices. However, thermostamping is generally better suited for thermoplastic composites due to their ability to be reprocessed and molded with relative ease.

Relatively complex shapes can be achieved by such a thermoforming process, as demonstrated by the stiffener ribs manufactured for a wing leading edge designed and built by Fokker Aerostructures, thanks to the good drapeability of the woven structure of the reinforcing glass fibres [33].

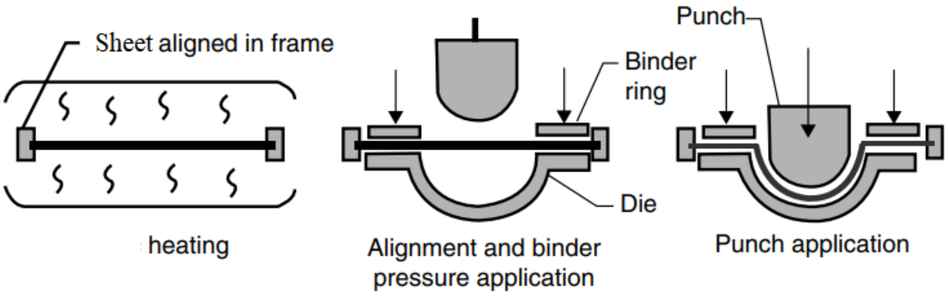

Figure 1.7: Thermostamping process [32]

1.3.3.4 Innovative processes

In the context of fiber reinforced polymers, it's worth noting that innovative manufacturing techniques are still in the early stages of research and have yet to achieve widespread adoption. Among these emerging techniques, one that deserves special attention, which is Incremental Sheet Forming (ISF). It is a dieless manufacturing process characterized by the tool's controlled movement along a predetermined path. Using a CNC technology, the tool shapes the part through localized deformation, layer by layer. The principle of this process is illustrated in Figure 1.8. This approach relies on computer-aided design models and CNC codes to shape a variety of parts with diverse geometries. The ISF not only conserves energy but can also be interesting for the manufacturing of complex parts in small quantities, as in the domain of prototyping. This technique can also involve the application of heat in conjunction with incremental sheet forming processes. By providing controlled heat, this method seeks to enhance material formability, potentially offering

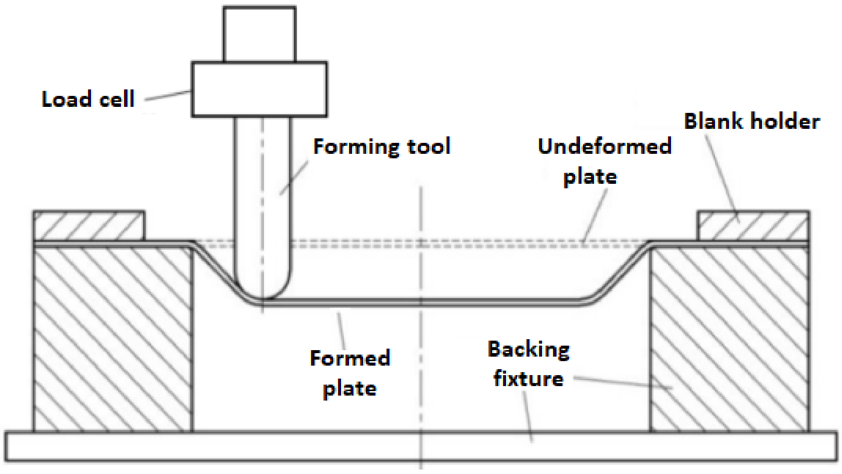

Figure 1.8: Incremental Sheet Forming principle [34]

a new dimension to the manufacturing possibilities for fiber-reinforced polymers. However, due to its complex nature, more investigation and validation are needed to check its practical viability and potential advantages.

1.4 Modeling and mechanical characterization of thermoplastic composites

It is essential to optimize the previously-described manufacturing techniques of fiber reinforced thermoplastics. This necessitates the establishment of predictive models and numerical tools that align with the specific process conditions (particularly temperature and strain rate). Modeling serves the purpose of describing the mechanical behavior of these materials, enabling the development of predictive models and providing essential inputs to simulation codes. In the following sections, the focus will be on the material models and characterization techniques that can be employed to assess the behavior of FRPs.

1.4.1 Material models

Material models used to predict the mechanical behavior of fiber reinforced composites must include material-related mechanical characteristics, such as non linear visco-elasticity and plasticity along with strain rate and temperature dependency.

Material modeling can generally be divided into physical (micro-mechanical) and phenomenological approaches. The choice between both approaches depends on the specific goals of the analysis, the level of detail required, the availability of data, and the computational resources available. Using physical modeling, individual fiber behavior and matrix properties along with their fractional physical composition are assessed in order to predict the overall performance of a composite from a micro-mechanical level. Sometimes, the physical methods are unable to fully capture, for example, complex fiber interactions and fiber-matrix interface properties. This makes such models idealized versions of the actual mechanical characteristics. On the other hand, phenomenological approaches can describe the overall composite behavior without specifically examining the constituents. Generally, using such approaches makes it more practical to model the mechanical behavior of a heterogeneous material over a wide range of temperatures and strain rates.

The following sections review some physical as well as phenomenological material models used to predict the mechanical behavior of fiber reinforced polymer composites.

1.4.1.1 Physical models

As mentioned previously, the behavior of composites can be predicted using physical models which offer fundamental understanding of deformation mechanisms at the micro-scale level. This approach doesn't require extensive experimental testing to characterize the behavior at the macro-scale (overall composite behavior). However, it requires deep understanding of the properties for each of the constituents i.e. characteristics of the matrix; orientation, distribution and length of fibers; volume fractions; fibers/matrix interface; void content...[35]. The majority of models developed by researchers are based on analytical homogenization approaches. Some of them will be shortly reviewed.

Rule of mixture (ROM) The most straightforward homogenization technique is the ROM, wherein the homogenized property of the material, P (equation 1.1) , is formulated as a weighted sum of the associated properties (Young's modulus, Poisson's ratio, shear modulus, Bulk modulus, ultimate tensile strength, mass density, thermal conductivity...) of the constituents comprising the material. i.e. matrix and fibers [36].

$$P = V_m P_m + V_f P_f \tag{1.1}$$

Here, the indices m and f refer to the matrix and reinforcement components of the polymer, and V represents the corresponding volume fraction. The inverse of this rule (IROM) can also be applied as:

$$\frac{1}{P} = \frac{V_m}{P_m} + \frac{V_f}{P_f} \tag{1.2}$$

Researchers have employed the ROM principle in their proposed models to predict the elastic properties of fiber reinforced polymer composites. In the study of Joseph et al.[37], the authors predicted the tensile properties of discontinuous sisal fiber reinforced polypropylene composite using ROM based models. After comparing the predicted properties with the experimental results, they found that the prediction was accurate at lower fiber volume fractions but not at higher fibre volume fractions.

Halpin Tsai model The Halpin-Tsai equations [38][39] are extensively used for predicting the elastic properties of discontinuous short fiber composites, more precisely those characterized by an ideal fiber alignment. The property P of the composite can be represented by the following equation:

$$\frac{P}{P_m} = \frac{1 + \eta\zeta V_f}{1 - \eta V_f} \text{ with } \eta = \frac{(P_f/P_m) - 1}{(P_f/P_m) + \zeta} \tag{1.3}$$

with ζ being a parameter that depends on the geometry of the reinforcement. The model can be modified to accommodate for the randomly oriented discontinuous fiber reinforced composites. The equations are detailed in [40]. For instance, Osaka et al.[41] modified the Halpin-Tsai model to predict the elastic modulus of a randomly oriented short natural fiber reinforced thermoset (polyester and epoxy) composites.

Mori-Tanaka-Benveniste model Bevenist [42] relied on the Mori–Tanaka formulation [43] to predict the effective elastic modulus, denoted as C, for a composite featuring randomly dispersed linear fibers. The formulation of C is defined as:

$$C = (V_m C_m + V_f C_f A)\,(V_m I + V_f \langle A\rangle)^{-1} \tag{1.4}$$

Where I represents the fourth-order identity tensor. The Mori-Tanaka strain-concentration tensor $\langle A\rangle$ is defined as follows:

$$\langle A\rangle = \left[I + S\,(C_m)^{-1}\,(C_f - C_m)\right]^{-1} \tag{1.5}$$

Where S stands for the Eshelby tensor [44].
Additional details on the equations and derivations can also be found in [45]. Many studies investigated the micro-mechanical behavior of fiber reinforced polymers while relying on the Mori-Tanaka approach. Nachtane et al. [46] included the Mori-Tanaka scheme in their modeling approach to predict the flexural stress and stiffness of discontinuous randomly oriented glass fiber Polyamide-6. The experimental results agreed well with the predicted values.

Bridging model The bridging model [47], [48] was designed to predict the behavior of continuous fiber reinforced composites. It's simple and straightforward to implement, especially for composites subjected to planar loading conditions, and requires no iteration. The model consists in defining a relation between each of the fiber and matrix stress tensors by means of a fourth-order bridging tensor (A_{ijkl}) as follows:

$$\left\langle \sigma_{ij}^{(m)} \right\rangle = A_{ijkl} \left\langle \sigma_{kl}^{(f)} \right\rangle \tag{1.6}$$

The effective elastic tensor is computed based on the Mori-Tanaka approach; as defined earlier. The model's potential applications include estimating a range of mechanical properties for both unidirectional and multi-directional laminates. These include aspects such as thermo-elastic behavior, ultimate strength, inelastic response, elevated temperature strength, strength envelope, fatigue life, and S-N curve. The bridging model was extended to predict the non-linear matrix plasticity induced behavior of a short fiber reinforced composite (considering a representative volume element RVE) [49]. Four composite materials were investigated: Silion carbide (SiC) particles reinforced Aluminium (AL), short SiC fibers reinforced Al, short glass fibers (GF) reinforced Polypropylene (PP), and short GF reinforced Polyamide (PA). Factors like the matrix plasticity, the matrix stress concentration factors (stress concentration occurring at the fiber ends) and the fiber orientation on the nonlinear response are considered. The model assumes an elastic behavior for the fibers along with non-linear elasto-plastic behavior for the matrix. Good agreement was shown when comparing the theoretical stress-strain curves with experimental results gathered from the literature.

Carman and Reifsnider model The Carman and Reifsnider model was originally designed to predict the mechanical properties of discontinuous fiber reinforced composites [50]. Their work consisted in adapting a configuration of concentric circular cylinders to model the composite as a distributed representative element (the inner cylinder represents the fiber, while the outer cylinder is the matrix). A linear elastic response was attributed to the composite and the corresponding elastic properties were determined. The composite can involve diverse fiber orientations, varying fiber lengths, and a range of fiber types. The composite's stiffness tensor is determined through a global averaging process, where the approximate stresses within the representative fibers and matrix embedded within the composite are taken into account. Meddad et al.[51] developed a micro-mechanical model based on the Carman and Reifsnider approach. Their work consisted in generalizing the model to a 3D configuration. The model predicted the elastic properties of a discontinuous short carbon fiber reinforced epoxy composite, while taking into account the effect of fibers distribution, length and orientation. The elastic properties obtained analytically showed good agreement with experimental data found in the literature.

1.4.1.2 Phenomenological models

While physical models can provide highly accurate predictions of composite behavior, this accuracy comes at the cost of increased complexity and computational demands. Phenomenological models offer a trade-off between accuracy and simplicity, by selecting an appropriate level of complexity based on the application's requirements. In addition to the aforementioned reason, computational efficiency, limited data requirements, and general applicability on various materials justify the employment of phenomenological approaches to predict complex behaviors of composite materials.

Over the years, several studies have been carried on polymers as well as their corresponding composites as an attempt to identify or develop phenomenological material models capable of describing the temperature/strain rate dependent response of such materials. Some researchers relied on conventional material models that were originally designed for metals. They proposed modifications to adapt the model for polymeric behavior. Other researchers developed constitutive laws specifically designed for amorphous and semi-crystalline polymers. Those models are adjusted to fit the performance of fiber reinforced polymers, since the temperature and strain rate sensitivity is mainly a characteristic of the matrix material. This section reviews some of the common phenomenological laws applied to predict the behavior of polymers and FRPs.

Viscoelastic models

Maxwell model Viscoelastic material models can also be applied to model the behavior of polymers and their corresponding composites. The generalized Maxwell model presented in Figure 1.9 is one of the simplest viscoelastic models which is able to describe the stress relaxation of a polymer and is included in a large number of studies. In some investigations, viscoelastic models were applied to predict the thermoforming behavior of polymers or their corresponding composites ([52], [53]). In this case, it is important to note that the viscoelastic model typically focuses on the deformation of the polymeric sheet during the heating and shaping stages, including its viscoelastic response to temperature, strain, and strain rate. The removal of the formed part from the mold is generally not included in these models. Factors such as the thickness distribution of the formed part can be investigated ([52], [53]).

The study of Peng et al.[53], presents a phenomenological thermo-mechanical viscoelastic

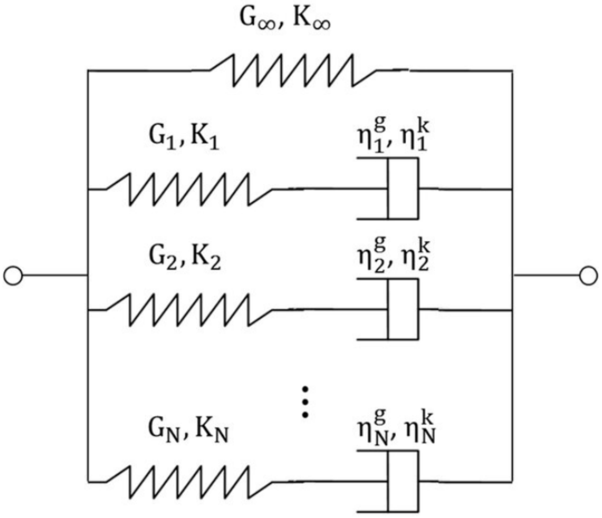

Figure 1.9: Generalized Maxwell model [54]

constitutive model for polypropylene wood composites. The specimens are compressed at quasi-static strain rates and at temperatures of 90°C, 130°C, and 170°C. Relying on the Maxwell viscoelastic approach, a nonlinear thermo-mechanical viscoelastic constitutive model is developed for the polypropylene wood composite by decoupling the effect of temperature with that of the strain rate. The parameters of the model are calibrated based on the experimental stress-strain curves of the thermo-compression tests. The model was implemented in the FE simulations. The simulated stress-strain curves were in good correlation with the experimental curves. The constitutive law equation is presented as:

$$\bar{\sigma}(\bar{\varepsilon}, \dot{\bar{\varepsilon}}, T) = E_0 \bar{\varepsilon}^n + \int_0^t E_1(T) \dot{\bar{\varepsilon}}(\tau) \exp\left(-\frac{t-\tau}{\theta_1}(T)\right) d\tau \tag{1.7}$$

$\bar{\sigma}(\bar{\varepsilon}, \dot{\bar{\varepsilon}}, T)$ represents the equivalent stress that depends on the equivalent strain $\bar{\varepsilon}$ and strain rate $\dot{\bar{\varepsilon}}$ as well as on the temperature T. θ_1 represents the stress relaxation time of the Maxwell element. The elastic parameters E_0 and n responsible for the wood fibers behavior are assumed to be independent of T and $\dot{\bar{\varepsilon}}$, whereas the equivalent Young's modulus of the polypropylene matrix E_1 depends of T. The model was then used to simulate the thermoforming of car interior part (made of polypropylene wood composite) and investigate the effect of temperature on the thickness distribution.

Chang et al.[55] investigated the uniaxial tensile responses of Poly-ether-ether-ketone (PEEK) prior to necking at strain rates ranging from 10^{-5} s^{-1} to 10^{-1} s^{-1} and temperatures ranging from -60°C to 140°C. The tensile responses exhibit nonlinear characteristics and dependence of temperature and strain rate. Based on the uniaxial tensile results, a phenomenological nonlinear viscoelastic constitutive model is proposed to characterize the stress-strain response of PEEK considering temperature and strain rate dependence. The viscoelastic model is composed of a parallel arrangement of a cubic nonlinear spring and a linear Maxwell element. The equation representing the constitutive model is as follows:

$$\bar{\sigma}(\bar{\varepsilon},\dot{\bar{\varepsilon}},T) = E_0(T)\bar{\varepsilon} + C_1(T)\bar{\varepsilon}^2 + C_2(T)\bar{\varepsilon}^3 + E_1(T)\int_0^t \dot{\bar{\varepsilon}}(\tau)\exp\left(-\frac{t-\tau}{\theta_1}(T)\right)d\tau \tag{1.8}$$

Where E_0, C_1, and C_2 denote the rate-independent elastic constants of the nonlinear spring. E_1 and θ_1 represent the elastic coefficient and the stress relaxation time of the Maxwell element, respectively (all parameters are functions of temperature). The results indicate that the proposed constitutive model can accurately predict the nonlinear tensile stress-strain responses of PEEK over a wide range of temperatures under quasi-static loading.

Reis model The study of Reis et al.[56] consisted in modelling the tensile behavior of High density polyethylene (HDPE) by a one-dimensional viscoelastic model that takes into account the strain rate and temperature sensitivity. The authors also proposed a formulation of the model that takes damage into consideration. Tensile tests were performed at strain rates ranging from 7.25 × 10^{-5} s^{-1} to 7.25 × 10^{-3} s^{-1} and temperatures of 25°C, 50°C, 75°C and 100°C. The temperature and strain rate dependent stress-strain behavior, without damage consideration, is modeled as follows:

$$\bar{\sigma}(\bar{\varepsilon},\dot{\bar{\varepsilon}},T) = [a(\dot{\bar{\varepsilon}},T)[1-exp(-b(T)\bar{\varepsilon})]] \tag{1.9}$$

Where $a(\dot{\bar{\varepsilon}},T)$ and $b(T)$ are defined as:

$$a(\dot{\bar{\varepsilon}},T) = (a_{11}T - a_{22})\dot{\bar{\varepsilon}}^{a_2} \tag{1.10}$$

$$b(T) = b_1T - b_0 \tag{1.11}$$

The same authors applied this model to predict the tensile behavior of glass fiber reinforced polyurethane under strain rate ranging from 2 × 10^{-5} s^{-1} to × 10^{-3} s^{-1} at room temperature (no temperature consideration) [57]. Compared to experimental data, the model predicted very well the modulus of elasticity and the ultimate strength at different strain rates.

Hyperelastic models

Mooney-Rivlin Moony-Rivlin is a hyperelastic model formulated by Mooney [58] and Rivlin [59], suitable for large elastic deformation. In general, hyperelastic models are characterized by a strain energy density function W that depends on different magnitudes associated to the strain field and material constants,

$$W = \left\{ \begin{array}{c} W\left(I_1, I_2, I_3\right) \\ W\left(\lambda_1, \lambda_2, \lambda_3\right) \end{array} \right\} \tag{1.12}$$

where I_1,I_2,I_3 are the invariants of Cauchy-Green strain deformation tensors and λ_1, λ_2, λ_3 are principle stretches. The stress-strain relations are then derived by differentiating the strain energy density function with respect to the invariants or the principle stretches. The Moony-Rivlin model is known for its accuracy in predicting the response of hyperelastic materials. The equation of strain energy function W defined by Mooney is:

$$W(I_1, I_2, J) = \sum_{i+j=1}^{N} C_{ij} \left(I_1 - 3\right)^{\mathrm{i}} \left(I_2 - 3\right)^{j} + D(J-1)^2 \tag{1.13}$$

Where

$$I_1 = \left(\lambda_1\right)^2 + \left(\lambda_2\right)^2 + \left(\lambda_3\right)^2 \tag{1.14}$$

$$I_2 = \left(\lambda_1 \lambda_2\right) 62 + \left(\lambda_2 \lambda_3\right)^2 + \left(\lambda_3 \lambda_1\right)^2 \tag{1.15}$$

$$J = \lambda_1 \lambda_2 \lambda_3 \tag{1.16}$$

C_{ij} represents Rivlin's coefficients and D refers to the incompressibility of the material (For incompressible materials the term $D(J-1)^2$ is eliminated).

Pham et al. [60] predicted the strain rate and temperature dependent stretching behavior of a thermoplastic polymer (polyethylene therephtalate PET) using a visco-hyperelastic model. The Mooney-Rivlin scheme was included in the modeling process to represent the elastic part of the behavior whose parameters were determined by means of a non-linear curve fitting based on data obtained from a biaxial characterization technique. Afterwards, the model was applied to simulate the stretch blow molding of PET which was successfully validated experimentally.

In another study, Pham et al. [61] investigated the stretching behavior (large deformation) of a glass mat thermoplastic (polypropylene PP). They performed in-plane biaxial stretching tests for three different temperatures (160, 170 and 180 °C) at 0.5s^{-1} while considering three stretch ratios. The authors proposed a transversely isotropic hyperelastic model and calibrated the parameters based on the experimental results of stress as a function of stretch ratio. The model was later on applied to predict (FE simulation) the thickness of a thermoformed part made of glass mat polypropylene.

Viscoplastic models

Cowper-Symonds model Cowper-Symonds [62] is a typical strain rate-dependent model, originally designed for metals, that scales the hardening law by a strain factor and a strain rate factor. The equation of the model is:

$$\bar{\sigma}(\bar{\varepsilon}_p, \dot{\bar{\varepsilon}}) = [\sigma_0(\bar{\varepsilon}_p)][1 + (\frac{\dot{\bar{\varepsilon}}}{C})^{\frac{1}{P}}] \tag{1.17}$$

Where $\sigma_0(\bar{\varepsilon}_p)$ represents the hardening law (Ludwik, Voce, Swift...) at the predefined reference strain rate which depends on the equivalent plastic strain $\bar{\varepsilon}_p$. C and P are the material parameters representing the effect of strain rate.

Although this model was designed for metals, it was remarkably applied to predict the behavior of fiber reinforced composite materials. Wang et al.[63] studied the mechanical properties and fracture behaviors of polypropylene and short basalt fiber reinforced polypropylene composites at varying strain rates (0.001 up to 10 s^{-1}). The authors defined the initial hardening law by relying on Ludwik [64] and Voce models [65]. Compared to the experimental stress-strain results, the established model gave good prediction of the strain rate dependent behavior at the studied strain rate range.

Likewise, Duan et al. [24] investigated the influence of strain rate (ranging from 0.001 s^{-1} to 50 s^{-1}) on mechanical properties of long glass fiber reinforced polypropylene composite (LGFRP) by both experimental tests and numerical simulations for its application on automobile structural components. The study found that the mechanical properties of LGFRP composite were significantly affected by strain rates. Cowper-Symonds model was calibrated based on experimental tensile tests. The FE simulation results of the strain countours agreed well with the experimental results obtained by Digital Image Correlation.

Gates and Sun model Gates and Sun [66] presented a constitutive model to describe the elasto-viscoplastic behavior of fiber-reinforced thermoplastic composites (unidirectional continuous AS4 graphite fibers reinforced polyether ether ketone (PEEK)) under plane stress conditions. This modeling approach is suitable to predict the behavior of materials under different loading conditions, especially when materials exhibit behaviors such as creep (time-dependent deformation under a constant load), stress relaxation (decrease in stress over time under constant deformation), and other time-dependent phenomena. Anisotropy considerations (orthotropic plasticity) proposed by Sun and Chen [67] were included in the model. Considering uniaxial loading where the applied load isn't aligned with the fiber direction (off-axis), an orthotropic elastic/viscoplastic fiber-reinforced composite to predict the uniaxial flow rate is given in the equation below:

$$\dot{\varepsilon_x} = [\frac{\dot{\sigma}}{E}][h(\theta)]^{1+(1/m)} \left(\frac{1}{K}\right)^{1/m} (\sigma_x - \sigma_x^*)^{1/m} \tag{1.18}$$

Details of the parameters $h(\theta)$, K, σ_x^* and m can be found in [67].

DSGZ The DSGZ (named after the authors: Duan, Saigal, Greif, Zimmerman) stands as a viscoplastic phenomenological model created specifically for glassy or semi-crystalline polymers [68]. In addition to temperature and strain rate consideration, this incorporates softening and hardening effects. The constitutive law describing the stress σ is given by:

$$\bar{\sigma}(\bar{\varepsilon}, \dot{\bar{\varepsilon}}, T) = \left\{ f(\bar{\varepsilon}) + \left[\frac{\bar{\varepsilon} \cdot e^{\left(1 - \frac{\bar{\varepsilon}}{C_3 \cdot h(\dot{\bar{\varepsilon}}, T)}\right)}}{C_3 \cdot h(\dot{\bar{\varepsilon}}, T)} - f(\bar{\varepsilon}) \right] \cdot e^{\big(\ln\big(g(\dot{\bar{\varepsilon}}, T) - C_4\big) \cdot \bar{\varepsilon}} \right\} \cdot h(\dot{\bar{\varepsilon}}, T) \tag{1.19}$$

Where

$$f(\bar{\varepsilon}) = \left(e^{-C_1 \cdot \bar{\varepsilon}} + \bar{\varepsilon}^{C_2}\right)\left(1 - e^{-\alpha \cdot \bar{\varepsilon}}\right) \tag{1.20}$$

$$h(\dot{\bar{\varepsilon}}, T) = (\dot{\bar{\varepsilon}})^m e^{\frac{a}{T}} \tag{1.21}$$

and $g(\dot{\bar{\varepsilon}}, T)$ is the dimensionless form of $h(\dot{\bar{\varepsilon}}, T)$.

Achour et al.[69] extended the phenomenological viscoplastic DSGZ model developed for glassy or semi-crystalline polymers to an implicit formulation. The behavior of polypropylene was investigated at strain rate ranging from 0.92 to 258 s^{-1} and temperature ranging from 20°C to 60°C. The material parameters were calibrated based on the tensile stress-strain curves. The model was then validated with additional experimental results at different strain rates and temperatures.

Deng et al.[70] proposed a hybrid lamination model that relied on the DSGZ approach to simulate the solid state thermo-stamping of a woven fabric reinforced thermoplastic polymer (carbon fiber reinforced PEEK). The deformation behavior of the thermoplastic, which exhibits visco-elasto-plastic characteristics, is described by the DSGZ phenomenological model. Meanwhile, the anisotropic mechanical properties of the textile reinforcement under significant deformation are defined by a separate anisotropic model following a hypo-elastic law. The process of parameter identification for the hybrid lamination model is conducted independently for each of these components. The simulated outcomes, including the distribution and profile of shear angles, align closely with the experimental findings obtained from the uniaxial bias extension tests. Experimental and simulation results underscore that temperature plays a remarkable role in influencing the forming process.

G'Sell and Jonas A widespread viscoplastic model, G'Sell and Jonas, was initially designed for modeling the mechanical behavior of semi-crystalline polymers [71]. The main advantage of this model is its ability to integrate the effects of viscoelasticity and viscoplasticity in a single formulation as stated below (equation 2.1).

$$\bar{\sigma}(\bar{\varepsilon},\dot{\bar{\varepsilon}}) = K \cdot \exp\left(h\bar{\varepsilon}^2\right)(1-\exp(-W\bar{\varepsilon}))\cdot\dot{\bar{\varepsilon}}^m \tag{1.22}$$

m (strain rate sensitivity), K (scaling factor), h, and W are material parameters. Low strain levels are described by the term $(1-\exp(-W\bar{\varepsilon}))$. The term $\exp\left(h\bar{\varepsilon}^2\right)$ describes the plastic strain hardening which takes place at high strain levels as in the case of glassy unreinforced polymers [22]. In the work of Schossig et al. [72], the influence of strain rate and fibers concentration on the mechanical behavior of glass fiber reinforced thermoplastic (polypropylene) was experimentally investigated. G'Sell and Jonas model was used to describe the strain rate dependent behavior of the materials. Additionally, this model was used to represent the deformation behavior during thermoforming applications. Atmani et al. [22] have also modeled the thermoforming of a yogurt container by the elasto-viscoplastic G'Sell and Jonas model with thermal considerations. Trufasu et al.[73] conducted a study on the mechanical behavior of polyether-ether-ketone (PEEK) composites. The parameters of the mechanical behavior law were identified using experimental data of the compression tests. The study shows that the mechanical behavior law can accurately describe the mechanical behavior of PEEK composites.

1.4.1.3 Modeling of anisotropy

This section briefly discusses possible approaches for modeling anisotropy in fiber reinforced thermoplastic polymers. In some cases, anisotropy can be described within an elastic framework, which requires determining elastic constants in various directions. The planar orthotropic elasticity [74] is an example of such approaches. Holmstrom et al.[75] investigated the elastic anisotropic tensile behavior of discontinuous glass fiber polyamide-6 for different fiber weight fractions. The values of Young's modulus, in-plane and out-of-plane Poisson's ratio, ultimate tensile strength and fracture strain predicted with the orthotropic elasticity agreed well with the experimental values. A similar study [76] was conducted on discontinuous glass fiber reinforced polypropylene. The orthotropic elasticity was combined with a progressive damage model to predict the anisotropic elastic behaviour of the reinforced thermoplastic. Anisotropy is often disregarded in some studies where the thermoforming (prior to the removal of the part from the mold) behavior of thermoplastics (e.g.acrylonitrile butadiene styrene [52]) or fiber reinforced thermoplastics (e.g. wood fiber reinforced polypropylene [53]) is represented with viscoelastic models. In other cases, where the material undergoes large permanent plastic deformation, anisotropy can be modeled during plastic flow and therefore, described by plasticity criteria. Several attempts to examine the strength and yield characteristics, relying on homogenized material properties, introduced yield criteria such as: the Tsai–Hill [77], Azzi–Tsai [78], Tsai–Wu [79], Hofmann [80], and Hill48[81]. Tsai-Hill criterion (apply Hill's anisotropic plasticity to the failure of homogenous, anisotropic materials) for instance, was applied by Mortazavian et al.[82] to investigate the effect of anisotropy and fiber orientation of the tensile strength and elastic modulus of discontinuous glass fiber reinforced thermoplastics (polybutylene terephthalate and polyamide-6). On the other hand, Hill48 criterion, which was initially developed to describe the yielding and plastic flow of anisotropic metallic material, found application in the field of fiber reinforced polymers. This criterion is widely recognized in calculation codes for its applicability, simplicity, frequency of use and reduced number of parameters. Choi et al.[83] associated the Hill48 yield criterion with the flow stress (Ramberg–Osgood) to evaluate the anisotropic behavior induced by the fibers orientation of two discontinuous carbon fiber reinforced thermoplastics (polypropylene and polyamide-6). In the study of Erice et al.[84], the authors predicted the compressive strain rate dependent plasticity of unidirectional carbon fiber reinforced epoxy with three different approaches. Hill48 criterion succeeded to give good simulation results when compared to the experimental stress-strain curves.

To conclude, this section briefly reviewed some of the approaches applied to model the material behavior of fiber reinforced polymers and even possible anisotropy. The following section discusses the mechanical characterization techniques generally applied to calibrate the material parameters of the mentioned models.

1.4.2 Mechanical characterization

Mechanical characterization tests play a crucial role in understanding the behavior of any material in general. Conventional tests, such as uniaxial tensile, shear and flexural tests, provide essential data on the material's basic mechanical properties. On the other hand, non-conventional tests like Nakazima, combined axial/torsion on tubular specimens, and in-plane biaxial tests offer insights into more complex mechanical responses, which is particularly important for applications involving varied loading and process conditions. Conventional tests are typically homogeneous and standardized tests regulated by norms that allow for the direct calculation of stresses and deformations. Non-conventional tests, on the other hand, involve heterogeneous tests with complex deformation fields, requiring supplementary tools and experimental devices to measure these fields. The combination of these conventional and non-conventional tests can provide a comprehensive understanding of the mechanical properties of reinforced polymers, aiding in their design and optimization for specific engineering applications.

1.4.2.1 Conventional tests

In this section, a concise overview of the standard testing methods that are frequently employed to examine the mechanical properties of polymers and reinforced polymeric materials across varying temperatures and strain rates. These tests involve the uniaxial tensile test, simple shear test and three-point/four-point bending tests.

1.4.2.1.1 Uniaxial tensile test Uniaxial tensile tests (ASTM D3039) are widely used mechanical characterization techniques to assess the tensile behavior of various materials, including metals, polymers, composites. It involves applying an axial force along the longitudinal axis of a specimen to measure its response (Figure 1.10a).

These tests can provide valuable information such as elastic constants and anisotropic coefficients. For the case of discontinuous fiber reinforced polymers, the behavior is influenced by factors such as fiber orientation, fiber length, fiber content, and the distribu-

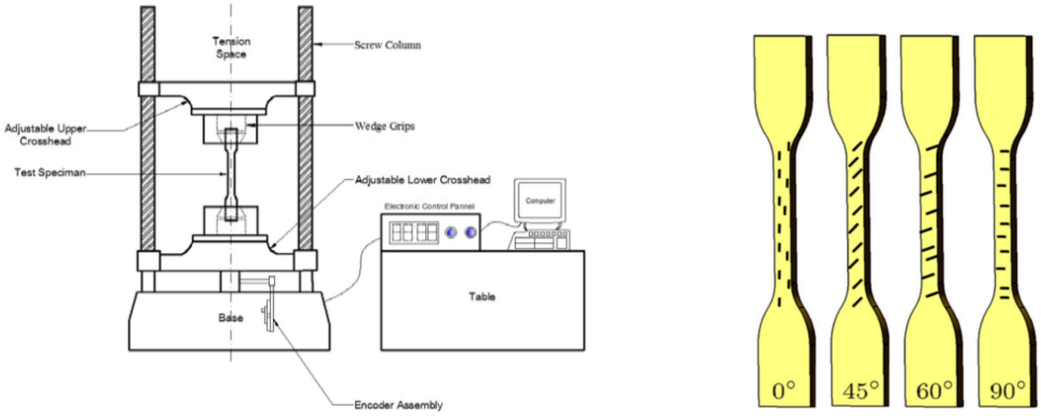

(a) Schematic of machine [85] (b) Specimens for different fiber orientations[86]

Figure 1.10: Unixial tensile test setup

tion of fibers within the matrix. The mechanical properties of these materials are often anisotropic, meaning they vary with the direction of the applied load due to the random orientation of fibers. For this reason, for an accurate characterization of the behavior, several tests should be conducted using specimens milled out from the plate material in different angles relative to the flow direction, as shown in Figure 1.10b. From these characterization techniques, one can derive experimental true stress-true strain curves for different conditions (strain rates, temperature, ...). This testing technique was applied to investigate the stress-strain response of discontinuous glass fiber reinforced polybutylene terephthalate and glass fiber reinforced polypropylene in [86] and [24], respectively.

1.4.2.1.2 Shear test Over the years, shear testing of fiber reinforced materials has been conducted using methods ranging from very simple to complex techniques. The testing methods are generally grouped according to the geometry of the specimen.

V-notched rail or Iosipescu test A common in-plane shear test applied on flat specimens is known as V-notched rail or Iosipescu shear method (ASTM D7078). This testing technique involves assessing the shear properties of isotropic as well as anisotropic material such as fiber reinforced polymers ([87]). It is achieved by clamping the ends of a V-notched specimen between two sets of loading rails. When subjected to tension, these rails introduce shear forces into the specimen via its faces. The schematic diagram of the test setup is illustrated in Figure 1.11 The study of Selezneva et al. [88] considered this technique to determine the shear modulus and strength of discontinuous carbon fiber reinforced polyether–ether–ketone. The shear properties of unidirectional (two directions were considered: 0° and 90°) carbon fiber reinforced polyether–ether–ketone and epoxy and glass fiber reinforced polyester were also investigated using the Iosipescu technique.

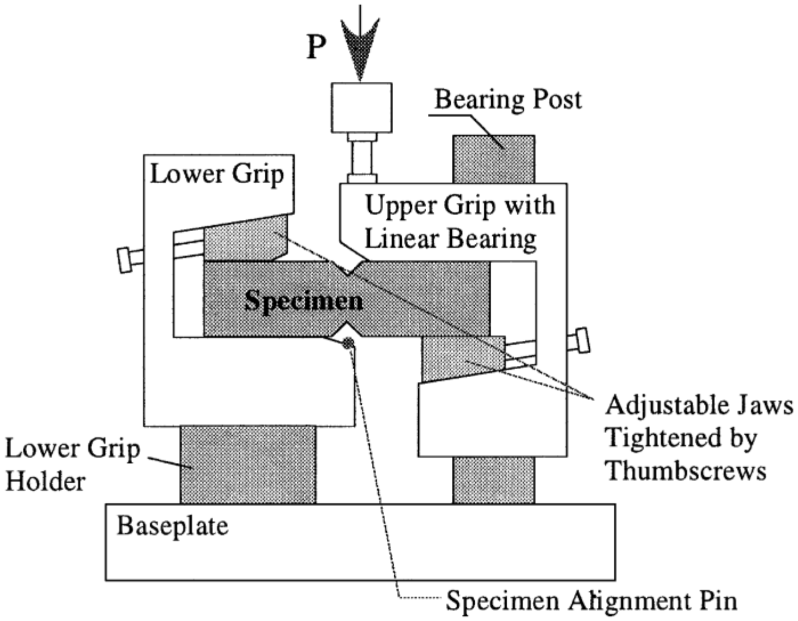

Figure 1.11: Schematic of V-Notched rail shear test [89]

Thin-walled tubes The shear (torsional) testing of a thin-walled tube is a common and universal approach to obtain shear modulus and shear strength of a material. It is known to induce a relatively pure and consistent shear stress state. This is due to geometry of the tests specimen, where the magnitude of shear strain linearly changes from the center axis of rotation, the variation across the thin tube wall remains minimal. For composite materials, unidirectional fiber reinforced composites are the preferred specimens (easier to manufacture) [90]. Figure 1.12 illustrates an experimental setup of the thin-walled tube testing technique along with the geometry of the specimen. In the study of Weber et al.[91], the authors measured the shear properties of unidirectional-orientated flax and glass fiber reinforced polymer (epoxy). Tarnopol'skii et al.[90] also investigated the shear properties of glass fiber/epoxy composites with (±45)lay-up, using different shear testing techniques. Amongst all, the thin-walled tube test induced the highest value of shear strength. This technique is generally preferable for thermoset composites since the common manufacturing technique for the thin-walled tubes is filament winding which is usually recommended for thermosets.

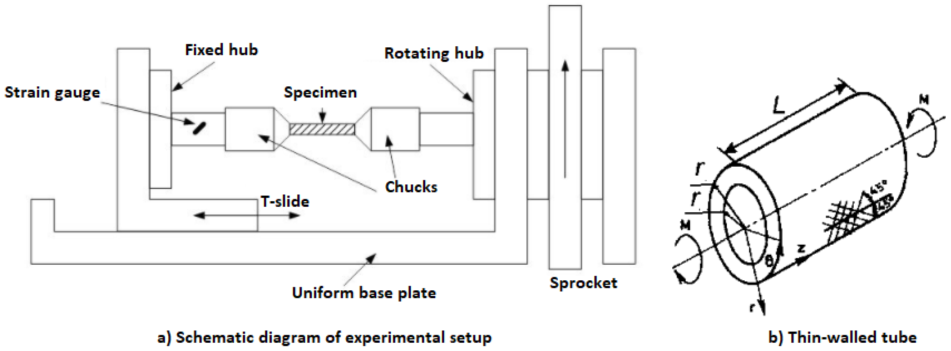

Figure 1.12: Schematic of Thin-walled tube shear test ([92] [90])

bias-extension test This bias-extension test is typically applied to measure the shear properties of woven-fabric composites [93]. This method considers a specimen characterized by a rectangular gauge section and fibers oriented at 45° and -45° angles relative to the loading direction, as illustrated in Figure 1.13 showing the undeformed and deformed specimen [94]. The tested specimen is cut or prepared in a way that the extension force will be applied at an angle other than the principal axis. A conventional uniaxial tensile machine can be adapted to perform this test [93]. Brands et al.[94] used the bias-extension technique to characterize the shear properties of two unidirectional (woven) fiber reinforced thermoplastics (carbon/low-melt polyaryletherketone and carbon/polyetherketoneketone). In the study of Wang et al.[93], the authors investigated the shear behavior of two woven thermoplastis composites: carbon/polyphenylene sulphide and carbon/polyetheretherketone. Based on the load-displacement data obtained from the bias-extension tests, the shear moment versus in-plane shear angle curves were derived for both tested materials.

1.4.2.1.3 Flexural test on beams Both three-point and four-point bending (Figure 1.14) tests are used to determine the flexural properties of materials. Different shapes of specimens can be adopted such as beams, plates, rods and other structural elements subjected to bending loads. Nakashima et al.[95] determined the flexural modulus of discontinuous carbon fiber reinforced polyamide-6, using both three-point and four-point bending tests, while varying the specimen thickness and support span. They concluded that for the elastic modulus, there were very small differences between test data of both

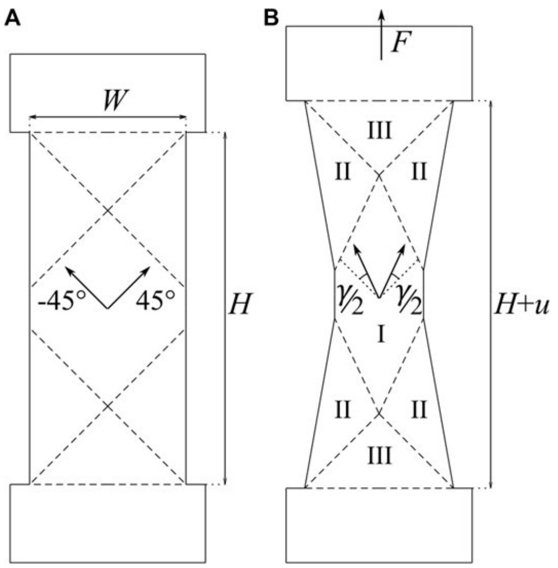

Figure 1.13: Schematic of bias-extension test [94]

tests. Yu and Ma[26] investigated the temperature and loading rate dependent flexural properties (modulus and strength) of discontinuous glass fiber reinforced polypropylene by conducting three-point bending tests on beam specimens.

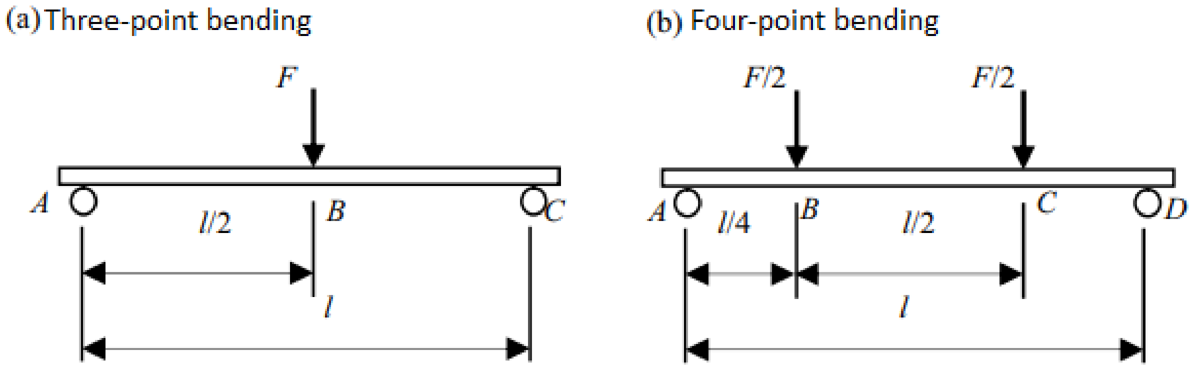

Figure 1.14: Schematic of three-point and four-point bending principles [96]

1.4.2.2 Non-conventional tests

Non-conventional tests, such as Nakazima, combined loading tests, and in-plane biaxial test on cruciform specimens, offer distinct advantages over conventional tests in certain situations and for specific material characterization objectives.

1.4.2.2.1 Nakazima Test The Nakazima test (Figure 1.15) is a specialized biaxial test that applies proportional loading along two orthogonal axes while maintaining a constant biaxial stress ratio. The specimen is subjected to simultaneous tensile and compressive loads in different directions, allowing for the study of complex stress states. This testing technique is very close to deep-drawing processes and is usually applied to construct forming limit diagram for metallic materials. In the study of Rohrig et al.[86], the Nakazima test was applied to investigate the mechanical properties of glass fiber reinforced polybuthylene thereftalte (PBT). During the experiment, digital image correlation was applied to evaluate the strain information over the whole surface. The force was measured by a load sensor.

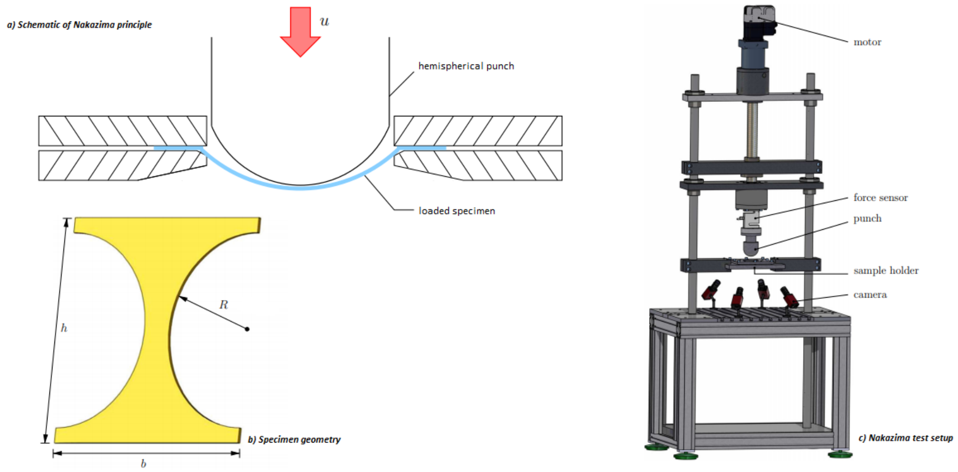

Figure 1.15: Nakazima test schematic diagram [86]

1.4.2.2.2 Combined axial loading with simple torsion on tubular specimen This method has been used to investigate the biaxial behavior of metals in 1940's and then composites in 1960's. This technique subjects the material to both axial (tensile or compressive) and torsional (shearing) loads simultaneously. When the specimen is subjected to axial and torsional loads at a 45° angle to the cylinder axis, it results in two perpendicular normal stresses along the principal directions. Figure 1.16 shows a schematic diagram of the test apparatus.

In the study of Andriss et al.[97] the authors subjected tubular specimens to combined axial and torsional loading. This approach was employed to characterize the non-linear mechanical behavior of a continuous carbon fiber-reinforced polycarbonate material with unidirectional plies under quasi-static, multiaxial loading conditions.

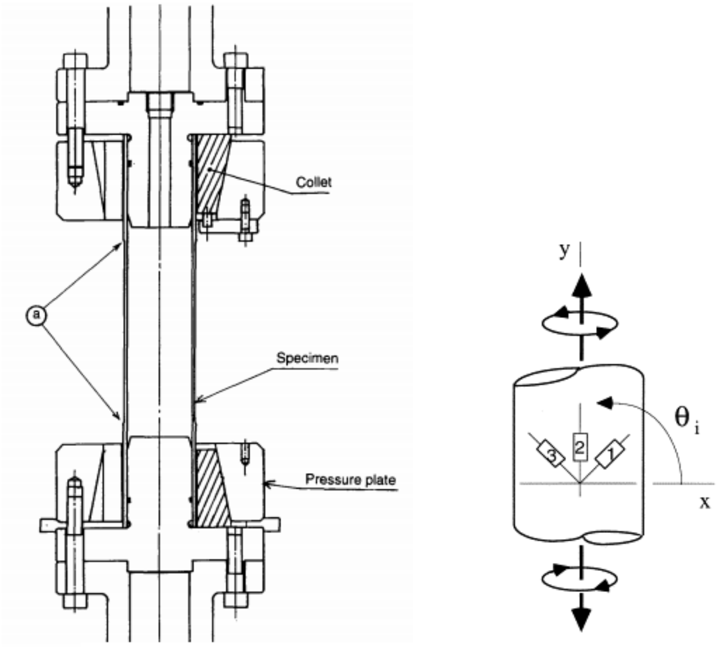

a) Schematic of clamping fixture for the combined axial/torsion test

b) Tubular specimen

Figure 1.16: a) Apparatus of combined axial/torsion on tubular specimen [98]; b) geometry of specimen [99]

1.4.2.2.3 In-plane biaxial loading

Biaxial stretching of rectangular sheets A Biaxial Stretching mechanism [100] is commonly used for the mechanical characterization of materials, particularly polymers, films, and sheets. It is capable of producing biaxially oriented polymer sheets and has enabled a fundamental study to be made of the parameters that influence the properties of biaxially oriented polymer products. The principle of biaxial stretching of rectangular sheets is illustrated in Figure 1.17

Brückner KARO IV is a biaxial stretching machine (Figure 1.18) developed in a German laboratory. This machine was primarily used to characterize the biaxial behavior of polymeric material. Pham et al.[60] characterized the temperature and strain rate dependent behavior of polyethylene terephthalate PET using the Bruckner biaxial stretcher. The same characterization technique was applied by Ouchiar et al.[102] to investigate the stretching behavior of Polylactide (PLA) and PLA-Talc nanocomposites. The biaxial stretching was carried at two different drawing temperatures.

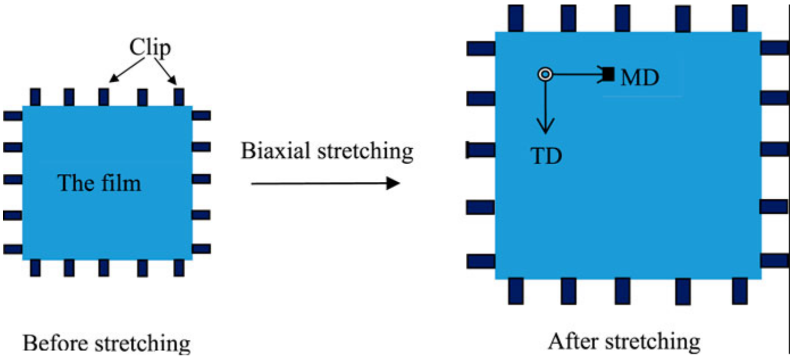

Figure 1.17: Principle of in-plane biaxial stretching of rectangular sheets [101]

Figure 1.18: Bruckner biaxial stretching machine [60]

Flat Cruciform specimens The biaxial test using cruciform specimens is a specific type of in-plane biaxial testing method used to evaluate the mechanical behavior of materials under biaxial stress states. This test involves the use of cruciform shaped specimens comprising two perpendicular arms, and it is typically performed with a servo-hydraulic testing machine capable of applying loads along two perpendicular directions.
In the following, section A will be dedicated to briefly state the testing machines used for this type of testing. Section B gives a concise overview on the types of cruciform specimens found in the literature.

A. In-plane biaxial testing machines

One option to apply tensile forces along the two perpendicular arms of the cruciform specimen, consists in developing and adding link mechanism attachments to conventional uniaxial testing machines, as proposed by Ferron and Makinde [103] (Figure 1.19). The authors applied this testing technique to characterize the biaxial behavior of Aluminum-

1050. This approach is cost-effective but it does not allow for the adjustment of load

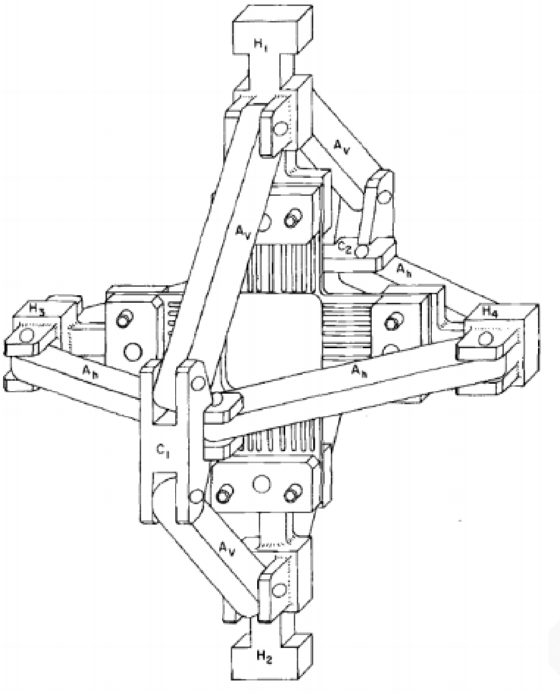

Figure 1.19: Link mechanism attached to a conventional uniaxial tensile test machine [103]

ratios during tests. Additionally, this type of machine is not suitable for dynamic testing. Consequently, stand-alone machines appear to be better suited for such tests. These testing devices are equipped with four independent actuators along both directions, enabling the realization of various linear and nonlinear load paths. Typically, these machines are equipped with a closed-loop control system to maintain load balance among the four arms and to make necessary adjustments to keep the specimen centered during the test. Boehler et al. [104] designed an in-plane biaxial testing apparatus (Figure 1.20a) to perform experimental investigations on anisotropic materials, such as composite plates or rolled sheet metals. Likewise, Makinde et al.[105] designed a biaxial testing machine (Figure 1.20b) suitable for the investigation of the behavior of sheet metals and composite materials subjected to monotonic and cyclic biaxial loads. Chen et al. [106] recently developed an in-plane biaxial apparatus (Figure 1.20c) designed for the characterization of heat-resistant composites and sheet metal subjected to high temperatures (up to 2500 $°C$) and complex loads (tension–tension, tension–compression, and compression–compression). The authors characterized the behavior of a carbon matrix reinforced with continuous carbon fibers.

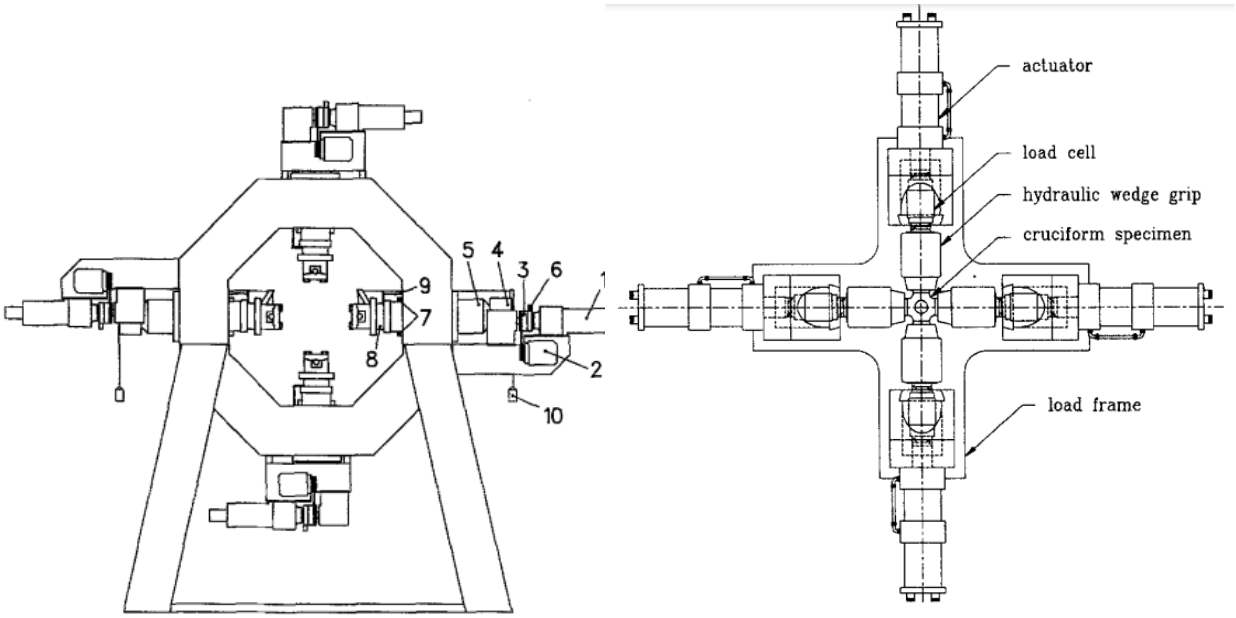

(a) Boehler et al.[104]

(b) Makinde et al.[105]

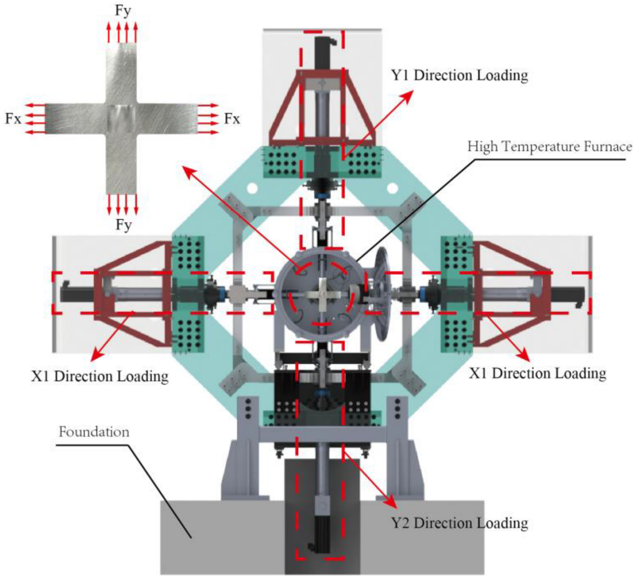

(c) Chen et al.[106]

Figure 1.20: Stand-alone in-plane biaxial testing machines

B. Types of cruciform specimens

As previously mentioned, the machine is designed for conducting tests on flat cruciform specimens made of both isotropic or anisotropic materials. The main challenge for this kind of in-plane biaxial testing is to develop a specimen design that effectively facilitates biaxial

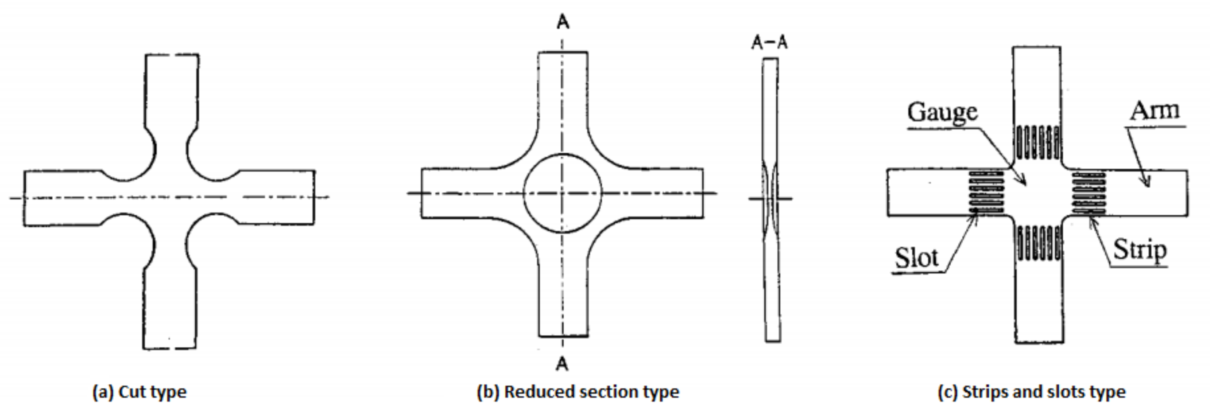

(a) Cut type (b) Reduced section type (c) Strips and slots type

Figure 1.21: Cruciform specimen geometries proposed by Ohtake et al. [108]

tests under conditions of significant deformation, considering factors related to initial anisotropy (e.g., composite materials, rolled metals) as well as anisotropy induced by deformation. Depending on the requirements and objectives of the test (i.e. Identification of hardening law, forming limits, fatigue strength, yield surface...), the standard shape of the cruciform specimen can be modified and adjusted. Generally, the requirements for an ideal in-plane biaxial tensile tests using flat cruciform specimens are: i) homogeneous stress-strain distribution in the gauge central region; ii) the highest stress level should be attained in the gauge section where initial yielding occurs; iii) No stress concentration outside this area [104], [107]. Traditionally, to meet these requirements, the designed specimen typically incorporates one or a combination of the following configurations: a) Implementing curved fillets between the arms, b) Introducing thickness reduction in the central zone, c) Adding slits [108], as shown in Figure 1.21.

The International Organization for Standardization (ISO) proposed a cruciform shape with seven slits in each arm (ISO 16842 [109]) shown in Figure 1.22. According to ISO, this shape is easy to manufacture, no thickness variation is required, and the yield point can be achieved with no need for additional numerical simulations. The drawback is that the maximum deformation at the central zone is not satisfying [110].

Zidane et al.[111] proposed a cruciform specimen configuration (Figure 1.23), featuring slits in the arms and a two-step reduction in thickness within the circular central region. This geometry was optimized through numerical simulation and verified through in-plane biaxial tensile testing on aluminum AA5086. The results led to the conclusion that employing the designed cruciform specimen in a single biaxial tensile test is adequate for characterizing both the material's forming limit diagram and its rheological properties.

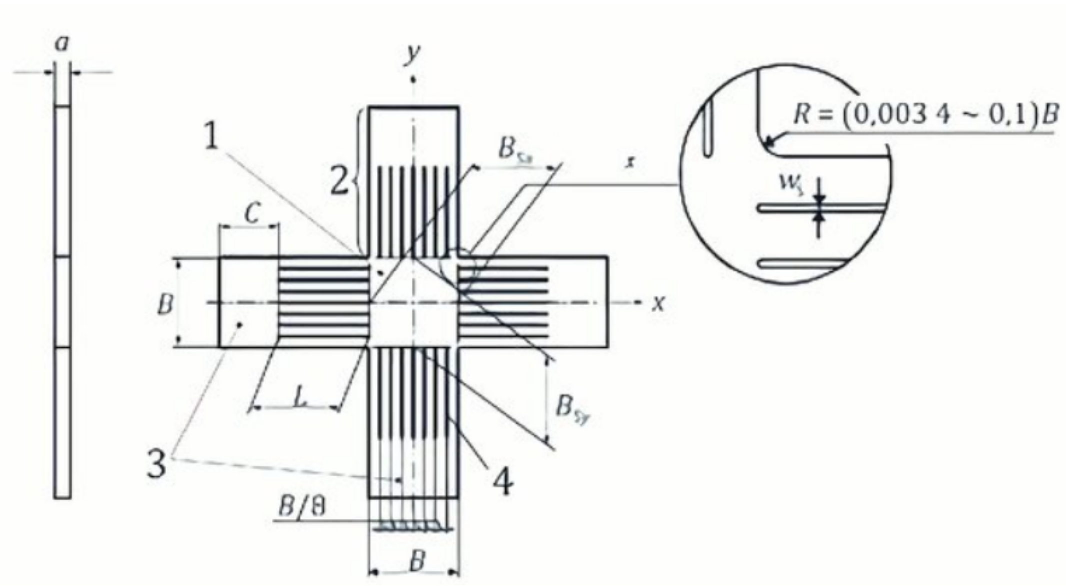

Figure 1.22: In-plane biaxial cruciform specimen standardized by ISO 16842 [109]

Song et al. [112] conducted additional research into the forming limit curve at fracture

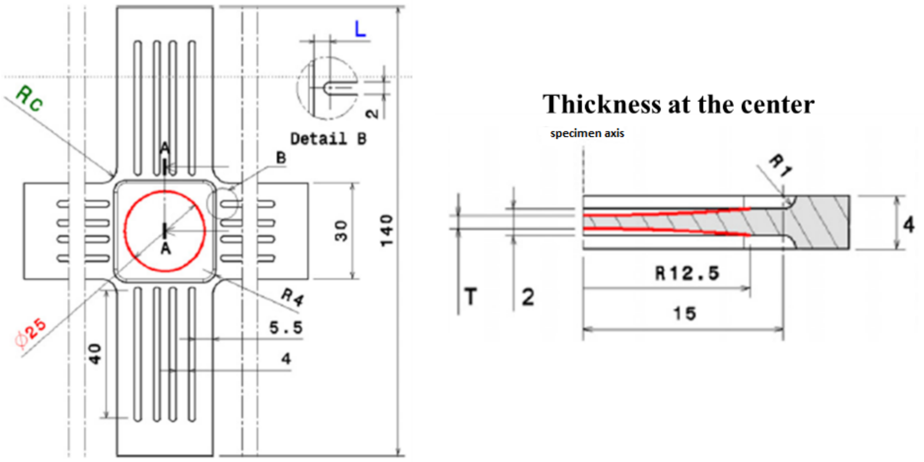

Figure 1.23: Cruciform specimen proposed by Zidane et al. [111]

(FLCF) for steel DP600. The optimized geometry of the cruciform specimen is presented in Figure 1.24. Based on the experimental FLCF data obtained, the fracture yield criteria was identified through numerical simulation. This criteria was then employed to predict the FLCF for various strain paths.

The aim of a study conducted by Xiao et al.[113] was to predict the forming limits of TA1 titanium at both room and elevated temperatures. They proposed a design for cruciform

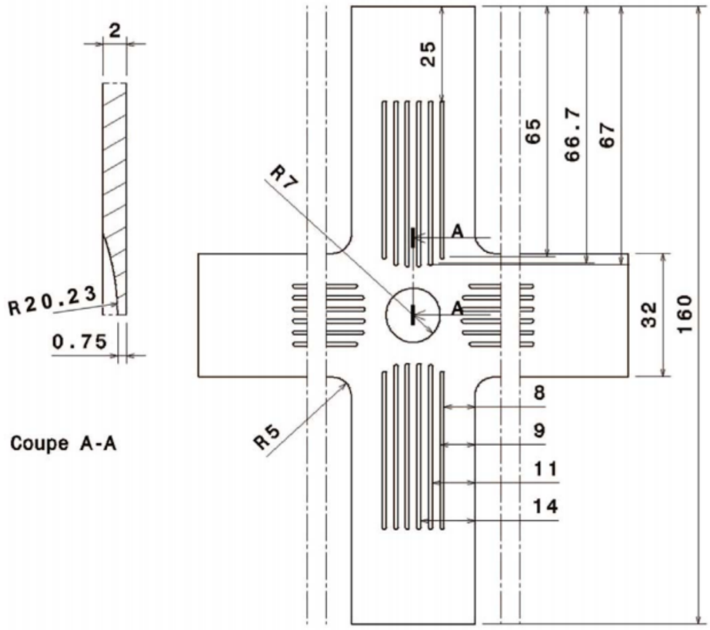

Figure 1.24: Cruciform specimen proposed by Song et al.[112]

specimen dedicated for the in-plane biaxial tensile tests (Figure 1.25). Results proved that the proposed semi-spherical thickness reduction induced localized necking and fracture in the central zone.

Nasdala et al.[110] proposed a cruciform specimen to determine the yield surface of aluminium 5754 alloy. The geometry is presented in Figure 1.26. In their configuration, the authors modified the standard specimen proposed by ISO 16842 (Figure 1.22) by including wider slits in the arms to avoid stress concentration as well as further thinning of the gauge area.

Deng et al.[114] designed a cruciform specimen geometry for constitutive model identification, considering 1018 steel and 2090-T3 aluminum. The proposed specimen comprises a gauge section with reduced dimensions, arms featuring slots, and extremely sharp geometric features in between, as shown in Figure 1.27. This designed specimen induced large strains in the gauge section before failure. Liu et al.[115], [116] conducted a study to investigate the hardening behavior of metallic sheets under conditions involving significant strains. They proposed an optimized specimen design for this purpose, which is presented in Figure 1.28. This specimen features a central area with reduced thickness, slots in each arm, and a notch positioned between two arms. Using this particular specimen shape ensured large equivalent plastic strains, up to 30%, within the central zone when subjected

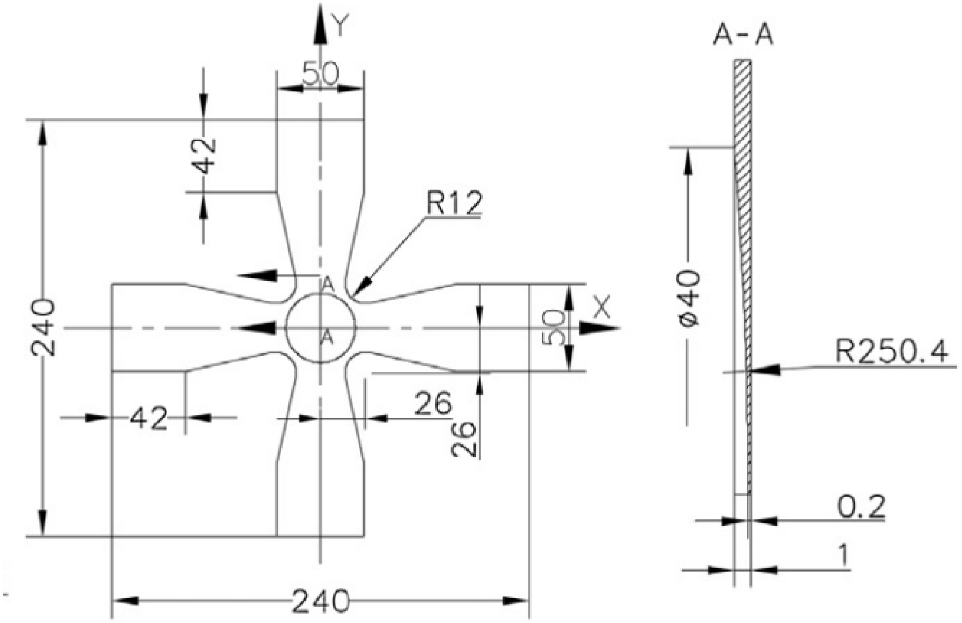

Figure 1.25: Cruciform specimen proposed by Xiao et al. [113]

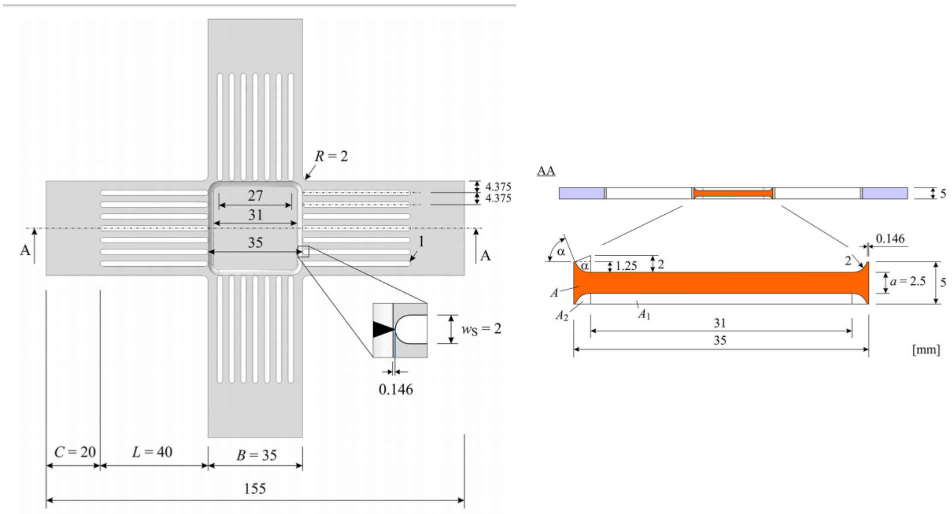

Figure 1.26: cruciform specimen proposed by Nasdala et al.[110]

to equi-biaxial tensile loads under both quasi-static and dynamic conditions.

Welsh and Adams [117] proposed a cruciform specimen to determine the biaxial strength of any given stress ratio for a carbon/epoxy laminated composite. The optimization involved varying: the size of the milled central area; the shape of central zone (circular or square); the size of the fillet radius between the loaded arms. Based on the obtained stress results,

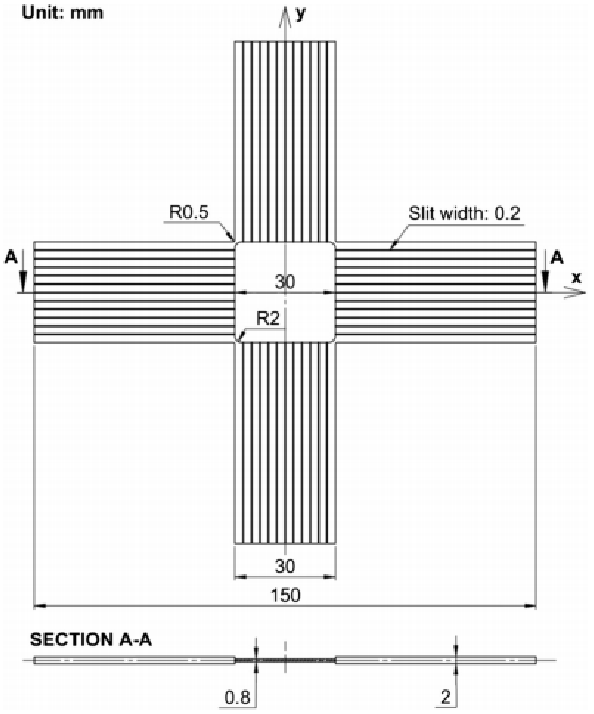

Figure 1.27: Cruciform specimen proposed by Deng et al. [114]

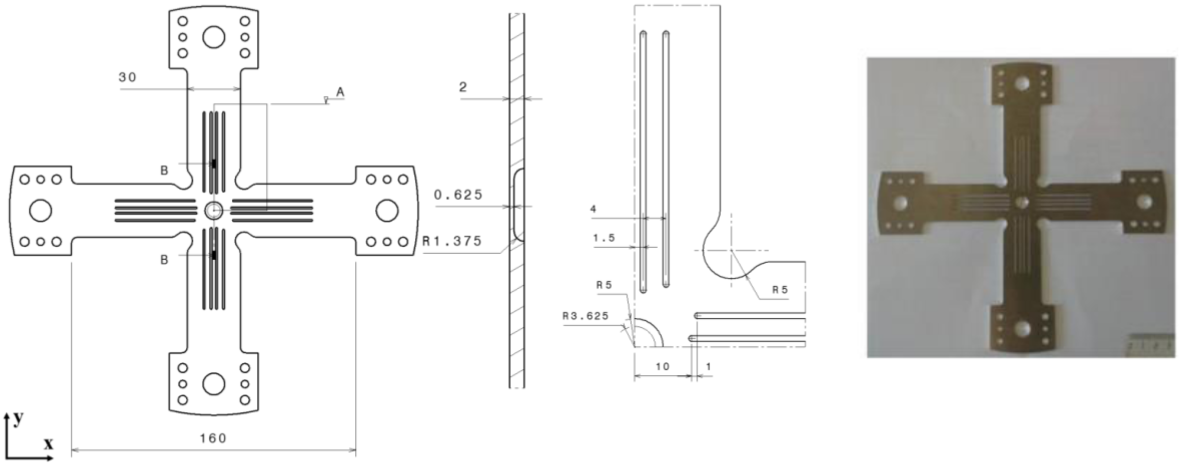

Figure 1.28: Optimized cruciform geometry proposed by Liu et al.([115], [116])

the authors selected the specimen geometry that featured a large corner fillet and a small squared gauge area (Figure 1.29).

It’s important to note that there exists geometries that can be applied for both metallic and composite materials. Makinde et al.[105] introduced two distinct cruciform specimen

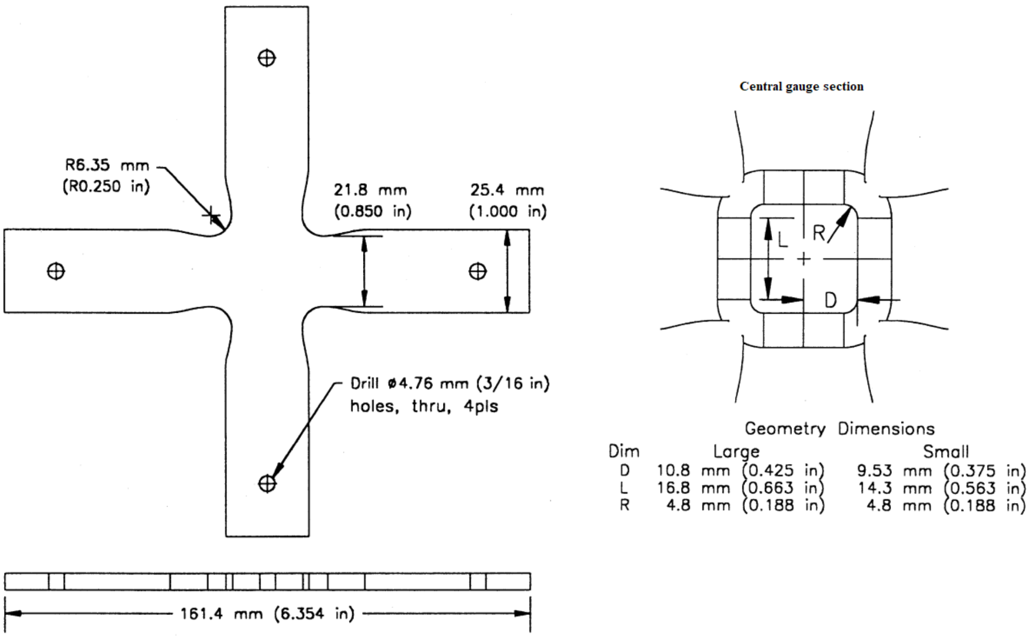

Figure 1.29: Cruciform specimen proposed by Welsh and Adams [117]

geometries for the examination of the mechanical properties of sheet metals and composite materials under both monotonic and cyclic biaxial loading conditions, as depicted in Figure 1.30. One design featured a central zone with reduced thickness in a circular shape, while the other had a central zone with reduced thickness in a rectangular shape and included slits in each arm. The authors stated that in experiments where small strains are involved, like those studying fatigue crack initiation and propagation (or testing composite materials), cruciform specimens with a smaller circular central section are recommended. An illustrative example of this geometry is displayed in Figure 1.30a. In contrast, larger strains are attained with cruciform specimens with a rectangular central section and slots in the arms, as shown in Figure 1.30b. These slots are designed to reduce the rigidity of the arms. Without this modification, the arms might restrict the maximum attainable strain at the center of the specimen and the extent of the region with uniform stress and strain fields. The second geometry was adopted in another study [118] but a thickness reduction was introduced in the central zone. This design was chosen to achieve the highest strain levels in the central region of an aluminium alloy. Additionally, they incorporated seven parallel slots in each arm of the cruciform specimen to help maintain uniform deformation in the gauge section. During testing, these cruciform specimens were subjected to biaxial stretching, reaching equivalent strains of approximately 15% in the stretching zone.

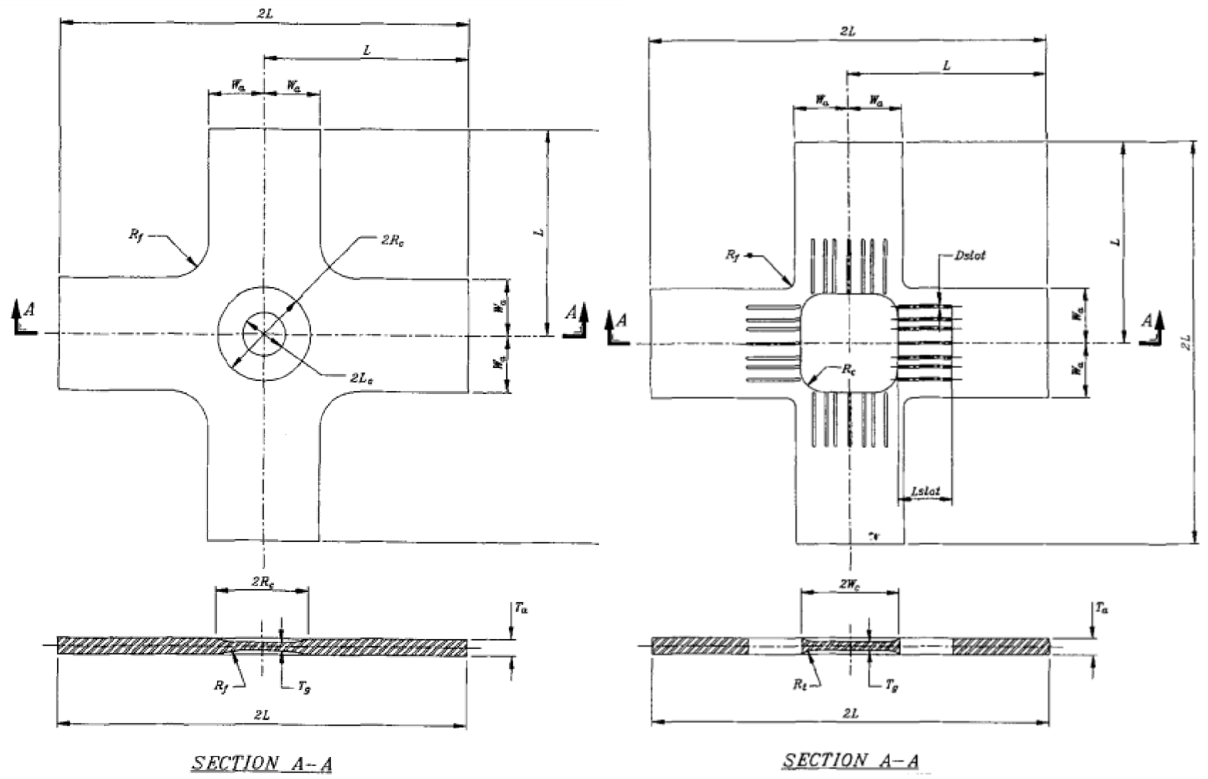

(a) Circular central section/reduced thickness (b) Slots on the arms

Figure 1.30: Geometries of cruciform specimen proposed by Makinde et al. [105] for both metals and composites

Smits et al.[119] conducted a comparative study to investigate the influence of different cruciform specimen geometries on the biaxial failure strain of glass fiber reinforced epoxy laminates ($[(\pm 45/0^\circ)4/\pm 45^\circ]_T$). Their work aimed to identify a suitable specimen geometry for conducting biaxial tests on fiber-reinforced composites at room temperature, providing valuable insights into the testing methodology for these materials. The authors optimized the shape of the corner fillets between the arms along with the size of the milled central area by testing four different geometries. Figure 1.31 shows the optimal geometry that induced the best strain distribution causing failure to occur in the central zone. While the literature often suggests employing thickness thinning methods, an alternative approach proposes maintaining a constant thickness across the specimen to be tested. Some authors propose reinforcing both the arms of the specimen and the regions near the corners between the arms using tabs, typically made from composite material or aluminum. This approach minimizes the need for machining the material in the gauge zone, as only the outer contour of the specimen requires machining, leaving

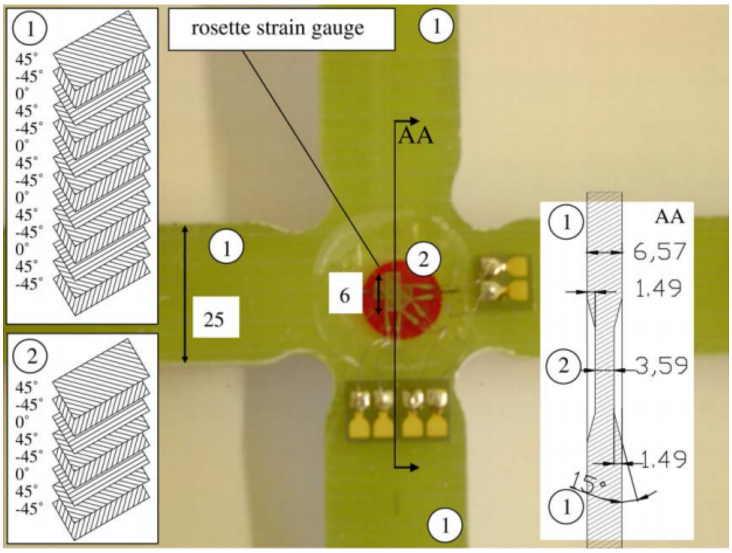

Figure 1.31: Geometries of the cruciform specimens along with the first principle strain results obtained by Digital image Correlation.

the central areas of the tabs accessible for measurements. Hopgood et al.[120] applied this sandwiching method to design the cruciform specimen. The purpose of the study was to obtain the failure envelope of open-holes carbon fiber reinforced epoxy by conducting in-plane biaxial tensile tests at different biaxial strain ratios. Figure 1.32 illustrates the designed specimen. The configuration involves a 2mm thick carbon fiber epoxy test material that is sandwiched between glass fiber composite tabs. In the center of this setup, there is a circular cut-out, exposing the carbon fiber test region for investigation. Kobeissi et al.[121] also used the sandwiching technique to design the in-plane biaxial cruciform specimen. However, the authors promoted the use of aluminum tabs over composite tabs for several reasons. They highlighted the ease of machining metal, the reduced risk of delamination associated with composite tabs, and the metal's ability to withstand larger strains, primarily due to its plasticity. Additionally, the authors supported their design choice through numerical simulations based on Finite Element Method (FEM). These simulations took into account factors such as the specific aluminum alloy chosen for the tabbing material, the thickness of the tabs, and the configuration of the thickness transition. The results of the numerical study were experimentally validated through tests conducted under varying stress states. The designed specimen is presented in Figure 1.33.

In conclusion, non-conventional tests such as in-plane biaxial tensile tests on cruciform

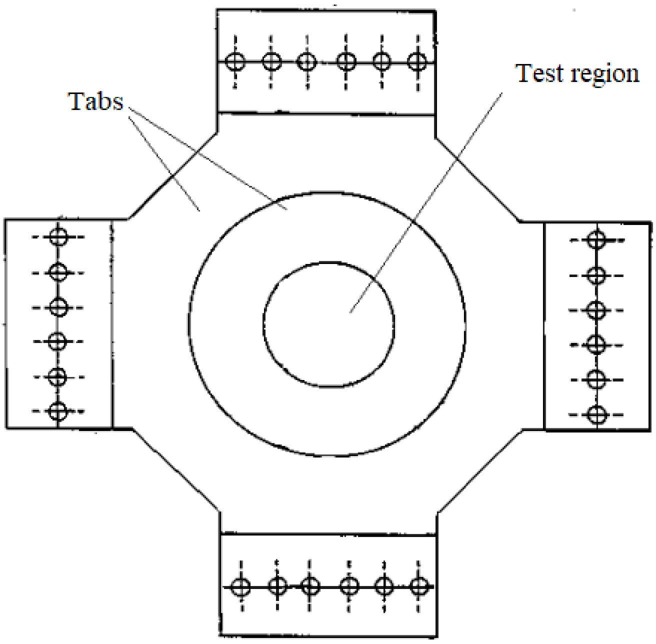

Figure 1.32: Cruciform specimen proposed by Hopgood et al. [120]

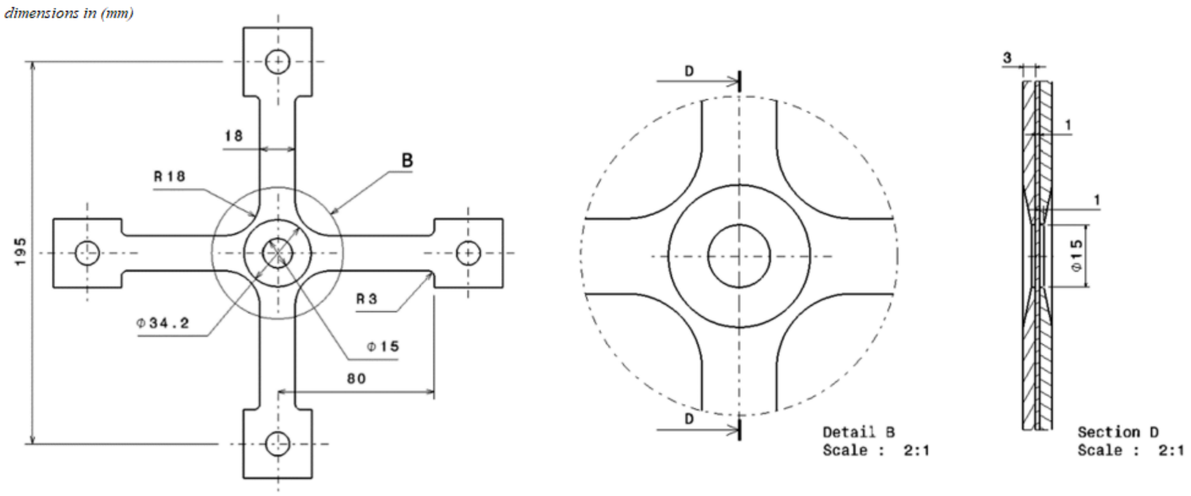

Figure 1.33: Cruciform specimen proposed by Kobeissi et al.[121]

specimens offer advantages over conventional tests when it comes to understanding material behavior under complex loading conditions and for characterizing anisotropic or nonlinear materials.

1.5 Conclusion

To summarize, this chapter discussed the modeling and characterization of composite materials, with a specific focus on the field of discontinuous fiber reinforced thermoplastic polymers.

The combination of various factors influencing the behavior of these composites, such as temperature and strain rate, has been examined. This investigation underscores the complex relationships between external conditions and the material's response, thereby emphasizing the necessity for a careful approach in design and application.

The exploration of manufacturing techniques has revealed the versatile nature of creating these composite structures. The manufacturing landscape offers a diverse array of options, each with its unique advantages and challenges.

A discussion about the modeling approaches was performed to predict the behavior of fiber reinforced thermoplastic polymers. Micro-mechanical models provide a glimpse into the material's internal interactions, while phenomenological models offer a broader perspective on overall behavior. Each modeling approach has its advantages and limitations.

The overview on testing techniques, covering both conventional and non-conventional methods, shows a dedication to accurate material characterization. Specifically, there's a focus on in-plane biaxial testing with cruciform specimens. This approach offers insights into the material's behavior under complex loading scenarios, linking practical situations with lab testing.

Given the advantages and increasing demand for fiber reinforced thermoplastics, it is relevant to examine their mechanical behavior within the scope of this study. This investigation contributes to a better understanding of their suitability for different applications.

The next Chapter will investigate the thermo-mechanical behavior of a discontinuous glass fiber reinforced polypropylene. In a first step, conventional uniaxial tensile tests will be used as characterization tools at given ranges of temperature and strain rate.

CHAPTER 2

UNIAXIAL MECHANICAL CHARACTERIZATION

2.1 Introduction

Uniaxial mechanical characterization of fiber-reinforced polymers (FRPs) plays a vital role in understanding and evaluating the mechanical behavior of these composite materials. By analyzing the resulting stress-strain response, the main mechanical properties e.g. tensile strength, elastic parameters, and strain at failure can be determined. Uniaxial tensile testing is a conventional characterization technique frequently applied for calibrating material models to be implemented in FE simulations. This procedure enhances the predictive accuracy of these models for various engineering applications.

Thermoplastic composites generally exhibit a high sensitivity to temperature as well as strain rate. Anisotropy due to fibers orientation/distribution is also a factor that renders the overall behavior of these material very complex. During manufacturing processes, more precisely heat assisted forming techniques, the material is likely to be subjected to severe conditions such as intermediate to moderate strain rates, high temperatures and/or complex strain paths. Therefore, it is essential to identify material models capable of predicting the complex response of fiber reinforced polymers corresponding to conditions encountered in manufacturing processes. The first step in this work consists in conducting conventional uniaxial tensile tests on glass fiber reinforced polypropylene samples at strain rates of 0.001, 1 and 10 s^{-1} and temperatures of 20, 70 and 120^{o}C. The anisotropy is evaluated by conducting tensile tests with different material orientations. A phenomenological constitutive behavior law is chosen to describe the overall behavior of the thermoplastic composite. The parameters of this model are calibrated based on the experimental results of the uniaxial tensile tests.

2.2 Uniaxial tensile tests

2.2.1 Material and experimental setup

The composite material used in this work is a 40% discontinuous long glass fiber reinforced polypropylene thermoplastic. Injected molded plates of 510x300x2 mm^3 are supplied by SABIC company (Stamax, 40YM240). Uniaxial tensile specimens are extracted by means of a water-jet cutting machine along the 0°, 90° and 45° directions, where the 0° direction represents the length of the plate as illustrated in Figure 2.1. Figure 2.2 shows the dimensions of the uniaxial tensile specimen.

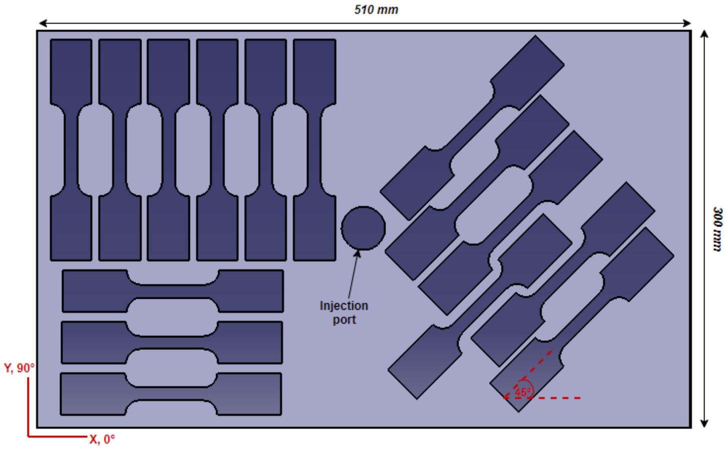

Figure 2.1: Schematic of the injected molded plate showing the orientation of the specimens and their location with respect to the injection port

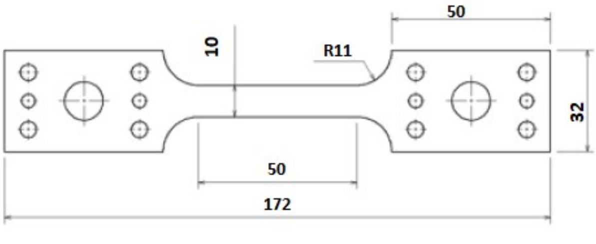

Figure 2.2: Dimensions of uniaxial tensile specimen (in mm)

Uniaxial tensile tests are performed on a hydraulic tensile machine, equipped with a heating system [122]. Load velocities of 0.5, 50 and 500 mm/s are tested, corresponding to initial strain rate values of 0.001, 1 and 10 s^{-1}, respectively. Experiments are carried out at three different temperatures: 20°C (Room temperature RT), 70°C and 120°C. The selected temperature and strain rate ranges for the characterization are directly linked to the conditions of heat forming processes [123], [124]. For the case of polypropylene which is the tested material in this work, the melt temperature is between 165 and 175°C. When conducting tests at elevated temperatures, the specimen is positioned inside an oven and heated until the target temperature is attained. Once this temperature is achieved, the specimen remains in the oven for 10 minutes before starting the test. This ensures that the temperature within the sample is uniformly distributed throughout.

2.2.2 Digital Image Correlation

Strain measurements can be achieved by various conventional techniques such as strain gauges and extensometers. Digital image correlation is an optical full-field measurement technique which is becoming very popular to obtain reliable 2D displacement and strain fields from images of a loaded part. It is applicable not only for metals, but also for polymers such as polymethyl methacrylate (PMMA)[125] as well as for fiber reinforced polymers e.g., Basalt fiber reinforced polypropylene and glass fiber reinforced polypropylene[24], [63]. The images are captured with high-resolution/speed cameras. Image processing is usually achieved by DIC software that use subset-based algorithms (gray-value correlation). It involves dividing the images into smaller subsets and comparing the gray values of each subset before and after deformation in order to determine the displacement. The strain is then calculated by taking the derivative of the displacement field. To perform DIC in this work, a speckle pattern (gray scale) is applied to the surface of the specimen (a white layer is first applied and then sprayed with random black dots). A high-speed/resolution camera (PHOTRON FASTCAM NOVA S9) is fixed perpendicular to the specimen surface along with a proper lighting system ensuring that no surface heating is caused by the light. As mentioned earlier, for high temperature tests, the specimen is placed in the heating chamber. The test is then filmed through a glass door. Therefore, the filming resolution is adjusted for a better quality of the images. GOM Correlate software is used for the correlation procedure. Relying on a DIC guideline [126], a facet size of 21x21 pixels and a point distance of 7 pixels (0.12mm/pixel) are applied. A virtual extensometer is employed to calculate the length change in the region of interest, i.e. calculating the average deformation of the specimen's gauge length as illustrated in Figure 2.3. The use of the virtual extensometer to calculate the average deformation makes the results less sensitive to the correlation parameters.

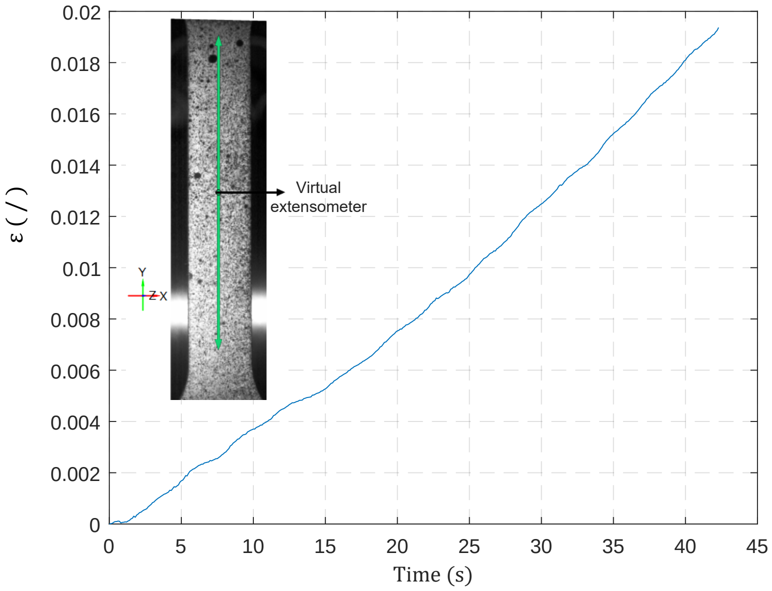

Figure 2.3: Strain measurement using virtual extensometer in DIC Correlate for the uniaxial tensile test at RT and 0.001 s^{-1}

2.2.3 Experimental results

Relying on the uniaxial tensile tests performed in this work, the effect of specimen orientation, strain rate and temperature will be studied. An example of recorded force and strain as a function of time is presented in Figure 2.4, corresponding to the test of a 0° specimen, at RT and quasi-static strain rate of 0.001 s^{-1}. At 42 seconds, failure of the specimen occurs with a resulting force and strain of 1700 N and 1.9%, respectively. The engineering stress-strain curves are then plotted based on these experimental results note: it was verified that there is no difference between the true and the engineering stress-strain curves i.e. negligible difference. Therefore the engineering stress-strain curves will be presented in this work). The repeatability of the results is verified with three tests conducted at each condition. An example is illustrated in Figure 2.5 showing the repeatability of the stress-strain curves resulting from three tests performed at the same experimental conditions (at RT and quasi-static strain rate of 0.001 s^{-1}). All specimens are extracted from the same position relative to the injection port as illustrated in the figure. The error bars represent the standard deviation calculated from the three tests. Repeatability is achieved for all the tested conditions.

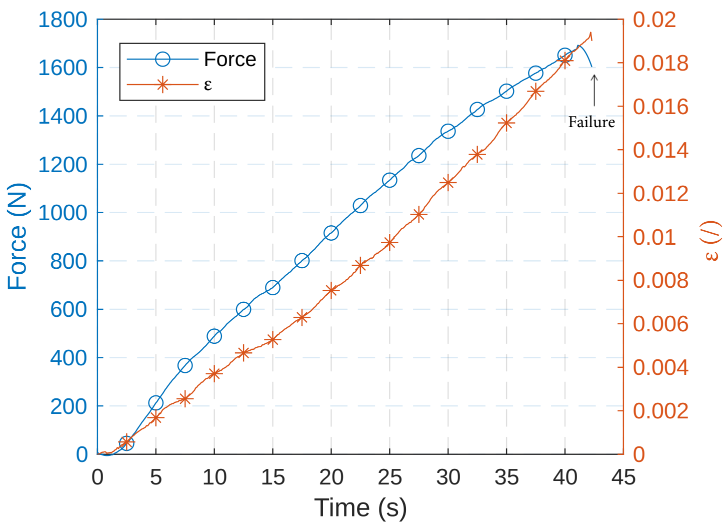

Figure 2.4: Uniaxial force vs. time and longitudinal strain vs. time curves obtained experimentally at RT and quasi-static loading velocity

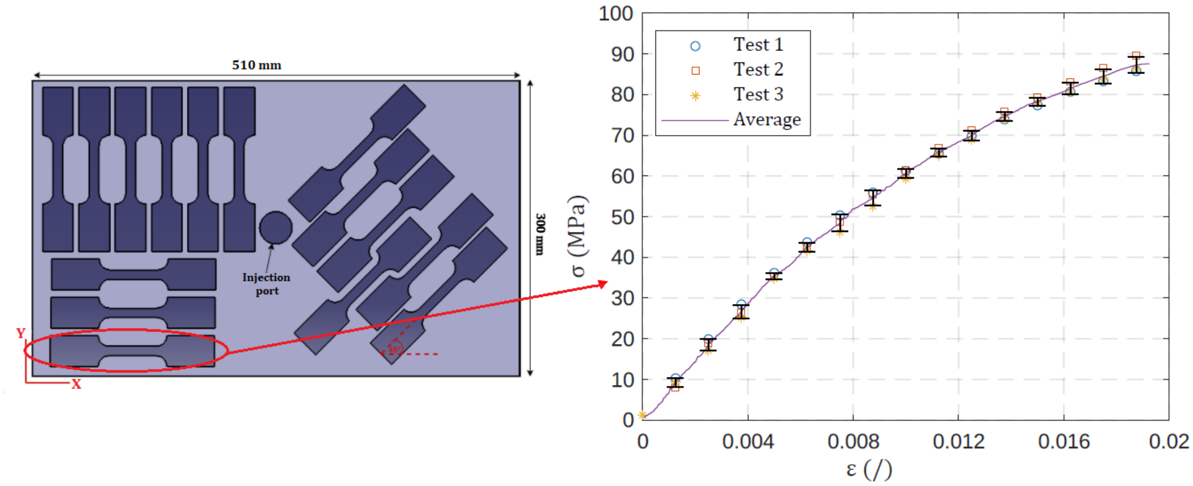

Figure 2.5: Repeatability tests conducted at RT and $0.001s^{-1}$

2.2.3.1 Effect of specimen orientation

The stress-strain curves of discontinuous glass fiber reinforced polypropylene are plotted, at RT and quasi-static strain rate of 0.001 s^{-1}, for specimens extracted from three different orientations: i) along the length of the plate 0°, ii) along the transverse direction 90° and iii) with an angle of 45°, as shown in Figure 2.6. Figure 2.6 shows a clear influence of the material orientation. The stiffness of the specimen along the transverse direction, i.e 90°, is the lowest one, corresponding to the lower curve. The stiffness of the specimen at 45° is located between the longitudinal and transverse direction specimen stiffness. Moreover, the ultimate strength decreases with the increase of the specimen orientation angle. The maximum strength accounts for the longitudinal direction for a value of 91 MPa. On the other hand, the elongation at failure increases when the angle increases; it reaches a value of 2.3% for the transverse direction specimen, i.e for 90° direction. This behavior is thought to be related to the manufacturing of the part and the induced fibers orientation/distribution, given that the plates are rectangular and the injection port is located in the middle. The discontinuous fibers are more likely to be oriented in a certain direction. In this case, it is along the length of the plate i.e. 0° direction in which the velocity of the material flow is higher during the injection process. Table 2.1 summarises the tensile properties (Young's modulus E, the ultimate tensile strength σ_{ult} and the strain at failure ε_f) determined at RT and 0.001s^{-1} for three different material orientations. Note that all these properties are determined according to ISO-527 [127], e.g. Young's modulus is evaluated within the strain range of 0.05% to 0.25%. The value of E is then determined as the slope of the linear regression line fitted to the stress-strain relationship within this specific strain interval.

Table 2.1: Tensile properties at three different material orientations

Orientation		$T = 20°C$	
	$E(MPa)$	$\sigma_{ult}(MPa)$	$\varepsilon_f(\%)$
0°	7428	91	1.94
45°	5686	64	2.09
90°	4122	52	2.3

2.2.3.2 Effect of position with respect to injection port

In order to check the effect of the fibers distribution in the plate, different specimens were selected from different positions relative to the injection port along the transverse (90 °) direction as shown in Figure 2.7. The same effect is monitored along the 45° direction as illustrated in Figure 2.8, but this time only a specimen located the furthest away from the injection port is selected to be compared with the nearest two. The results show that the stress-strain response of the material is affected by the position of the tested specimen with respect the the injection port. This is related to the fact that the distribution of the fibers may not be homogeneous throughout the plate i.e. the fibers would be more concentrated in regions that are the closest to the injection port.

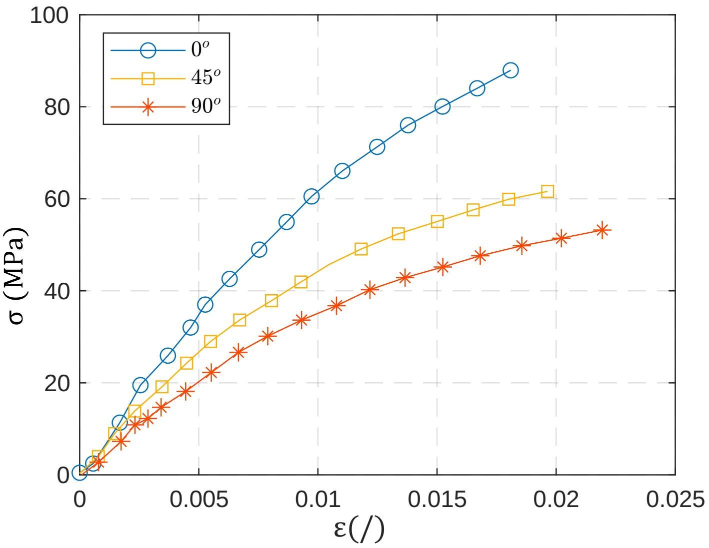

Figure 2.6: Uniaxial stress-strain curves at room temperature and quasi-static strain rate for three different orientations 0°, 45° and 90°

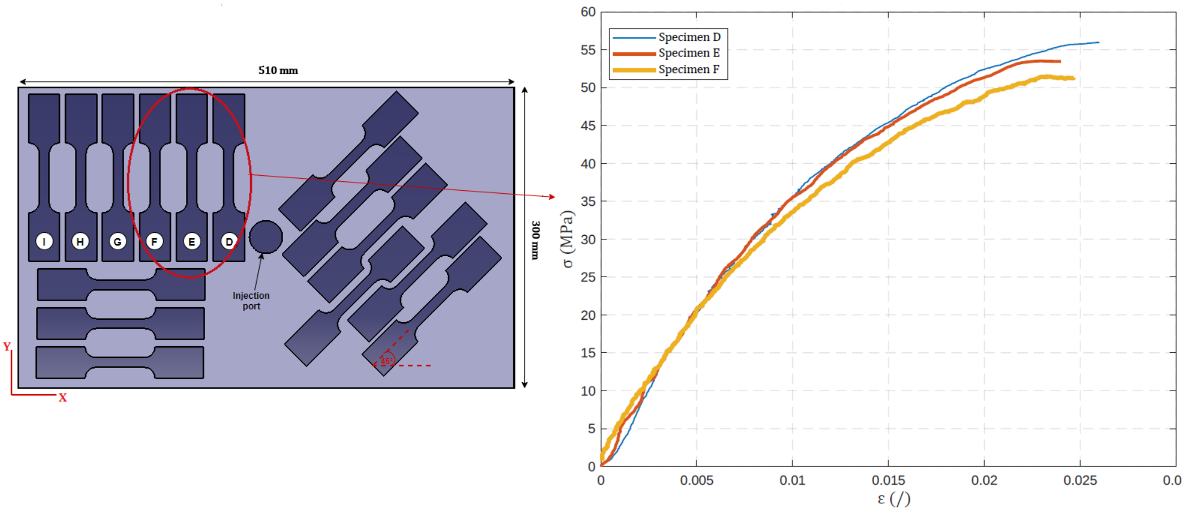

Figure 2.7: Effect of specimen location with respect to injection port for the tests conducted at RT and $0.001s^{-1}$, along the transverse 90° direction

According to the results, it is evident that the orientation and position of the specimen within the plate have an influence on the stress-strain behavior. To accurately identify the effects of temperature and deformation rate (in the following sections), the specimens are taken from the same location, as indicated previously in Figure 2.5.

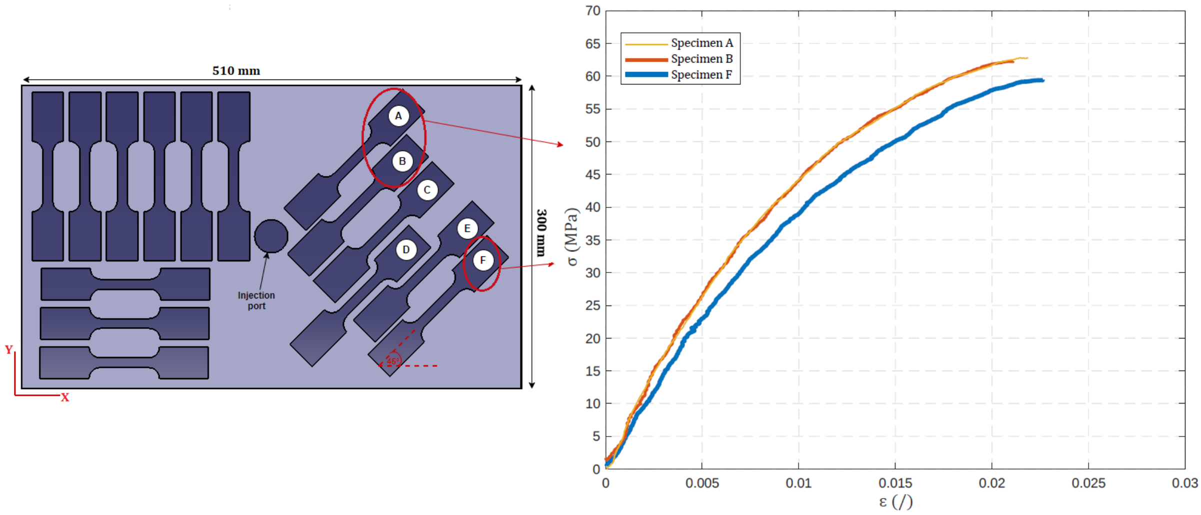

Figure 2.8: Effect of specimen location with respect to injection port for the tests conducted at RT and 0.001s^{-1}, along the 45° direction

2.2.3.3 Effect of strain rate

The investigation of the strain rate effect is performed using specimens extracted from the longitudinal direction. Figure 2.9 shows the resulting stress-strain curves at different temperatures: T =20°C , T = 70°C and T = 120°C in Figures 2.9a, 2.9b and 2.9c, respectively. For each tested temperature, three different deformation rates are considered: 0.001, 1, and 10 s^{-1}. Results showed that Young's modulus and the ultimate strength increase with the strain rate, for all temperature conditions. Inspecting Figure 2.9a, it is clear that when considering 0.001s^{-1} as a reference strain rate , σ_{ult} increases by 16% and 43% if the value of the reference rate is multiplied by a factor of 10^3 and 10^4, respectively. The resultant highest ultimate strength is then 130 MPa while the strength corresponding to 0.001s^{-1} is 91 MPa. However, the strain at failure and Young's modulus. Compared to the lowest strain rate, a small increase of 7% and 14% is noticed in the elongation at failure ε_f and Young's modulus E, respectively, at the highest strain rate. Note that for all stress-strain curves presented in this work, the end point of each curve corresponds to the failure of the specimen.

For the temperatures T = 70°C and T = 120°C (Figure 2.9b and Figure 2.9c), respectively, the strength and the stiffness increase also with the velocity. However, despite the clear difference between the curves corresponding to the 0.001s^{-1} and 1s^{-1}, the curves corresponding to 1s^{-1} and 10s^{-1} are relatively close. This shows that the sensitivity of the tested thermoplastic material to the strain rate becomes low at high temperatures.

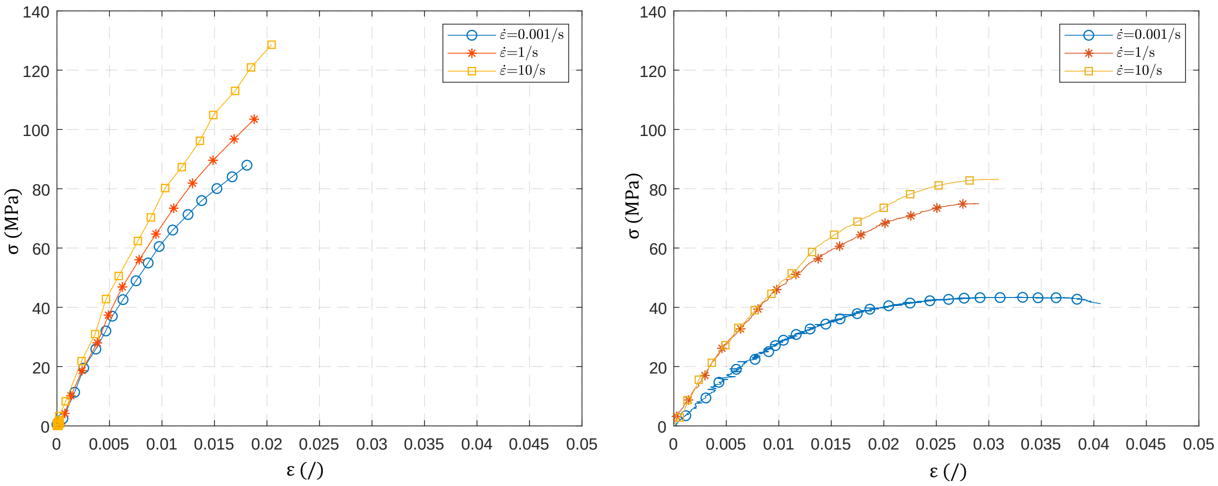

(a) T = 20°C (b) T = 70°C

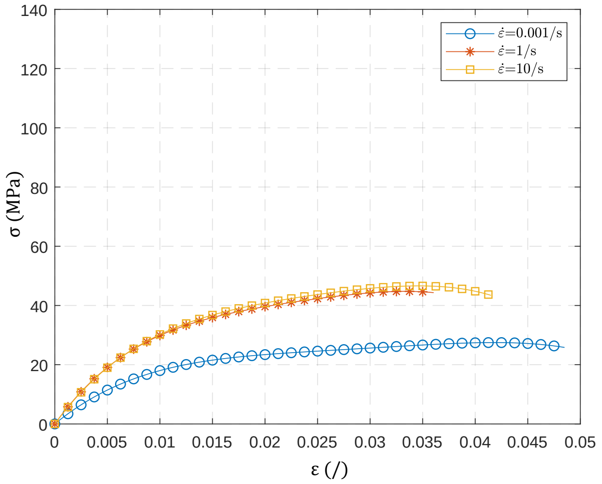

(c) T = 120°C

Figure 2.9: Effect of strain rate on the behavior for three different temperatures

Note that for a strain rate of $0.001s^{-1}$, high elongations at failure of 4.1% and 4.7% are obtained for T = 70°C and T = 120°C, respectively.

Table 2.2 summarizes the different values of the tensile properties as a function of the strain rate for the three tested temperatures such as the ultimate stress, the elongation at failure and Young's modulus.

Table 2.2: Effect of strain rate and temperature on the tensile properties

$\dot{\varepsilon}(s^-1)$	E(MPa)	σ_{ult} (MPa)	ε_f (%)
$T = 20°C$			
0.001	7428	91	1.94
1	8140	107	1.96
10	9188	130	2.08
$T = 70°C$			
0.001	3454	41	4.06
1	5507	75	2.9
10	5946	84	3.09
$T = 120°C$			
0.001	2515	25	4.85
1	4215	45	3.6
10	4166	43.5	4.17

2.2.3.4 Effect of temperature

It is important to study the effect of temperature on the mechanical behavior of the tested reinforced thermoplastic material. The uniaxial tests already performed in the previous section are presented in this section as a function of the temperature. Figure 2.10a, Figure 2.10b and Figure 2.10c show the stress-strain curves corresponding to deformation rates of 0.001, 1 and 10 s^{-1}, respectively. On these curves, the effect of temperature is clearly seen.

For a quasi-static uniaxial test ($0.001s^{-1}$), the ultimate strength decreases from 91 to 30 MPa while the elongation at failure increases from 2% to 4.8%. Also, when increasing the temperature, the stiffness decreases, for the three tested strain rates. This shows the clear effect of the temperature on the behavior of the glass fiber reinforced polypropylene.

Finally, Figure 2.11 illustrates the combined effect of both temperature and strain rate on the tensile mechanical properties.

Figure 2.11a shows the combined effect on Young's modulus E in the longitudinal direction. The stiffness increases with the velocity but decreases when the temperature increases. On the other hand, the ultimate tensile strength σ_{ult} decreases also when the temperature increases; while it remains almost constant at high temperature (70 and 120°C) and high strain rates (1 and 10 mm/s), as shown in Figure 2.11b. In Figure 2.11c, the elongation at failure increases clearly with the temperature. This elongation presents lower values for a strain rate of 1 s^{-1} , at temperatures of 70 and 120°C.

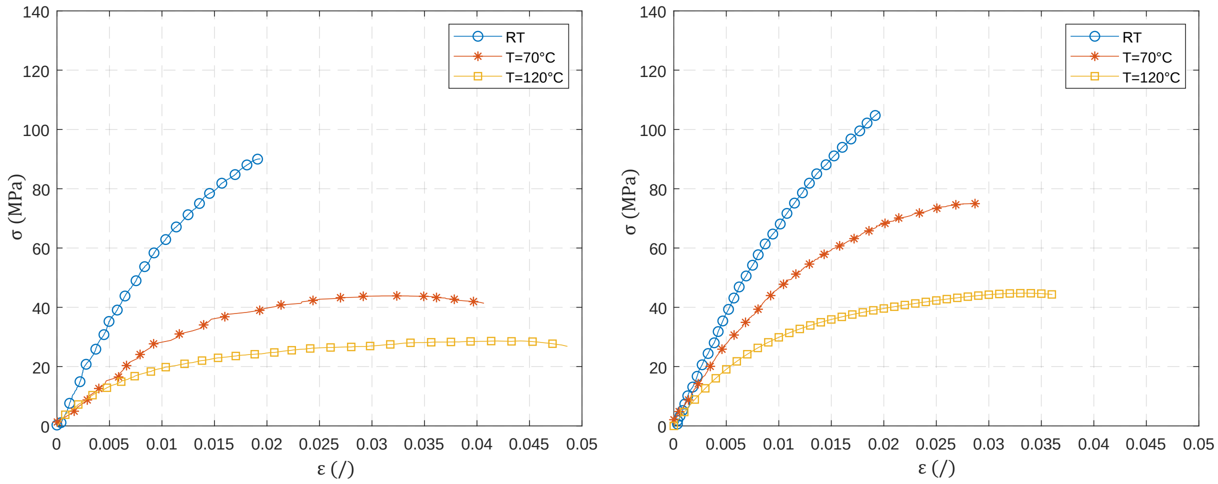

(a) $\dot{\varepsilon} = 0.001 s^{-1}$

(b) $\dot{\varepsilon} = 1 s^{-1}$

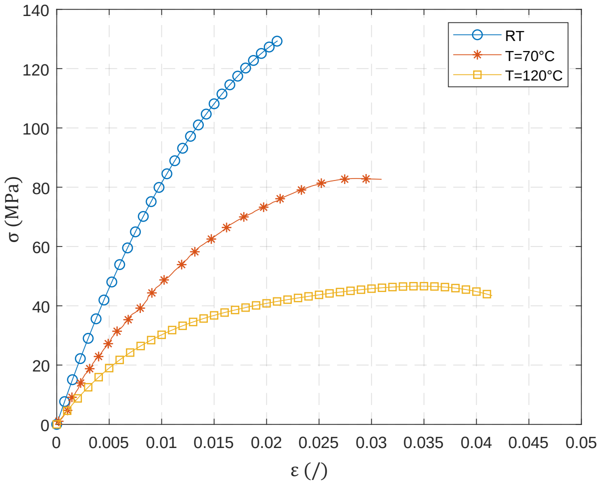

(c) $\dot{\varepsilon} = 10 s^{-1}$

Figure 2.10: Effect of temperature for three different strain rates

2.3 Identification of phenomenological material model

2.3.1 Constitutive model

The experimental investigations underlined the significant effect of strain rate and temperature on the mechanical behavior of discontinuous glass fiber reinforced polypropylene.

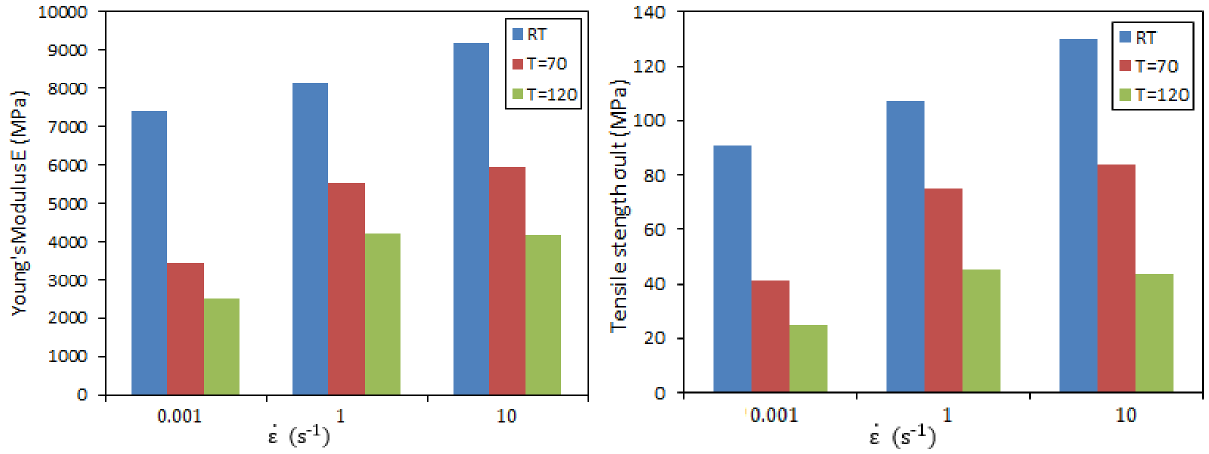

(a) Young's modulus E (b) σ_{ult}

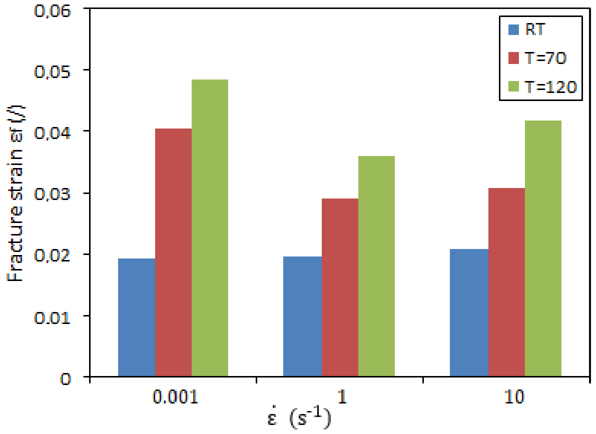

(c) ε_f

Figure 2.11: Effect of temperature and strain rate on the tensile properties

In this section, the phenomenological constitutive model of G'Sell and Jonas [71], [128] is selected to describe the behavior of the studied material. This model was originally designed to describe the behavior of semi-crystalline polymers. In this work, a modification of the constitutive equation is proposed for a better description of the observed experimental behavior. In a first step, the material parameters of the model are initially calibrated based on the uniaxial tensile test results performed on specimens along the 0° orientation. The anisotropy is integrated, in the following section, once the model is validated for the longitudinal direction. The original constitutive equation of the model is stated in equation 2.1 as:

$$\bar{\sigma}(\bar{\varepsilon},\dot{\bar{\varepsilon}}) = K \cdot \exp\left(h\bar{\varepsilon}^2\right)\left(1-\exp(-W\bar{\varepsilon})\right) \cdot \dot{\bar{\varepsilon}}^m \tag{2.1}$$

Behavior at low strain levels is represented by the term $(1 - \exp(-W\varepsilon))$. The term $\exp\left(h\bar{\varepsilon}^2\right)$ represents the stiffening of the material at large deformations [22]. This last term is neglected (h = 0) in this work due to the low level of deformation at failure observed from the experimental results. Additionally, the effect of the temperature can be incorporated in the model by performing a temperature sensitivity analysis for the material parameters and expressing them as a function of temperature. Therefore, the constitutive equation considered in this work becomes (equation 2.2):

$$\bar{\sigma}(\bar{\varepsilon}, \dot{\bar{\varepsilon}}, T) = K(T) \cdot (1 - \exp(-W(T) \cdot \bar{\varepsilon})) \cdot \dot{\bar{\varepsilon}}^{m(T)} \tag{2.2}$$

As proposed in many studies ([22], [129]–[132]), the equation of the model can be modified to clearly separate the linear and non-linear behaviors. Consequently, in this work, the constitutive equation of the model is modified as stated in equation 2.3:

$$\begin{cases} \bar{\sigma}(\bar{\varepsilon}, \dot{\bar{\varepsilon}}, T) = E(\dot{\bar{\varepsilon}}, T) \cdot \bar{\varepsilon} & \text{for } \bar{\sigma} < \sigma_{\mathrm{y}} \\ \bar{\sigma}(\bar{\varepsilon}_p, \dot{\bar{\varepsilon}}, T) = \sigma_{\mathrm{y}}\left(\dot{\bar{\varepsilon}}, T\right) + K(T) \cdot \left(1 - \exp\left(-W(T).\bar{\varepsilon}_p\right)\right) \dot{\bar{\varepsilon}}^{m(T)} & \text{for } \bar{\sigma} > \sigma_{\mathrm{y}} \end{cases} \tag{2.3}$$

The approach adopted to identify the initial yield strength σ_y and the equivalent plastic deformation $\bar{\varepsilon}_p$ is presented in section 2.3.1.1.

According to equation 2.3, there are 5 parameters to be determined for the material model defined in equation 2.3: $E(\dot{\bar{\varepsilon}}, T)$, $\sigma_y(\dot{\bar{\varepsilon}}, T)$, $m(T)$ $K(T)$, and $W(T)$. The values of $E(\dot{\bar{\varepsilon}}, T)$ were determined previously and detailed in Table 2.2. The remaining parameters will be determined in the following sections.

2.3.1.1 Determining the initial yield stress σ_y

Given E, $\bar{\varepsilon}$ and $\bar{\sigma}$ for each temperature and strain rate condition, the equivalent plastic deformation is calculated as:

$$\bar{\varepsilon}_p = \bar{\varepsilon} - \frac{\bar{\sigma}}{E} \tag{2.4}$$

Relying on equation 2.4, it is assumed that σ_y corresponds to the point at which $\bar{\varepsilon}_p$ becomes greater than zero. In other words, it's the point on the stress-strain curve where the material starts to exhibit permanent deformation. Table 2.3 summarizes the values of σ_y at different strain rates and temperatures. As expected, the values of this parameter exhibit a decrease as temperature rises for a given initial strain rate. Conversely, they show an increase with higher strain rate for a certain temperature condition. For instance, an increase in the temperature from RT to 120°C causes a 70% decrease in σ_y, for an initial strain rate of 0.001s^{-1}. Also, at RT, σ_y increases by 30% when raising the initial strain rate from 0.001s^{-1} to 10s^{-1}.

Table 2.3: σ_y determined for all the tested conditions

$\dot{\varepsilon}(s^-1)$	σ_y (MPa)
$RT(T = 20°C)$	
0.001	29.4
1	33
10	38.1
$T = 70°C$	
0.001	13
1	20
10	22.3
$T = 120°C$	
0.001	8.65
1	13
10	14.6

2.3.1.2 Determining the strain rate sensitivity m

The strain rate sensitivity m is determined in the non-linear region (equation 2.5) as the slope of the plot $\ln(\bar{\sigma}(\bar{\varepsilon}_p, \dot{\varepsilon}, T) - \sigma_y(\dot{\varepsilon}, T))$ vs. $\ln \dot{\varepsilon}$, at a given temperature T and a plastic strain level $\bar{\varepsilon}_p$, as stated in equation (2.6).

$$\bar{\sigma}(\bar{\varepsilon}_p, \dot{\varepsilon}, T) - \sigma_y(\dot{\varepsilon}, T) = K(T)\left(1 - \exp\left(-W(T)\bar{\varepsilon}_p\right)\right)\dot{\varepsilon}^m \tag{2.5}$$

$$m = \left.\frac{\partial \ln\Big(\bar{\sigma}(\bar{\varepsilon}_p, \dot{\varepsilon}, T) - \sigma_y(\dot{\varepsilon}, T)\Big)}{\partial \ln \dot{\varepsilon}}\right|_{\bar{\varepsilon}_{p,T}} \tag{2.6}$$

The value of the strain rate sensitivity parameter m is assumed constant for all strain levels and an average value of m can be considered as suggested by ([71], [128]). In this work, four different strain levels are selected:

- 25% of total $\bar{\varepsilon}_p$,
- 50% of total $\bar{\varepsilon}_p$,
- 75% of total $\bar{\varepsilon}_p$,
- 95% of total $\bar{\varepsilon}_p$.

An example for determining m at RT is shown in Figure 2.12. The strain rate sensitivity for each strain level corresponds to the line slopes. The average of these values represents the overall strain rate sensitivity m at the given temperature. In the same manner, the obtained values of m at T=70°C and T=120 °C are 0.074 and 0.07, respectively. The values obtained for m show that for elevated temperatures (70°C and 120°C), the sensitivity to strain rate becomes similar which clearly shown in the stress-strain curves presented in Figure 2.9.

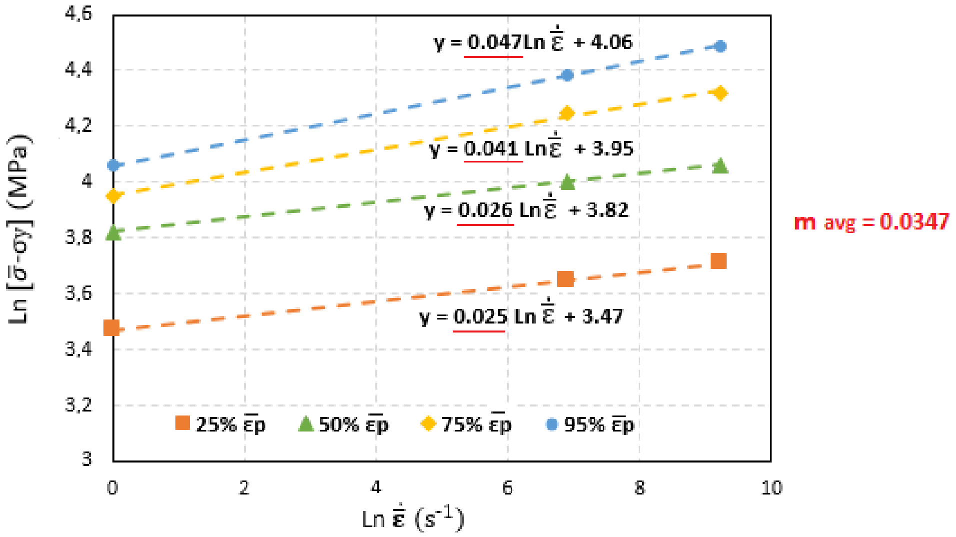

Figure 2.12: Determining the value of the strain rate sensitivity m at RT

2.3.1.3 Determining K and W

After determining σ_y and m analytically, K and W are identified using a nonlinear optimization function. The cost function to be minimized is defined by the error δ as follows,

$$\delta = \min \sum_{i=1}^{n} \left(\sigma_{\text{model}} - \sigma_{\text{experimental}}\right)^2 \tag{2.7}$$

Where n is the total number of data points, σ_{model} is the predicted stress stated in equation 2.5, and $\sigma_{experimental}$ is the stress measured experimentally. The values of K and W for each temperature are summarized in Table 2.4.

2.3.1.4 Temperature and strain rate sensitivity analysis of E

The temperature and strain rate sensitivity of the linear part represented by $\sigma = E(\dot{\bar{\varepsilon}}, T) \cdot \bar{\varepsilon}$ in equation 2.3 is addressed by two different approaches. The first consists in describing

Table 2.4: Parameters K and W determined at temperatures T=20°C, T=70°C, and T=120°C

$T(°C)$	$K[MPa]$	$W[/]$
20	80	419.5
70	51.3	290.7
120	27.3	212.9

the strain rate sensitivity independently from the one defined for the non-linear part. The second approach consists in considering the same strain rate sensitivity with the parameter m determined for the non-linear part. In both approaches the temperature variation is modeled using the physical Arrhenius relation proposed by [22].

$$E(T) = E_0 \cdot \exp\left[A_E\left(\frac{1}{T} - \frac{1}{T_g}\right)\right] \tag{2.8}$$

Where E_0 and A_E are material constants, T the temperature and T_g the glass transition temperature. The latter is known to be around -10°C (according to [26], [133], [134] the glass transition region of glass fiber reinforced polypropylene is between -25 to 10°C).

A. Approach 1 to determine $E(\dot{\varepsilon}, T)$

First, the temperature sensitivity of E is studied. The parameters E_0 and A_E of equation 2.8 are calibrated based on the experimental values obtained for each tested strain rate, i.e., 0.001, 1 and $10s^{-1}$. Therefore, three sets of E_0 and A_E are obtained as listed in Table 2.5. For each strain rate, the variation of E with respect to temperature is plotted in Figure 2.13 illustrating the experimental and calculated values.

Table 2.5: Temperature sensitivity parameters determined in approach 1

$\dot{\varepsilon}(s^{-1})$	$E_0(MPa)$	A_E
0.001	11605	1266.5
1	12226	900
10	12710	875

Variations of the parameters E_0 and A (listed in Table 2.5) are approximated by means of power function with respect to $\dot{\varepsilon}$, as shown in Figure 2.14. Consequently, the strain rate and temperature sensitivity of Young's modulus E is modeled as follows:

$$E(\dot{\varepsilon}, T) = (E_1 \cdot \dot{\varepsilon}^n) \cdot \exp\left[(A_{E'} \cdot \dot{\varepsilon}^p)\left(\frac{1}{T} - \frac{1}{T_g}\right)\right] \tag{2.9}$$

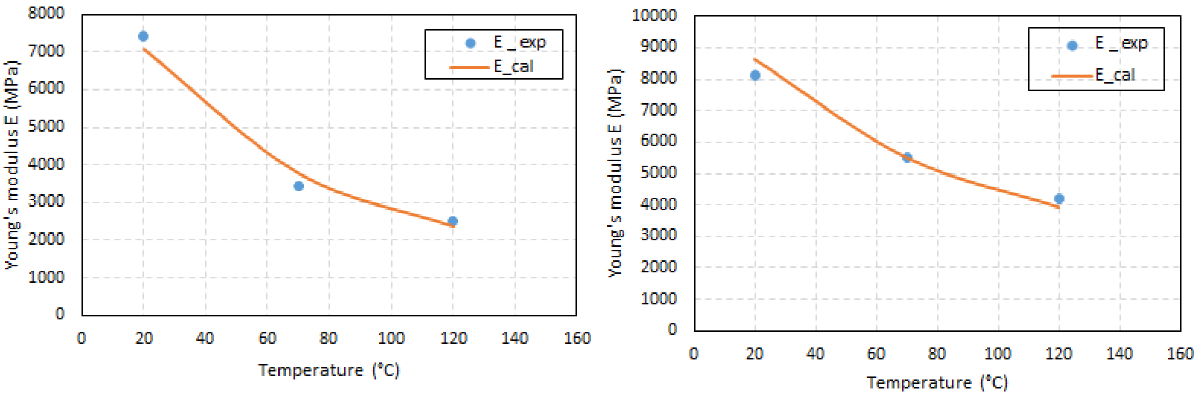

(a) $\dot{\varepsilon} = 0.001\ s^{-1}$ (b) $\dot{\varepsilon} = 1\ s^{-1}$

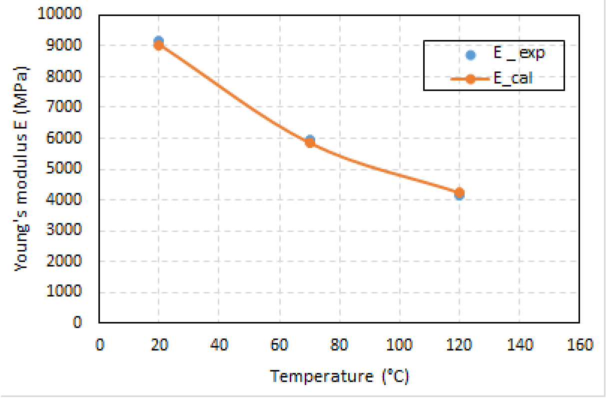

(c) $\dot{\varepsilon} = 10\ s^{-1}$

Figure 2.13: Temperature sensitivity of Young's modulus: experimental vs calculated using equation 2.8

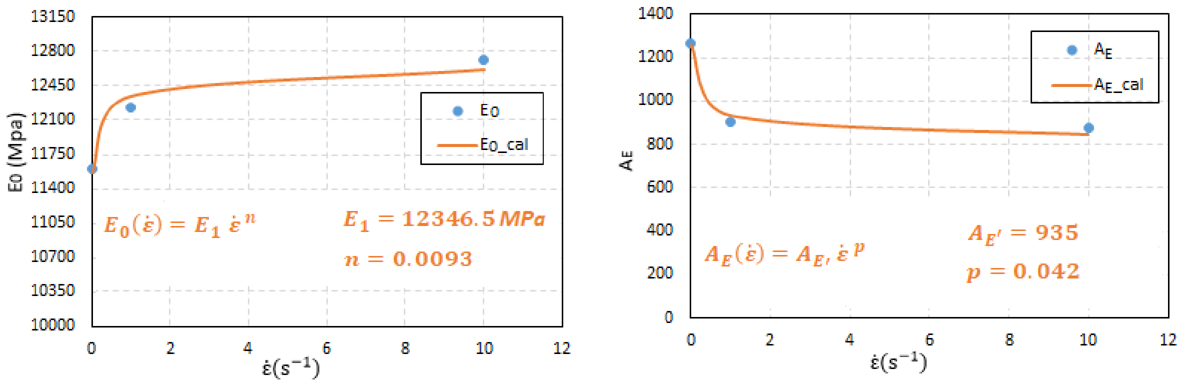

(a) Strain rate sensitivity of E_0 (b) Strain rate sensitivity of A_E

Figure 2.14: Strain rate sensitivity of Young's modulus represented by E_0 and A_E

Table 2.6 provides a comparison between the experimental and calculated values of E using equation 2.9, showing the relative percent error for each condition.

Table 2.6: Comparison between experimental and calculated values of Young's modulus in Approach 1

$\dot{\varepsilon}(s^{-1})$	$T(°C)$	$E^{exp}(Mpa)$	$E^{model}(MPa)$	Error (%)
0.001	20	7428	7105	4.4
	70	3454	3808	10.26
	120	2515	2392	4.88
1	20	8140	8579	5.4
	70	5507	5388	2.15
	120	4215	3809	9.62
10	20	9188	9068	1.3
	70	5946	5947	0.026
	120	4166	4342	4.24

B. Approach 2 to determine $E(\dot{\varepsilon}, T)$

The second approach consists in assuming that the strain rate sensitivity for the linear part is the same than for the non-linear part, i.e. the parameter m representing the strain rate sensitivity will be introduced in the linear part. The same Arrhenius equation defined previously is adopted in this second approach. Therefore, the model to be calibrated based on the experimental values of Young's modulus is defined as stated in equation 2.10,

$$E(\dot{\varepsilon}, T) = E_0(T) \cdot \dot{\varepsilon}^{m(T)} \tag{2.10}$$

At each temperature (20, 70 and 120°C), the parameter E_0 is calibrated. The values are presented in Table 2.7. The temperature sensitivity of the parameter E_0 is approximated by the physical Arrhenius equation as follows,

Table 2.7: Parameter $E_0(MPa)$ for each temperature

$T(°C)$	m	$E_0(MPa)$
20	0.0347	8621
70	0.074	5390
120	0.07	3901

$$E_0(T) = E_1 \cdot \exp\left[A_E\left(\frac{1}{T} - \frac{1}{T_g}\right)\right] \tag{2.11}$$

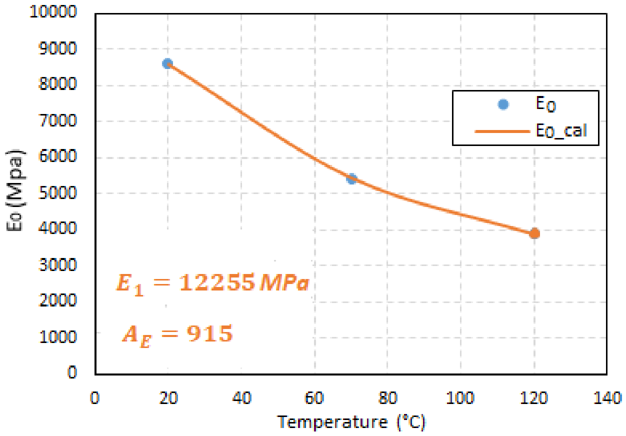

Figure 2.15: Temperature sensitivity of parameter E_0: calibration of E_1 and A_E

Where E_1 and A_E are constants to be calibrated based on the experimental values as shown in Figure 2.15. Consequently, the overall equation representing the strain rate and temperature sensitivity of Young's modulus using Approach 2 is stated below,

$$E(\dot{\varepsilon}, T) = E_1 \cdot \exp\left(A_E\left(\frac{1}{T} - \frac{1}{T_g}\right)\right) \cdot \dot{\varepsilon}^{m(T)} \tag{2.12}$$

Table 2.8 provides a comparison between the experimental values of Young's modulus and the values calculated using equation 2.12 proposed in Approach 2.

Table 2.8: Comparison between experimental and calculated values of Young's modulus for Approach 2

$\dot{\varepsilon}(s^{-1})$	$T(^oC)$	$E^{exp}(MPa)$	$E^{model}(MPa)$	$Error(\%)$
0.001	20	7428	6753	9
	70	3454	3265	5.45
	120	2515	2391	4.92
1	20	8140	8583	5.44
	70	5507	5444	1.13
	120	4215	3878	8
10	20	9188	9297	1.18
	70	5946	6456	8.58
	120	4166	4556	9.37

Both approaches give good approximations for Young's modulus. Approach 2 will be selected in this work to represent the temperature and strain rate sensitivity of E. This approach showed that the strain rate sensitivity that was already determined for the non-linear part can also give good prediction of the strain rate sensitivity related to the small linear part involved.

Following the same principle of approach 2, the sensitivity of the yield stress σ_y to strain rate and temperature is determined as follows,

$$\sigma_y(\dot{\bar{\varepsilon}}, T) = \sigma_{y_0}(T) \cdot \dot{\bar{\varepsilon}}^{m(T)} \tag{2.13}$$

$\sigma_{y_0}(T)$ (values listed in Table 2.9) is calibrated based on equation 2.14. The correlation of this parameter (values in Table 2.9) with equation 2.14 is presented in Figure 2.16.

Table 2.9: Parameter σ_{y0} at each temperature

$T(^oC)$	m	$\sigma_{y0}(MPa)$
20	0.0347	35
70	0.074	20.3
120	0.07	13.5

$$\sigma_{y0}(T) = \sigma_{y1} \cdot \exp\left(A_{\sigma y}\left(\frac{1}{T} - \frac{1}{T_g}\right)\right) \tag{2.14}$$

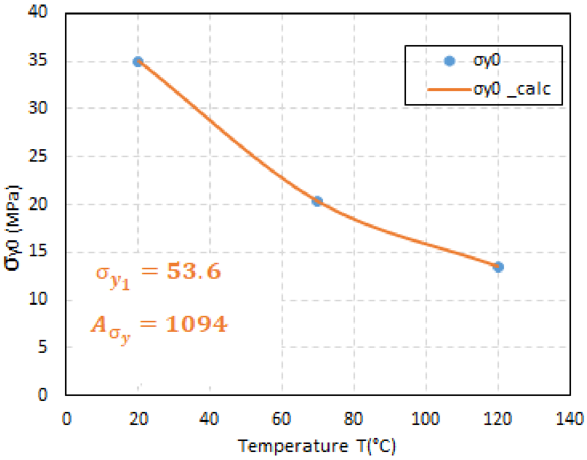

Figure 2.16: Temperature sensitivity of parameter σ_{y0}: calibration of σ_{y1} and $A_{\sigma y}$

The overall equation that defines the strain rate and temperature sensitivity of the yield stress $\sigma_y(\dot{\varepsilon}, T)$ becomes:

$$\bar{\sigma}_y(\dot{\bar{\varepsilon}}, T) = \sigma_{y1} \cdot \exp\left(A_{\sigma y}\left(\frac{1}{T} - \frac{1}{T_g}\right)\right) \cdot \dot{\bar{\varepsilon}}^{m(T)} \tag{2.15}$$

Table 2.10 provides a comparison between the experimental and calculated values of the yield stress using equation 2.15, showing the relative percent error for each condition.

Table 2.10: Comparison between experimental and calculated values of the yield stress in Approach 2

$\dot{\varepsilon}(s^{-1})$	$T(^oC)$	$\sigma_y{}^{exp}(MPa)$	$\sigma_y{}^{model}(MPa)$	$Error(\%)$
0.001	20	29.37	27.5	6.36
	70	12.97	12.17	6.17
	120	8.65	8.34	3.58
1	20	33	35	6.06
	70	20.9	20.3	2.87
	120	14.5	13.5	6.8
10	20	38.1	37.9	0.52
	70	22.3	24	7.6
	120	14.6	15.9	8.9

The parameters W and K, their temperature sensitivity can be approximated following the same evolution adopted for E as given in equations 2.16 and 2.17, respectively.

$$W(T) = W_0 \cdot \exp\left[A_W\left(\frac{1}{T} - \frac{1}{T_g}\right)\right] \tag{2.16}$$

$$K(T) = K_0 \cdot \exp\left[A_K\left(\frac{1}{T} - \frac{1}{T_g}\right)\right] \tag{2.17}$$

Figures 2.17a, 2.17b present the comparison between experimental and calculated values of W and K, respectively.

The temperature sensitivity of the parameters W and K can also be approximated by a linear variation as shown in Figures 2.18a, 2.18b.

Keeping the same trend for the temperature variation, equations 2.16 and 2.17 will be adopted for W and K in the generalized form of the constitutive equation. The latter is then written as:

$$\begin{cases} \bar{\sigma}(\bar{\varepsilon}, \dot{\bar{\varepsilon}}, T) = E_1 \cdot \exp\left(A_E\left(\frac{1}{T} - \frac{1}{T_g}\right)\right) \cdot \dot{\bar{\varepsilon}}^{m(T)} & \text{for } \bar{\sigma} < \sigma_{\text{y}} \\ \bar{\sigma}(\bar{\varepsilon}_p, \dot{\bar{\varepsilon}}, T) = \sigma_{y1} \cdot \exp\left(A_{\sigma y}\left(\frac{1}{T} - \frac{1}{T_g}\right)\right) \cdot \dot{\bar{\varepsilon}}^{m(T)} + & \\ K_0 \cdot \exp\left(A_K\left(\frac{1}{T} - \frac{1}{T_g}\right)\right) \cdot \left(1 - \exp\left(-W_0 \cdot \exp\left(A_W\left(\frac{1}{T} - \frac{1}{T_g}\right)\right) \cdot \bar{\varepsilon}_p\right)\right) \cdot \dot{\bar{\varepsilon}}^{m(T)} & \text{for } \bar{\sigma} > \sigma_{\text{y}} \end{cases} \tag{2.18}$$

Where the constants E_1, A_E, σ_{y1}, $A_{\sigma y}$, K_0, A_K, W_0 and A_W are listed in Table 2.11. Equation 2.18 will be used in the FE simulations to take into account the effect of temperature

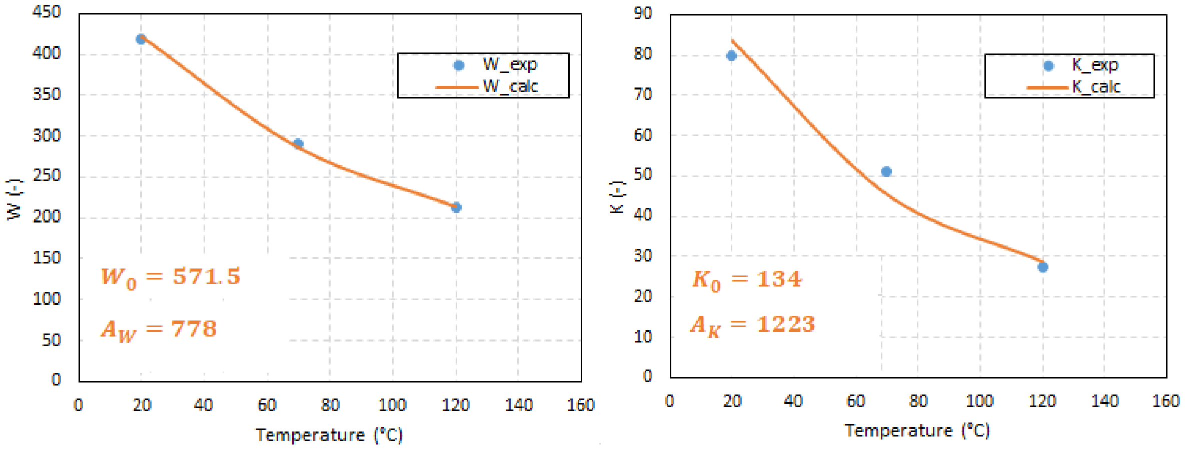

(a) Temperature sensitivity of W (b) Temperature sensitivity of K

Figure 2.17: Temperature sensitivity of W and K represented by the Arrhenius equations 2.16 and 2.17.

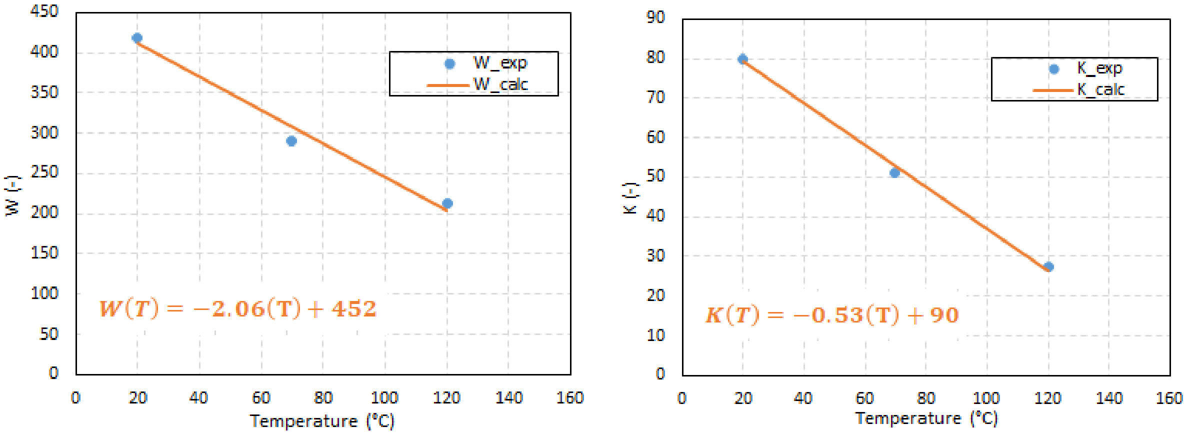

(a) Temperature sensitivity of W (b) Temperature sensitivity of K

Figure 2.18: Temperature sensitivity of W and K represented by the linear variations stated in the figures

and strain rate of the material.

Table 2.11: Temperature dependent model constants of the constitutive law determined from the uniaxial tensile tests

E_1	A_E	σ_{y1}	$A_{\sigma y}$	K_0	A_K	W_0	A_W
12255	915	53.6	1094	134	1223	571.5	778

2.3.2 Accounting for anisotropy

It is demonstrated from the stress-strain curves (Figure 2.6) obtained from the uniaxial tensile tests at 0°, 45° and 90° that the anisotropy of the material cannot be neglected. As suggested by [135]–[140], the equivalent stress can be described by the conventional Hill 48 yield criterion [81] (equation 2.19):

$$\psi\left(\sigma_{ij}\right) = \sqrt{F\left(\sigma_{22}-\sigma_{33}\right)^2 + G\left(\sigma_{33}-\sigma_{11}\right)^2 + H\left(\sigma_{11}-\sigma_{22}\right)^2 + 2(L\sigma_{23}^2 + M\sigma_{13}^2 + N\sigma_{12}^2)} \tag{2.19}$$

In the case of plane stress the equation reduces to:

$$\psi\left(\sigma_{ij}\right) = \sqrt{(G+H)\sigma_{11}{}^2 + (H+F)\sigma_{22}{}^2 - 2H\sigma_{11}\sigma_{22} + 2N\sigma_{12}{}^2} \tag{2.20}$$

With the assumption $G+H=1$, the parameters F, G, H, and N are determined from the yield stress ratio $R(\theta)$ at a given orientation θ with respect to the 0° direction (equation 2.21):

$$R(\theta) = \frac{1}{\sqrt{F\cdot\sin^2\theta + G\cdot\cos^2\theta + H + (2N-F-G-4H)\sin^2\theta\cos^2\theta}} = \frac{\sigma_y(\theta)}{\sigma_y(0^\circ)} \tag{2.21}$$

The yield stress ratios calculated based on the yield stresses identified at three orientations are presented in Table 2.12. Hill's parameters (F, G, H and N) can then be determined from equation that represent the anisotropy of the studied material.

Table 2.12: Yield stress ratios

$\theta(^\circ)$	$\sigma_y(MPa)$	$R(\theta)$
0	29.4	1
45	20.8	0.7
90	16.5	0.56

Table 2.13: Hill parameters

F	G	H	N
2.7	0.53	0.47	2.38

Hill anisotropy is defined in ABAQUS through the plastic potentials calculated as follows:

$$R_{11} = \sqrt{\frac{1}{G+H}}, R_{22} = \sqrt{\frac{1}{F+H}}, R_{33} = \sqrt{\frac{1}{G+F}}, R_{12} = \sqrt{\frac{3}{2N}}, R_{13} = R_{23} = 1 \qquad (2.22)$$

2.4 Numerical validation of the model

By applying the same uniaxial experimental conditions (homogeneous temperature and velocity), the calibrated model is numerically validated by performing finite element simulations of the uniaxial tensile tests on the commercial FE software ABAQUS. The model is implemented by FORTRAN code as a user subroutine UHARD. Only the gauge region of the specimen is modeled. Due to the homogeneous strain field, the model is not sensitive to the element size, number and type. Figure 2.19 shows the stress-strain variations obtained experimentally for 0° orientation at three different temperatures when compared with the simulation results. As shown in the figures, the experimental and numerical results are in good agreement. The mean relative error between experimental and simulation stress-strain curves is indicated in the figures.

On the other hand, the anisotropy is numerically validated by performing finite element simulation using Hill's yield criterion while integrating the parameters determined in the previous section. The three directions (0°, 45° and 90°) are then numerically simulated and compared to the uniaxial experimental results, in Figure 2.20. It shows that Hill's anisotropic criterion associated to the identified numerical model agrees well with the uniaxial experimental results.

For the remaining conditions of temperature and strain rate, the anisotropy criterion is assumed to be the same.

2.5 Conclusion

In this chapter, the mechanical behavior of glass fiber reinforced polypropylene is investigated focusing on the combined effect strain rate/temperature on the material's response. A series of uniaxial tensile tests are performed at room temperature up to 120°C, for strain rates ranging from quasi-static conditions to 10 s^{-1}.

As suspected, tensile properties are sensitive to temperature and strain rate. A temperature increase causes a decrease in Young's modulus, yield strength and ultimate tensile strength but increases the strain at failure. Whereas, the increase in the strain rate rises

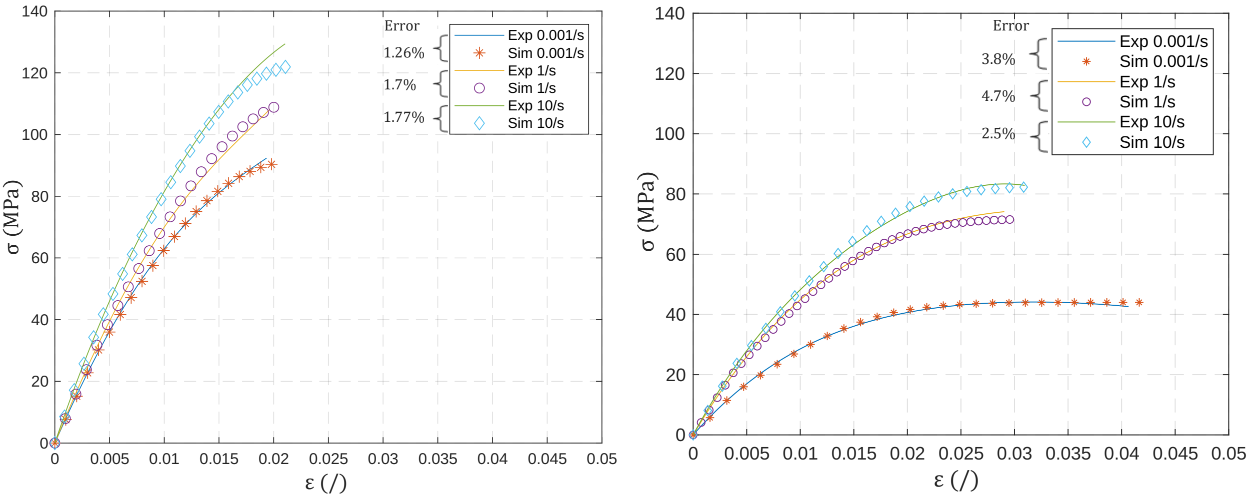

(a) RT (T = 20°C)

(b) T = 70°C

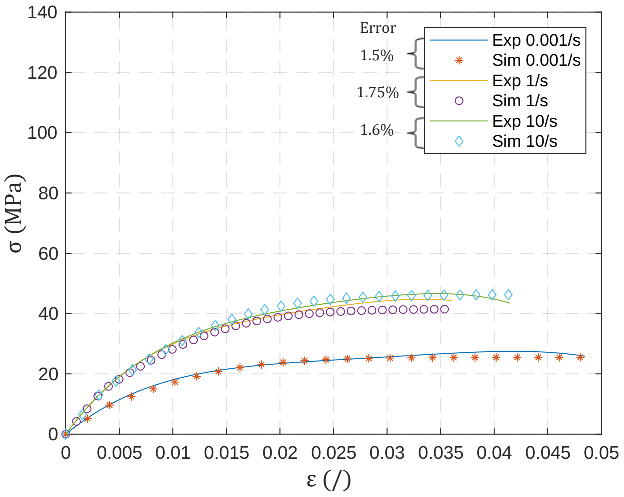

(c) T = 120°C

Figure 2.19: Comparison between experimental and numerical simulation of stress-strain curves

Young's modulus, yield strength and ultimate tensile strength without showing a clear effect on the strain at failure. Also, at higher temperatures, the effect of strain rate becomes less important.

The phenomenological constitutive behavior law inspired by the G'Sell and Jonas model is identified as potentially well-suited to faithfully reproduce the behavior of glass fiber reinforced polypropylene. The original equation is adapted to account for the effects of temperature and strain rate in the ranges concerned in this study. The five model parameters are then calibrated from the full experimental database. Moreover, in order to

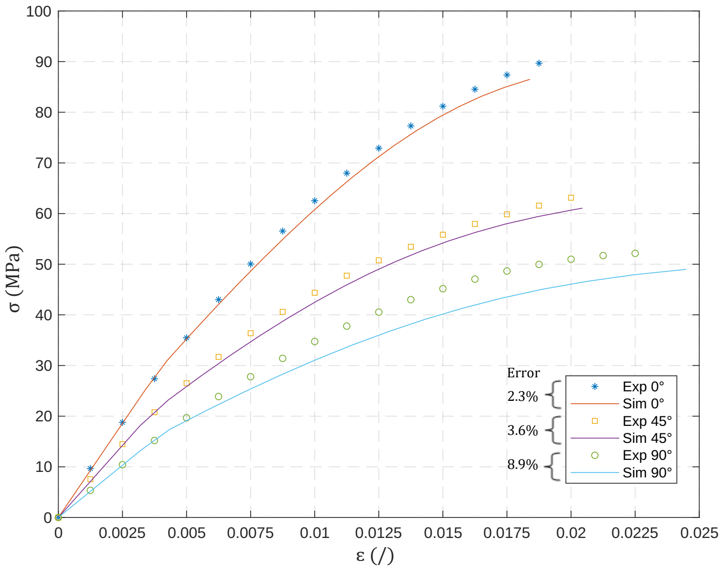

Figure 2.20: Comparison between experimental and simulation results for the three orientations 0°, 45° and 90° taking into account the anisotropy of the material

take into account the anisotropy, the effect of the material's orientation is examined by performing uniaxial tests at 0°, 45° and 90° with respect to the length of the plate. The influence of the orientation is detectable on the stress-strain variations and the tensile properties. Consequently, the experimental results are used to calibrate the parameters of Hill's criterion. The model is then implemented in Abaqus to numerically simulate the uniaxial tensile tests. Good agreement is shown between experimental and numerical stress-strain results.

In Chapter 3, the thermo-mechanical behavior of the material will be characterized using the non-conventional technique of in-plane biaxial tensile tests with a dedicated cruciform specimen. The applicability of the identified model in the simulation of the biaxial test will be inspected.

Chapter 3

In-plane biaxial mechanical characterization

3.1 Introduction

In the previous chapter, a conventional (classic) characterization technique was employed to predict the stress-strain response of discontinuous glass fiber reinforced polypropylene. It relied on straightforward uniaxial tensile tests to calibrate the model parameters. However, a relevant question arises concerning the adequacy of this approach in representing complex strain states (found during forming applications for instance). Therefore, there may be potential advantages in considering a multiaxial characterization of the material's behavior. In-plane biaxial tensile test conducted on cruciform specimens enables testing diverse strain states and allows for the achievement of higher strain levels compared to those obtained through conventional uniaxial testing techniques.

The objective of this chapter is to asses the contribution of an in-plane biaxial tensile test in the thermo-mechanical characterization of a reinforced thermoplastic.
Initially, equi-biaxial tensile tests are conducted on cruciform specimens. Varying loading conditions, involving different temperatures (from RT to 140°C) and strain rates (quasi-static and intermediate) are tested. Then, a finite element model of the biaxial tensile tests is proposed. The modified G'Sell and Jonas model presented in Chapter 2, is re-calibrated based on the experimental results of the in-plane biaxial tensile tests using the Finite Element Model Update (FEMU) approach. Various strategies for parameter optimization are examined, including calibration using databases from both uniaxial and in-plane biaxial tensile tests, as well as calibration exclusively using biaxial test data.

3.2 Experimental biaxial tensile tests

As already discussed in Chapter 1, in-plane biaxial tensile testing on cruciform specimens is becoming more and more common to investigate complex behaviors of materials like metals [115], [116], [141] and even composites [106], [121], [142]. This section presents the cruciform specimen design adopted for the in-plane biaxial characterization. Then, the entire experimental setup and operating conditions are explained. Finally, the main results are presented and discussed.

3.2.1 Cruciform specimen

Generally, the design of the cruciform specimen depends on the intended applications. In the frame of the in-plane biaxial tests, Liu et al. [115] optimized the shape of a cruciform specimen to identify the hardening behavior of metallic sheets subjected to different load conditions. This particular cruciform shape accommodated high levels of equivalent strain within the central region and created a relative homogeneity of strain fields.

In this work, the heterogeneous material under investigation is anticipated to undergo relatively moderate levels of deformation. The achievement of a relatively uniform strain distribution and the attenuation of unfavourable localization effects is mandatory. Also, reaching higher levels of equivalent strains is beneficial in this study as it highlights the distinct contrast between in-plane biaxial characterization and the conventional uniaxial tensile testing technique.

Relying on the aforementioned factors, the cruciform specimen proposed by Liu et al. [115] is considered in this study. The design and dimensions of the specimen are presented in Figure 3.1. The samples are extracted by water-jet cutting from the same plates used for the uniaxial tests. Figure 3.2 illustrates the position of the extracted cruciform specimens relative to the injection port. From a 2mm initial thickness, a thinning of the central zone is achieved by milling (up to a final thickness of 0.625 mm) to ensure failure in this zone. The x-axis corresponds to the length of the plate.

3.2.2 Experimental setup

A specialized quasi-static/dynamic biaxial tensile device developed by Zidane et al.[111] is used in this work to perform the in-plane biaxial tensile tests on a dedicated cruciform specimen. The schematic diagram is shown in Figure 3.3.

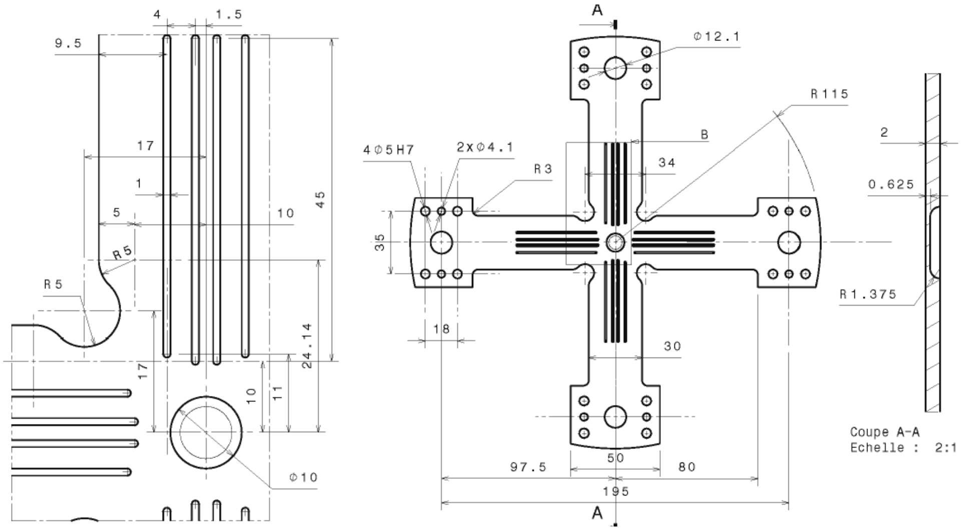

Figure 3.1: Dimensions (in mm) of the cruciform specimen designed by [115]

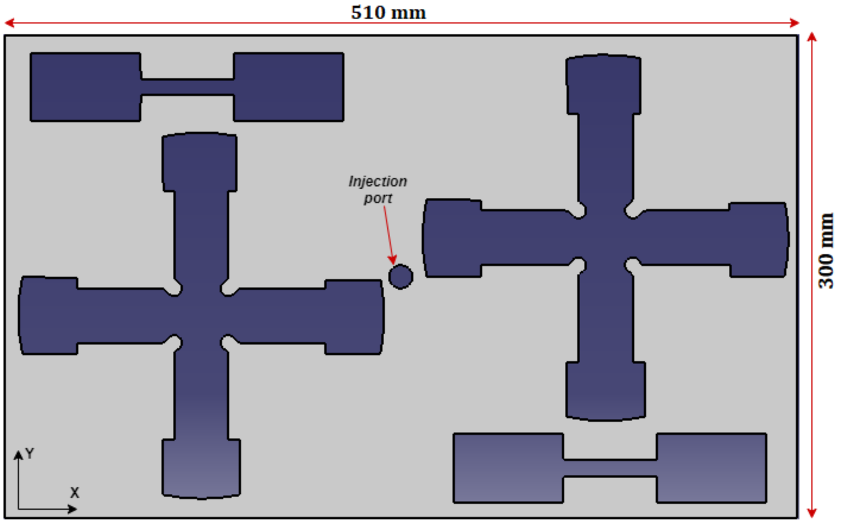

Figure 3.2: Schematic of the plate showing the position of the specimen and an actual image of the specimen extracted from 40%GF/PP plate

This device has been used in different studies for applications that include: (i) calibrating yield criteria, (ii) identifying hardening laws at large strains, and (iii) determining forming limit curves of metallic sheets. Liu et al.[115] investigated the characteristics of the forming limit curve (FLC) of sheet metal using this machine. Liang et al.[144] relied on this machine to perform in-plane biaxial testing on metallic alloys and characterize their temperature and strain rate-dependent behavior. Apart from metals, this apparatus was also used for composite materials in the work of Kobeissi et al.[121] to characterize the

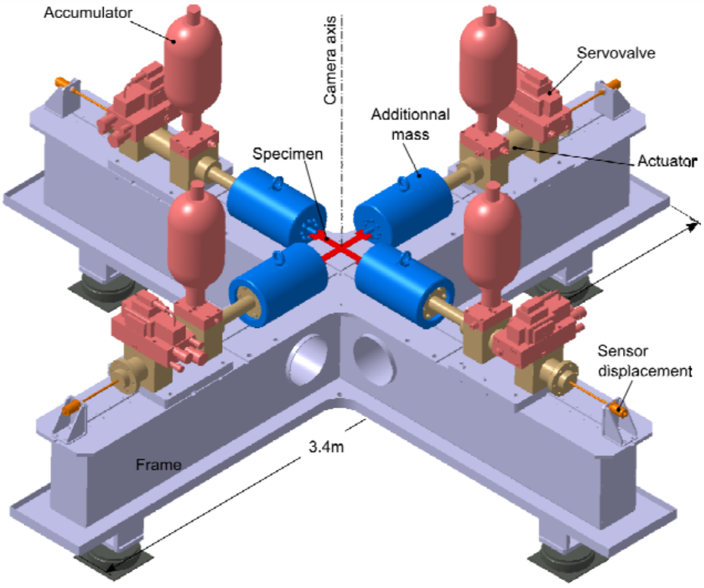

Figure 3.3: Schematic view of the in-plane biaxial tensile testing machine [143]

behavior of glass/epoxy plain weave composite under different biaxial loading ratios.
The apparatus comprises two orthogonal axes in a horizontal configuration. It is equipped with four independent hydraulic cylinders and four accumulators, with two of each per axis. Each axis has a maximum load capacity of 50KN, and each cylinder can achieve a maximum tensile speed of 2m/s, enabling both quasi-static and dynamic testing. By applying varying tensile velocities in different directions, various strain paths can be imposed at the central zone of the cruciform specimen.
For tests conducted at elevated temperatures, a heating system is added to the apparatus. It comprises an airflow generator and an insulated box. The entire setup (machine + heating system) is presented in Figure 3.4. Hot air is generated and directed into the insulated box via an inlet pipe, subsequently circulating back to the airflow generator through an outlet pipe. To maintain a specified set-point temperature, a remote probe located inside the insulating chamber measures and regulates the temperature of the hot air provided by the airflow generator. The specimen's temperature is monitored using thermocouples positioned inside the insulated box. The allowable temperature range for the airflow generator varies from -75°C to 200°C. A close up into the insulated box shows the grip/clamping system to secure the specimen. Two load sensors, which connect the grip system and the sliding bar are placed to measure the forces along both perpendicular directions.

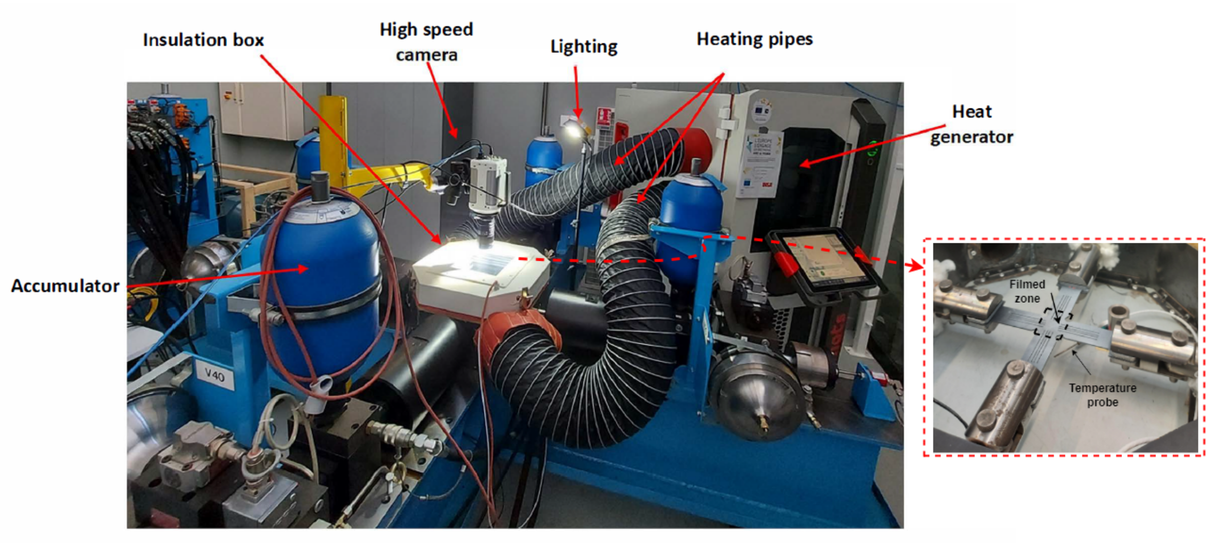

Figure 3.4: Biaxial tensile testing machine

The in-plane strain fields are measured using the Digital Image Correlation technique. A random black and white speckle pattern is created on the flat side of the specimen (Figure 3.5). Here, it's important to note that the image recording is centered on the specimen's flat surface, rather than the opposite face with the reduced thickness, which would require the use of a second camera (to film the curved thickness transition zone). As shown in the setup, only one camera is utilized, which accounts for the filming of the specimen's flat surface that aligns perpendicularly to the camera's axis. Also, the filmed flat area has a better surface finish compared to the machined area, making the DIC analysis more efficient. Therefore, for better visualization, the circular thickness-reduced zone is represented as illustrated in Figure 3.5, highlighting the inner and outer circles of the central zone. The inner circle of 7.25mm diameter corresponds to the inner constant thickness region. The 10mm diameter circle includes the thickness-transition zone.

A high-speed camera (PHOTRON FASTCAM NOVA S9) is positioned along the central vertical axis of the biaxial bench to capture sequential images of the specimen while it undergoes the in-plane tensile testing. For tests at elevated temperatures, the images are filmed through the glass pane located on the top of the insulated box. The specimen is illuminated from the exterior through the glass window. The lighting is adjusted towards the central region of the specimen, in a manner to obtain good image resolution despite the presence of the glass pane. The DIC parameters applied in GOM Correlate are presented in Table 3.1.

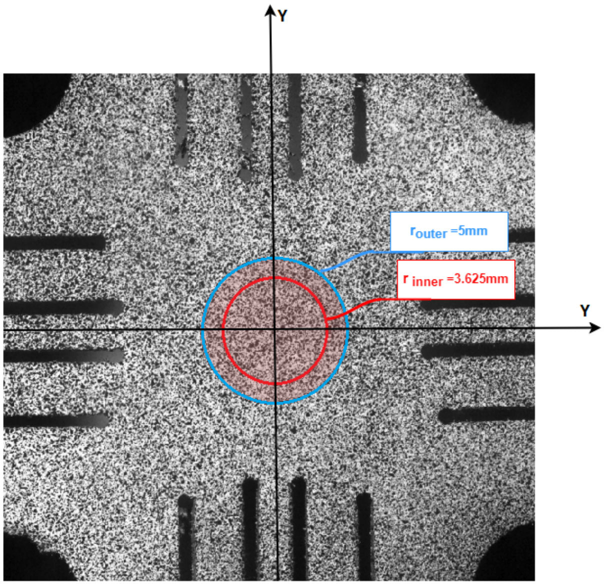

Figure 3.5: Speckle pattern and central zone positioning.

Table 3.1: DIC parameters

Resolution ($pixel \times pixel$)	Facet size ($pixel \times pixel$)	point distance ($pixel$)	magnification factor ($mm/pixel$)
528	21	7	0.06

In order to standardize the selected region of interest for all tests, the equivalent strain $\bar{\varepsilon}$ is averaged on three different regions: the total central circular zone of 10mm diameter, the inner constant thickness zone of 7.25mm in diameter and a zone of 15mm diameter, outside the thickness-reduced area. Note that $\bar{\varepsilon}$ is calculated in GOM Correlate as stated in equation 3.1,

$$\bar{\varepsilon} = \frac{1}{3}\left(\sqrt{2\left[(\varepsilon_1-\varepsilon_2)^2+(\varepsilon_2-\varepsilon_3)^2+(\varepsilon_3-\varepsilon_1)^2\right]}\right) \tag{3.1}$$

With ε_1 and ε_2 being the major and minor in-plane principal strains, respectively. ε_3 represents the principal strain along the thickness direction. This parameter is calculated by GOM Correlate based on the volume constancy.

The variations of $\bar{\varepsilon}$ with respect to time is presented in Figure 3.6 . It is evident that higher deformation levels are achieved in the thickness-reduced central zone. The maximum average equivalent deformation prior to rupture is 2.2% in the 15mm diameter zone. A higher value is attained in the central zone with the thickness reduction. Between the inner and outer circles, the difference is not of significant importance, but the maximum value of $\bar{\varepsilon}$ in the inner circle (3.2%) is slightly higher than the one reached in the outer circle (3%). For the remaining tests, the circular zone with the constant thickness, i.e. inner circle of 7.25mm diameter, will be adopted as the region of interest for calculating the average in-plane strains.

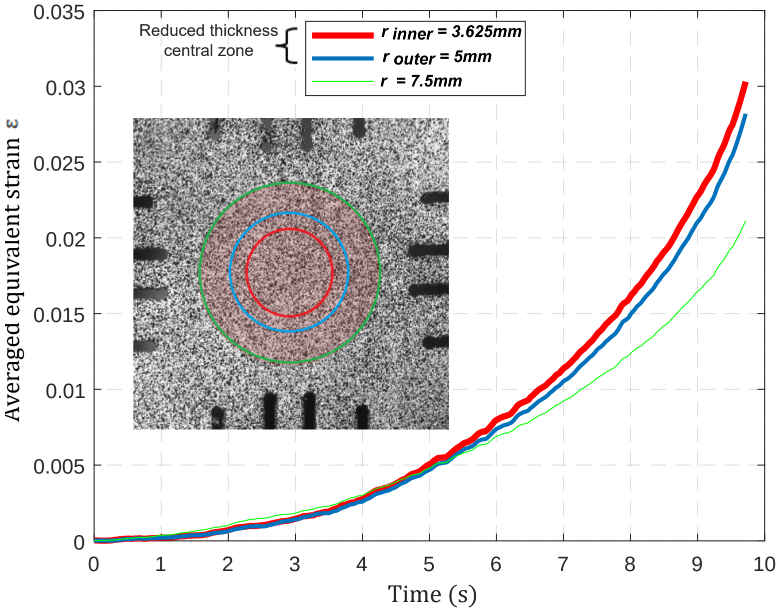

Figure 3.6: Averaging the equivalent strain in the central circular zones of the specimen (test conducted at quasi-static velocity and RT)

Details of the experimental conditions are provided in Table 3.2. Initially, in-plane biaxial tensile tests are performed at tensile velocities of 0.1mm/s and 10mm/s on all 4 arms of the specimens. Each velocity is tested at same temperatures as those tested for uniaxial characterizations i.e. RT (20°C), 70°C and 120°C.

Seeking a quasi-static strain rate, comparable to the strain rate tested in the uniaxial tests (initial strain rate of $0.001s^{-1}$), a loading velocity of 0.1mm/s is imposed on both perpendicular arms of the specimen. The experimental value of the equivalent strain rate $\dot{\bar{\varepsilon}}$ is calculated as follows:

$$\dot{\bar{\varepsilon}}(t) = \frac{\bar{\varepsilon}\left(t_{i+m}\right) - \bar{\varepsilon}\left(t_i\right)}{t_{i+m} - t_i}, \text{ when } t = \frac{t_i + t_{i+m}}{2} \tag{3.2}$$

Where m is the time interval.

For a test conducted at RT and a velocity of 0.1mm/s, the $\dot{\bar{\varepsilon}}$ calculated in the central

Table 3.2: Experimental conditions of biaxial tensile tests

Conditions		**Camera**		**Applied Load**
Velocity (mm/s)	**Temperature** (°C)	**Acquisition** (Hz)	**Resolution** ($pixel \times pixel$)	**Load sensor** (Hz)
0.1	RT	60	640 x 640	60
	70	60	640 x 640	60
	120	60	640 x 640	60
10	RT	3000	640 x 640	3000
	70	3000	640 x 640	3000
	120	3000	640 x 640	3000

zone (inner radius) show a monotonic increase throughout the test while remaining in the quasi-static strain rate range, as shown in Figure 3.7. Therefore, the deformation results

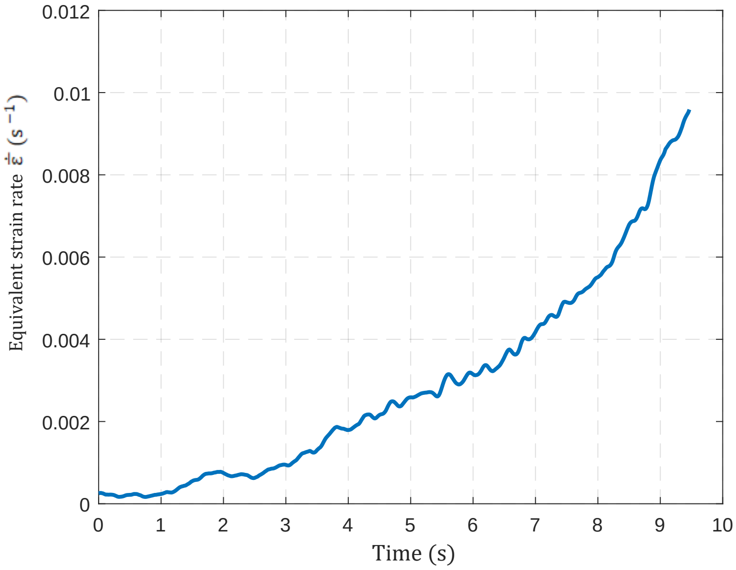

Figure 3.7: Average equivalent strain rate evolution at central zone of quasi-static test at RT

obtained from this loading velocity can be evaluated in comparison to the results of the quasi-static uniaxial tensile tests. At the same loading velocity, two additional tests are conducted at 70°C and 120°C. Likewise, the velocity of 10mm/s induced an equivalent strain rate evolution with a range comparable to the strain rate tested during uniaxial tensile tests (an initial value of 1 s^{-1}).

3.2.3 Experimental results

The temporal evolution of the load (F_X and F_Y along length 0° and width 90° directions of the plate, respectively) as well as ε_1, ε_2 and $\bar{\varepsilon}$, resulting from the in-plane biaxial tensile tests are discussed.

3.2.3.1 In-plane biaxial tensile test at V=0.1mm/s and RT

Figure 3.8a shows the force and strain curves resulting from the in-plane biaxial tensile test at RT and quasi-static velocity of 0.1mm/s. As shown in the figure, maximum forces of $F_X = 1400$ N and $F_Y = 1100$ N are obtained at failure. The difference between both curves can be attributed with the potential material anisotropy. The influence is also visible on the curves showing the temporal evolution of ε_1 and ε_2. The maximum level of strain reached just before failure is ε_{f1}= 1% and ε_{f2}= 2%, respectively (the subscript f designates the value at failure). $\bar{\varepsilon}$ is found to have a maximum value of $\bar{\varepsilon}_f$=3.2% at failure. This level is relatively higher than the strain at failure obtained with the uniaxial tensile test equivalent to 2%, for similar conditions of temperature and strain rate. As predicted, fracture occurs in the central zone of the specimen, as shown in Figure 3.8b. This is the case for all tested conditions.

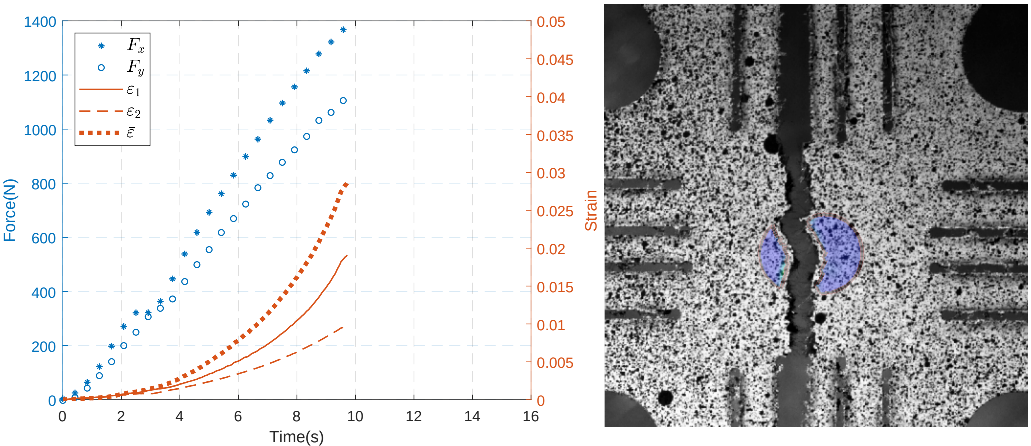

(a) Force and average strains

(b) Rupture in central zone at t= 9.71s

Figure 3.8: In-plane biaxial tensile test at RT and V=0.1mm/s

The repeatability of the tests is ensured by repeating each test at a given condition two or three times. For instance, the test conducted at RT and quasi-static velocity is repeated three times. The measured forces along the longitudinal and transverse direction are shown in Figures 3.9a and 3.9b, respectively. The force evolution with time is clearly consistent for these three identical tests.

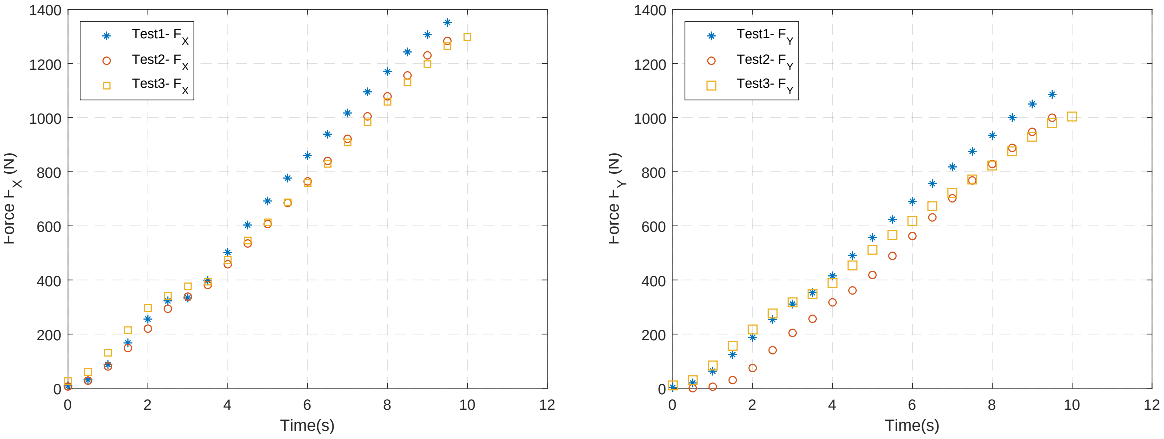

(a) Repeatability tests of F_X

(b) Repeatability tests of F_Y

Figure 3.9: Repeatability of in-plane biaxial tensile test at RT and quasi-static velocity

3.2.3.2 In-plane biaxial tensile test at V=0.1mm/s for T=70°C and T=120°C

The quasi-static tests at higher temperatures of 70°C and 120°C are presented in Figures 3.10a and 3.10b, respectively. The force curves show that the maximum value attained before rupture decrease significantly with the temperature increase, whereas, the value of $\bar{\varepsilon}_f$ increases with higher temperatures to reach 15.8% at T=120°C (approximately five times its value at RT).

3.2.3.3 In-plane biaxial tensile test at V=10mm/s for RT, T=70°C and T=120°C

In order to investigate the combined effect of temperature with a higher strain rate on the biaxial forces and strains, tests are also performed at a higher loading velocity of 10mm/s (intermediate strain rate of approximately $1s^{-1}$). Figure 3.11 shows the temporal evolution of F_X, F_Y, ε_1, ε_2 and $\bar{\varepsilon}$ at RT, 70 and 120°C.

Table 3.3 summarizes the maximum values (at failure) of forces and strains obtained for the in-plane biaxial tensile tests at 0.1mm/s and 10mm/s, at RT, 70 and 120°C. It is

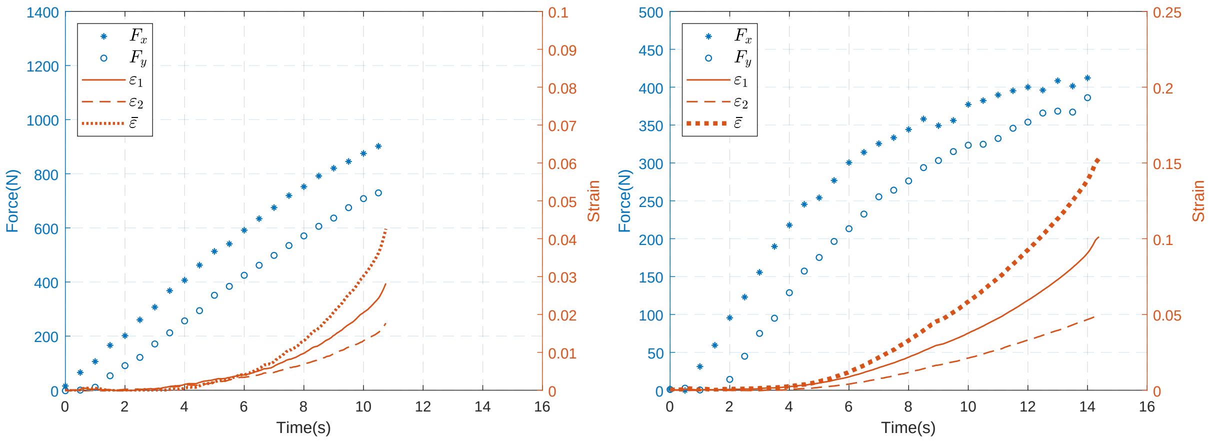

(a) T=70°C and V=0.1mm/s (b) T=120°C and V=0.1mm/s

Figure 3.10: Experimental load and deformation curves at a loading velocity of 0.1mm/s for RT, 70°C and 120°C

obvious that for each temperature, the increase in the loading rate, from quasi-static to intermediate, causes an increase in the force but leads to a decrease in the strain level.

Table 3.3: Force and deformation values at different temperatures and loading rates

T $(°C)$	Velocity (mm/s)	F_{Xf} (N)	F_{Yf} (N)	ε_{1f} (%)	ε_{2f} (%)	$\bar{\varepsilon}_f$ (%)
20	0.1	1400	1100	2	1	3.1
	10	1750	1370	1.3	0.9	2.1
70	0.1	913	747	2.98	1.94	4.6
	10	1119	753	1.87	1.26	2.67
120	0.1	410	380	10.46	4.85	15.8
	10	555	435	5.7	1.65	7.5

As an attempt to have an approximate comparison between the uniaxial and in-plane biaxial tensile tests, the values of $\bar{\varepsilon}_f$ at both quasi-static and intermediate loading rates are compared in Table 3.4. Considering quasi-static loading, the strain levels reached during uniaxial tensile tests at RT, 70°C and 120°C are lower than the values obtained when an equi-biaxial solicitation is applied at the same temperatures. Particularly, at high temperatures such as 120°C, $\bar{\varepsilon}_f$ for the equi-biaxial condition (15.8%) is approximately three times higher than the maximum value of strain attained for uniaxial conditions (4.8%). For intermediate loading rates, the increase in $\bar{\varepsilon}_f$ is not important, even at 120°C, where a maximum value of 7.5% is reached.

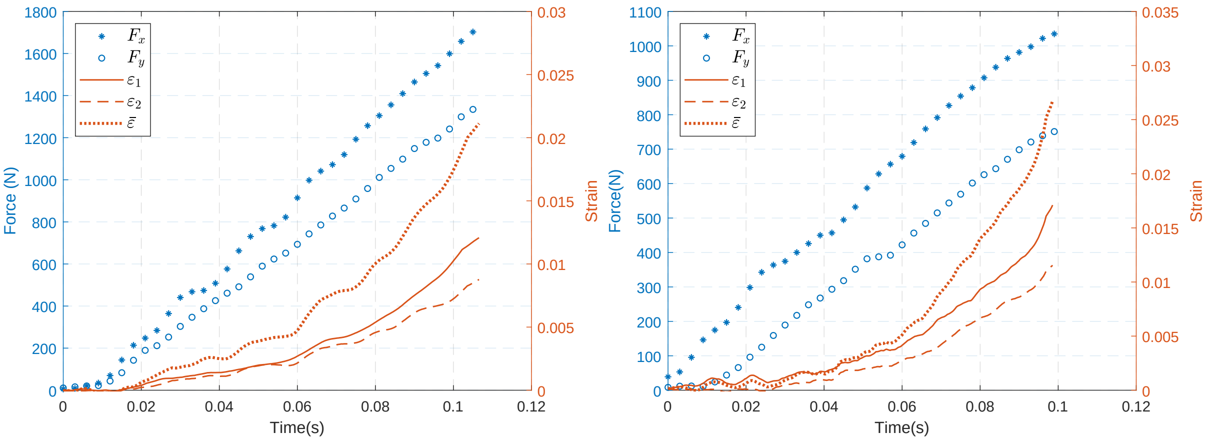

(a) RT and V=10mm/s (b) T=70°C and V=10mm/s

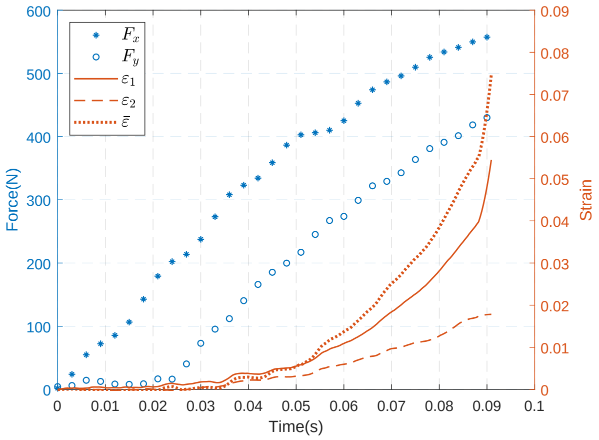

(c) T=120°C and V=10mm/s

Figure 3.11: Experimental load and deformation curves at a loading velocity of 10mm/s for RT, 70°C and 120°C

From Table 3.3 and Table 3.4, two conclusions can be stated: In-plane biaxial tests induce equivalent strains higher than the those generated by uniaxial tensile tests, specially at elevated temperatures. Also, for the case of the in-plane biaxial tests, equivalent strain levels obtained with a load velocity of 10mm/s are not high relative to those obtained at quasi-static speed. In other words, the formability of the material will be better at the highest possible temperatures and at a quasi-static strain rate.

Table 3.4: Comparison between uniaxial and in-plane equi-biaxial tensile tests

Operating condition		**Uniaxial test**		**Biaxial tests**	
Strain rate state	T (°C)	V (mm/s)	$\bar{\varepsilon}_f$ (%)	V (mm/s)	$\bar{\varepsilon}_f$ (%)
Quasi-static	RT	0.05	1.94	0.1	3.1
	70		4		4.6
	120		4.8		15.8
Intermediate	RT	50	1.96	10	2.1
	70		2.9		2.8
	120		3.6		7.5

3.2.3.4 In-plane biaxial tensile test at V=0.1mm/s and a higher temperature range

According to the latest conclusion, and for a better understanding of the temperature influence on the in-plane biaxial behavior of the material, additional tests are carried out at a quasi-static speed of 0.1mm/s and elevated temperatures (higher than 120 °C) of 130, 135 and 140°C. A test at 100°C is also performed in order to obtain a clearer vision of the temperature effect. The evolution of forces and deformations at the mentioned conditions are shown in Figure 3.12. It can be noted that the higher the temperature, the lower the force. Contrary to the deformation which increases with temperatures. The effect is clearly pronounced at the highest temperatures. Even a 5°C gap causes a significant increase in the maximum deformation level, i.e. $\bar{\varepsilon}_f$ increases by 50% when the temperature increases from 135 to 140 °C.

To illustrate the influence of temperature on the biaxial force and equivalent deformation, an average value of F_{Xf} and F_{Yf} is considered, denoted as F_{max}. The temperature sensitivity is also investigated for $\bar{\varepsilon}_f$. Figure 3.13 shows the evolution of these parameters with respect to temperature ranging from RT to 140°C, at the quasi-static speed. As illustrated in the figure, the behavior is tested in a range excluding the glass transition and melting regions of glass fiber reinforced polypropylene (According to ([26], [133], [134]) the glass transition region of glass fiber reinforced polypropylene is between -25 to 10°C, and the melting temperature according to ([145], [146]) is above 160°C). The evolution of $\bar{\varepsilon}_f$ is similar to an exponential trend, where in the restricted temperature range, from 120°C and above, a sharp increase in the level of deformation becomes remarkable, reaching 33% at 140°C. On the other hand, F_{max} decreases in approximately a linear trend, down to a value of around 200N. The values are also summarized in Table 3.5.

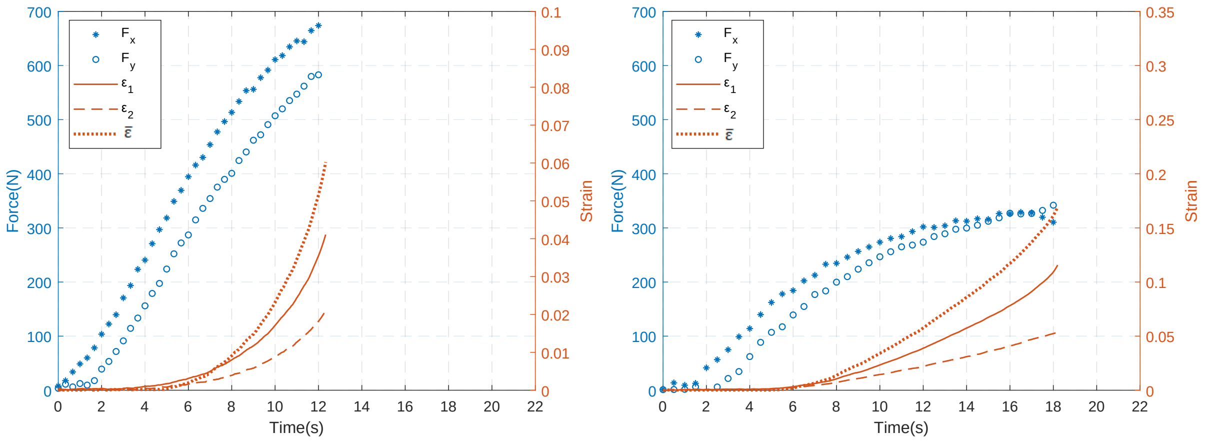

(a) T=100°C and V=0.1mm/s

(b) T=130°C and V=0.1mm/s

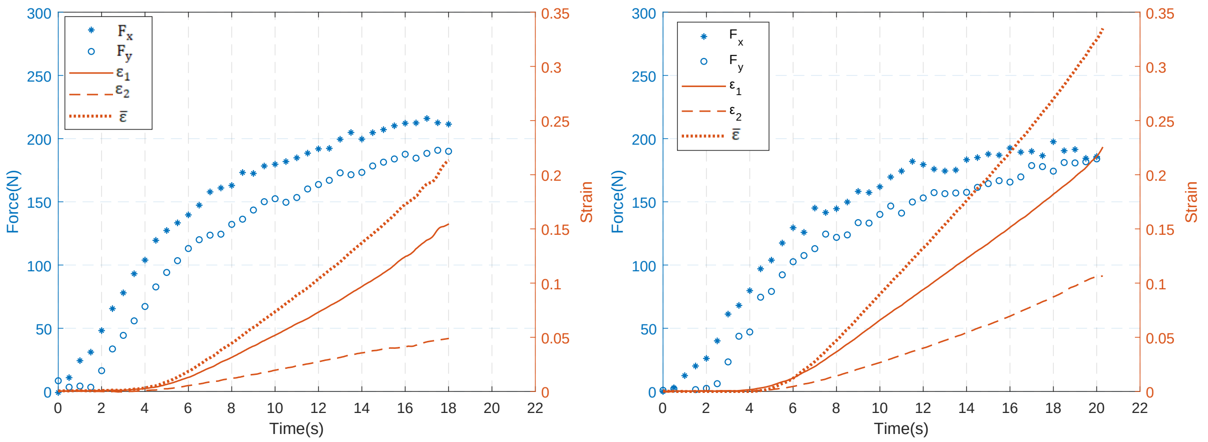

(c) T=135°C and V=0.1mm/s

(d) T=140°C and V=0.1mm/s

Figure 3.12: Experimental loads and deformation curves at temperatures ranging from 100 to 140°C

Table 3.5: Temperature sensitivity of maximum biaxial force and equivalent deformation

$T(°C)$	RT	70	100	120	130	135	140
$\bar{\varepsilon}_f(/)$	3.1	4.58	5.6	15.6	17	22	33
$F_{max}(N)$	1140	833	654	364	314	200	185

3.2.3.5 Experimental in-plane strain fields

The principal strain fields are evaluated in GOM Correlate. In the case of the quasi-static test at a T= 135°C, the images captured just before the material ruptures correspond to a

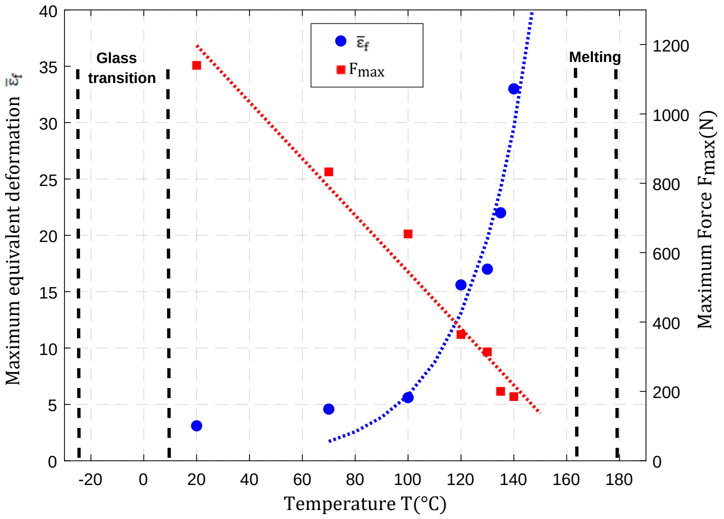

Figure 3.13: Temperature effect on the maximum load and equivalent strain

total time of 18 seconds. Figures 3.14, shows the entire filmed area of the specimen. To get a clear vision of the strain field distribution within the gauge area, a bigger calculation zone of 17 mm diameter is considered for measuring the equivalent strain field. The thickness-reduced central zone is represented by the red and blue circles for the inner and outer radii, respectively. At 7s before failure, a concentrated strain field is observed within the inner circular zone. Figure 3.15 shows a clearer illustration of the equivalent strain field of $\bar{\varepsilon}$ at three different instants before failure: t = 11s, t= 14s and t= 17s. At 1s just before failure (t=17s), the equivalent strain reaches a maximum value of approximately 25% within the inner circular zone.

For the quasi-static test at a T= 120°C, the recorded images correspond to a total time of t= 14.5s. Similarly, a 17mm diameter zone is defined for the calculation of strain fields, as illustrated in Figure 3.16. Likewise, the equivalent strain field begins to concentrate within the inner circular zone a while before reaching failure. The strain fields of $\bar{\varepsilon}$ at three instants before rupture (t= 11.5s, t=12.5s and t=13.5s) are presented in Figure 3.17. At 1s before failure occurs (t=13.5s), $\bar{\varepsilon}$ reaches a maximum value of 14% in the inner circular zone.

For both conditions, as well as for all the others, failure occurs exactly in thickness-reduced central zone of the specimen with concentrated and nearly homogeneous strain distribution. It can be concluded that the selected cruciform design, originally designed for metals, can relatively be suitable for heterogeneous materials such as fiber reinforced thermoplastics.

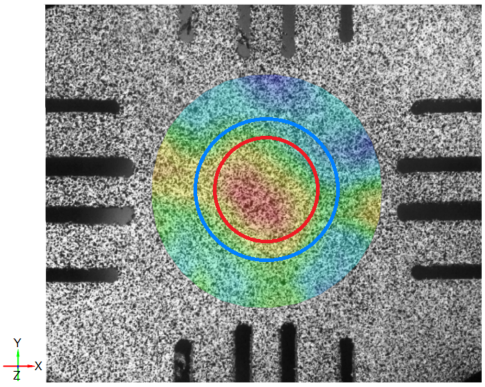

Figure 3.14: Equivalent strain fields at 0.1mm/s and T=135°C 7s before failure

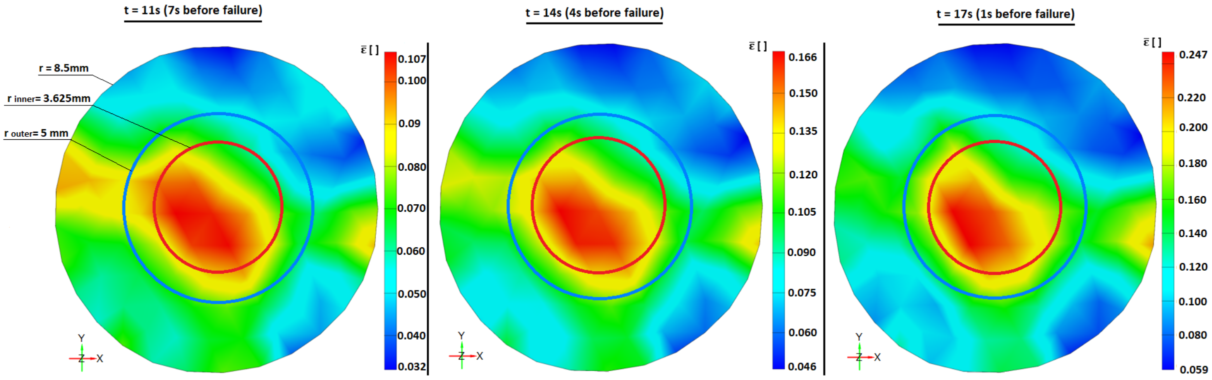

Figure 3.15: Equivalent strain fields at 0.1mm/s and T=135°C at three instants before failure

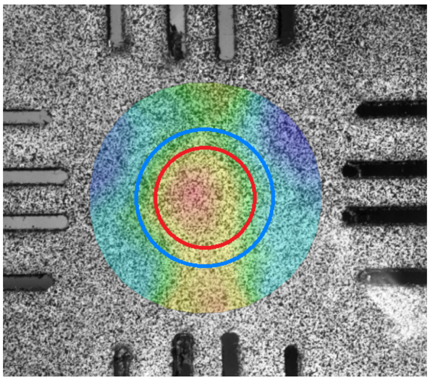

Figure 3.16: Equivalent strain fields at 0.1mm/s and T=120°C 3s before failure

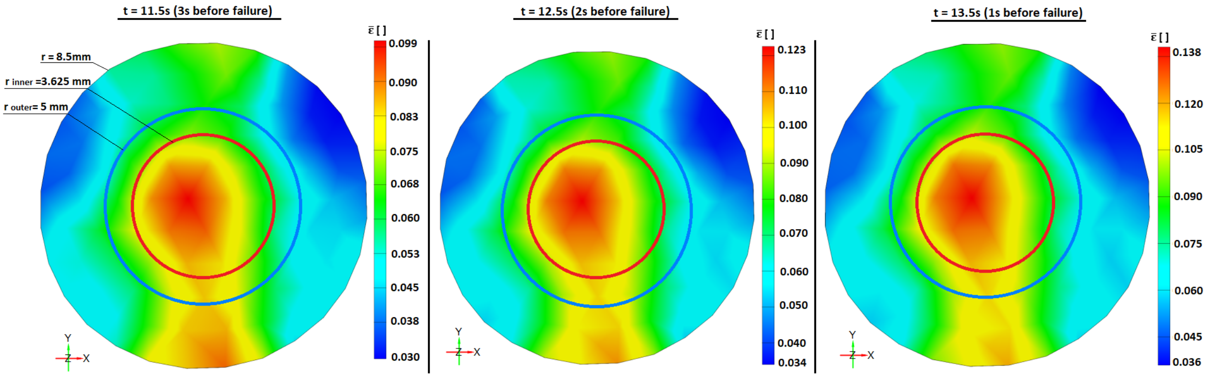

Figure 3.17: Equivalent strain fields at 0.1mm/s and T=120°C at three instants before failure

3.3 Numerical approach

This section concerns the numerical modeling of the in-plane biaxial tensile tests. First, a FE model of the test is proposed using the specimen defined in Figure 3.1. Then, based on this model and the G'Sell and Jonas law identified in Chapter 2, equivalent strains are predicted and compared to the experimental ones. Due to large discrepancies observed, an inverse analysis approach based on the Finite Element Model Updating (FEMU) is carried out to calibrate the G'Sell and Jonas model parameters from the biaxial tensile database.

3.3.1 FE model of the in-plane biaxial test

The FE model is established in the environment of Abaqus software (implicit solver). For reducing computational times, only one-quarter of the specimen is modeled due to symmetry considerations, as shown in Figure 3.18. The boundary conditions and element mesh have been configured to closely align with the experimental test conditions. The cruciform specimen is meshed with 3D elements and discretized through 8-node brick elements (C3D8R). Since the central zone is the area of primary interest in the in-plane biaxial tensile state, the element size is refined to 0.1 mm and three elements are arranged along the thickness direction. As for the boundary conditions, symmetry is imposed on sides 1 and 2. The temporal evolution of forces $F_X/2$ and $F_Y/2$ obtained experimentally are applied along both perpendicular directions. Half of the experimental force is applied due to symmetry. Applying the forces obtained experimentally as boundary conditions makes it possible to accurately reproduce the experimental conditions.

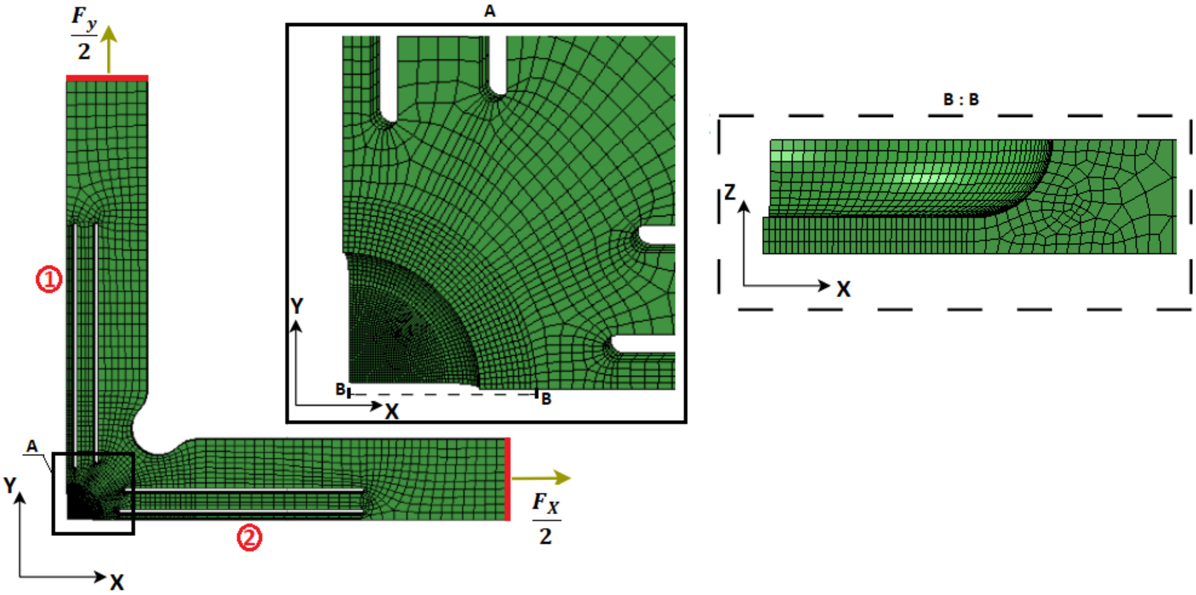

Figure 3.18: FE model of the cruciform specimen used to simulate the in-plane biaxial tensile test

3.3.2 Prediction of in-plane biaxial strain field

The modified G'Sell and Jonas law identified from the uniaxial tensile tests in Chapter 2, is used to simulate the in-plane biaxial tensile test conducted at RT and quasi-static velocity. To check for the reliability of the model equation, the numerical and experimental results are compared. The numerical results involve the temporal evolution of the equivalent strain ($\bar{\varepsilon}^{sim}$) at the central point of the specimen (flat surface), while the experimental data include the temporal evolution of the equivalent strain strain $\bar{\varepsilon}^{exp}$ determined using the DIC technique (the superscripts "*sim*" and "*exp*" are now added the expression of the strains to differentiate the numerical and simulated results).

Note that $\bar{\varepsilon}^{sim}$ is calculated with the same expression previously applied to calculate the experimental values (equation 3.1). Figure 3.19 shows the poor agreement between the experimental and simulated result. $\bar{\varepsilon}_f^{exp}$ (3.1%) is 61% higher than $\bar{\varepsilon}_f^{sim}$ (1.2%). This difference shows that the behavior law identified from the uniaxial tensile tests is not suitable describing the behavior of the material subjected to in-plane biaxial state. This model clearly leads to an overestimation of the material's rigidity when simulating the in-plane biaxial test.

Recognizing the limitations of the previous calibration strategy, a different approach is

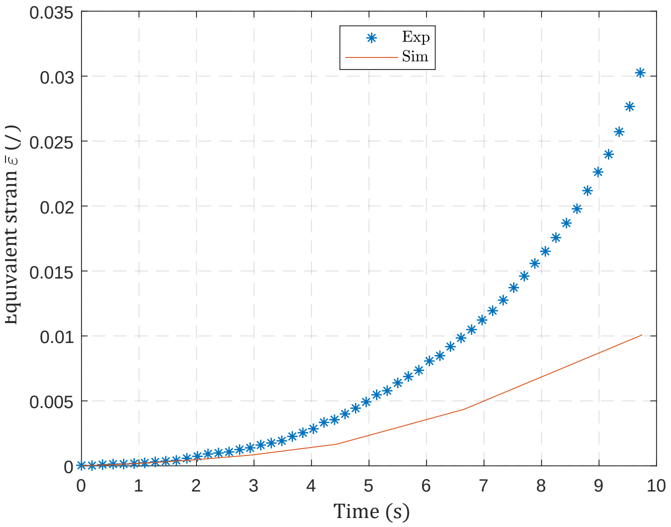

Figure 3.19: Comparison between experimental and simulated equivalent strain at RT and quasi-static loading using the model identified from uniaxial characterization

proposed which consists in calibrating the model parameters through inverse analysis by incorporating the in-plane biaxial test results.

In the following, two possible strategies will be introduced to calibrate the parameters of the behavior law:

The first strategy consists in finding a set of model parameters that can reasonably capture material behavior under both uniaxial and biaxial loading conditions, effectively seeking a compromise between both behaviors. The second strategy focuses on calibrating the model to precisely match the behavior of the material when subjected to biaxial loading conditions. Here, the parameters are adjusted specifically to align with the results of the in-plane biaxial tensile tests.

3.3.3 Re-calibration of the G'Sell and Jonas law using the FEMU method

In the case of the mechanical characterization from uniaxial tensile tests, the stresses and strains can be directly computed. However, when in-plane biaxial tests are concerned, direct calculation of stresses and strains is not possible. Therefore, an inverse analysis procedure is essential for the identification of the parameters.

Among the various approaches available for parameter identification based on full-field measurements, one feasible option is the FEMU. This method involves minimizing the gap between the output of finite element simulations and experimental observations by optimizing the material parameters.

This approach is suggested to identify the parameters of the modified G'Sell and Jonas model defined in Chapter 2 and recalled in this section:

$$\begin{cases} \bar\sigma(\bar\varepsilon,\dot{\bar\varepsilon},T) = E(\dot{\bar\varepsilon},T)\cdot\bar\varepsilon & \text{for } \bar\sigma < \sigma_{\mathrm{y}} \\ \bar\sigma(\bar\varepsilon_p,\dot{\bar\varepsilon},T) = \sigma_{\mathrm{y}}\left(\dot{\bar\varepsilon},T\right) + K(T)\cdot\left(1-\exp\left(-W(T).\bar\varepsilon_p\right)\right)\dot{\bar\varepsilon}^{m(T)} & \text{for } \bar\sigma > \sigma_{\mathrm{y}} \end{cases} \tag{3.3}$$

Figure 3.20 presents a flowchart of FEMU approach. Note that for each condition, the experimental temporal evolution of forces and strains are smoothed before being integrated in the optimization scheme. The multi-disciplinary and multi-objective optimization platform of modeFRONTIER is considered in this work. This software enables the integration

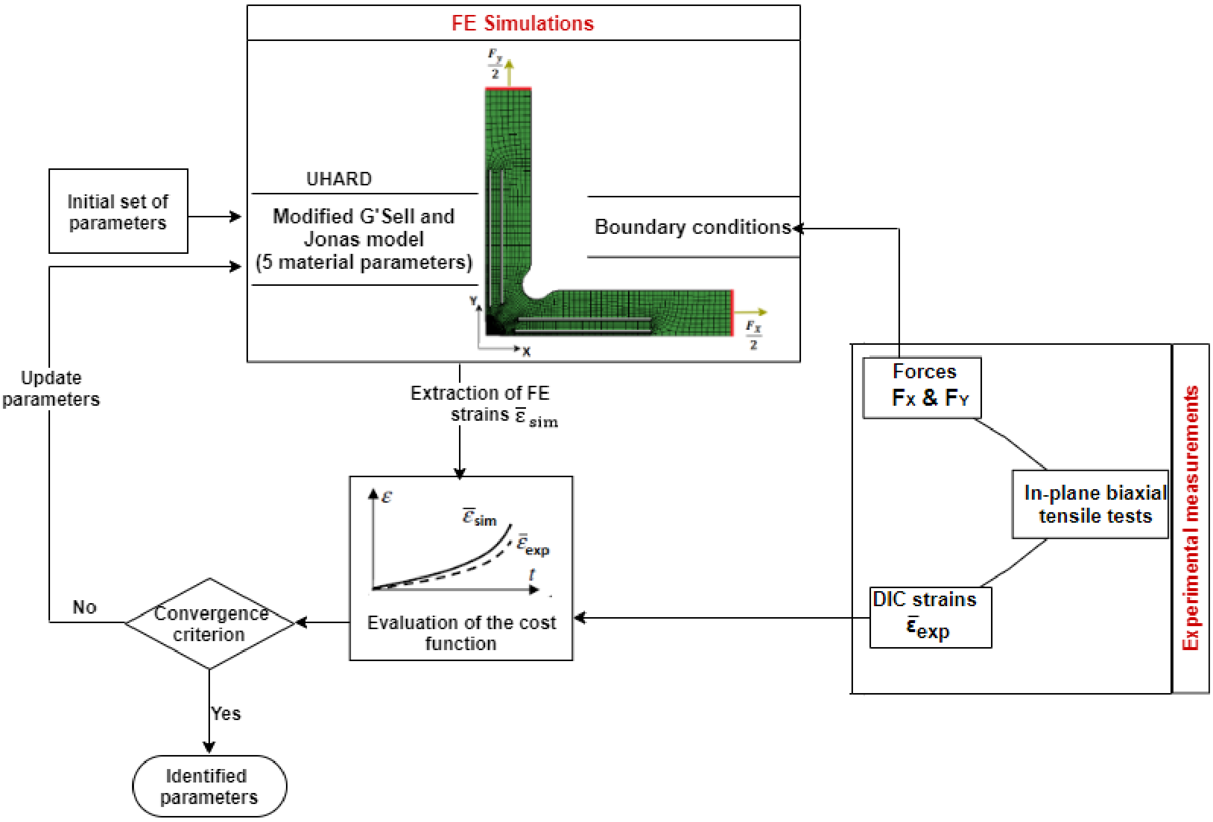

Figure 3.20: Flowchart of FEMU for parameters identification

of FE simulation codes, such as Abaqus, with optimization algorithms. Two of the most commonly used algorithms are applied in this work: MOGA (Multi-objectives Genetic Algorithm) and SIMPLEX. A brief description of each will be given later.

3.3.3.1 Calibration of parameters based on uniaxial and biaxial results

For this strategy, the model parameters will be calibrated based on the biaxial and uniaxial results obtained from the tensile tests conducted at quasi-static loading and temperatures RT, 70 and 120° C. Two cost functions (biaxial and uniaxial) are to be minimized; the first one denoted by f_1 is related to the biaxial results. It minimizes the relative root mean squared error equation (equation 3.4) between the experimental and simulated equivalent strain computed as stated in equation 3.1.

$$f_1 = \sqrt{\frac{\frac{1}{n}\sum_i^n \left(\bar{\varepsilon}^{\text{exp}}(t_i) - \bar{\varepsilon}^{\text{sim}}(t_i)\right)^2}{\sum_i^n \left(\bar{\varepsilon}^{\text{exp}}(t_i)\right)^2}} \tag{3.4}$$

Where n corresponds to time increments during the experiment and simulation. The second cost function f_2 (equation 3.5) consists in minimizing the relative root mean squared error between the experimental ($\bar{\sigma}^{\text{exp}}$) and analytical ($\bar{\sigma}^{\text{num}}$) equivalent uniaxial stress for p calculation points. These cost functions are introduced in a Matlab script that links between the experimental data and the simulation results (updated after each iteration).

$$f_2 = \sqrt{\frac{\frac{1}{p}\sum_i^p \left(\bar{\sigma}^{\text{exp}}(t_i) - \bar{\sigma}^{\text{num}}(t_i)\right)^2}{\sum_i^p \left(\bar{\sigma}^{\text{exp}}(t_i)\right)^2}} \tag{3.5}$$

For this identification strategy, MOGA is chosen as the optimization algorithm. Genetic algorithms are stochastic optimization methods that introduce a certain degree of randomness in the search process to make the latter less sensitive to modeling errors and escape any local optima to eventually converge to a global optimum. The optimization with a genetic algorithm is an iterative process: it starts from a population of randomly generated individuals and, as the search evolves, the subsequent populations include fitter and fitter solutions. Genetic algorithms offer several advantages, including effective global exploration of the design space, applicability across problem dimensions, high robustness, tolerance to noisy objective functions, and suitability for multi-objective robust design optimization. However, it's important to note that they may exhibit a lower convergence rate when high accuracy is required in optimization.

Since two objective functions are to be minimized in the present approach, MOGA comes as a suitable option for this optimization. The concept of Pareto Front can be regarded subsequently.

Out of five parameters, three are considered as the variables: σ_y, K and W. Young's modulus E is assumed to follow the same evolution with respect to temperature that was defined from the uniaxial tensile tests. The strain rate sensitivity m determined from the uniaxial tests at each temperature is presumed to be unchanged for the biaxial behavior. i.e. at each temperature condition, m and E are predefined and the remaining parameters are the variables to be optimised.

The initial values of the variables are those calibrated from the uniaxial tests in Chapter 2. Figure 3.21 shows the optimization workflow to determine the material parameters while including both uniaxial and in-plane biaxial test databases. The parameter sets are optimized for each tested temperature.

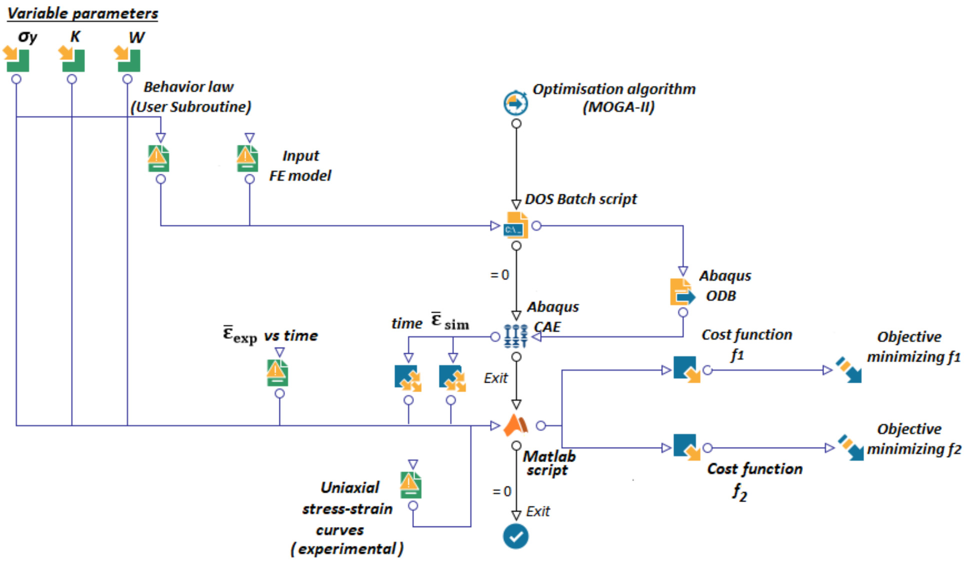

Figure 3.21: Workflow to determine the material parameters from the uniaxial and in-plane biaxial tensile test databases

Pareto Front

In the context of multi-objective optimization, a fundamental concept revolves around Pareto optimality and the associated term of Pareto dominance. Achieving a perfect solution when considering multiple objectives is often an unattainable goal. Instead, the approach is to explore a set of solutions that represent equally favorable compromises. The principle of Pareto front is presented in Figure 3.22. A Pareto optimal set, also

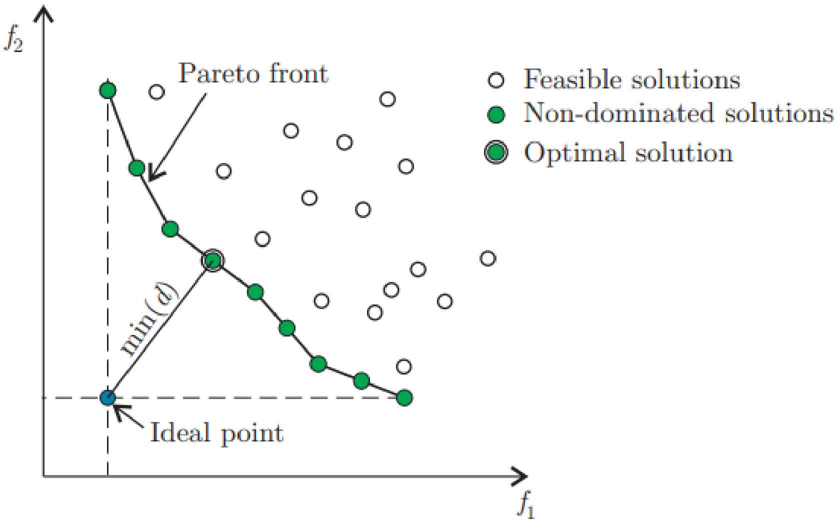

Figure 3.22: Principle of Pareto Front [147]

known as a Pareto front, constitutes a collection of solutions where none dominates the others. In other words, it's impossible to enhance any design objective without negatively affecting another. This implies that as one transitions from one Pareto solution to another, there's always a trade-off involved, where improvements in certain objectives come at the expense of others. From a mathematical perspective, each Pareto optimal point holds equal significance in addressing a multi-objective optimization problem. In practical terms, decision-makers often prefer Pareto optimal solution sets over single solutions, as their choices inherently involve trade-offs based on personal or objective preferences.

In this work, based on both objective functions f_1 and f_2, MOGA gives different sets of parameters i.e. different solutions. Plots showing the evolution of f_1 with respect to f_2 for three temperatures is presented in Figure 3.23. From this, the Pareto Front of the error can be verified showing that no solution can be improved in one objective without sacrificing performance in the other. This helps in identifying the best trade-off solution among these two conflicting objectives. Table 3.6 gives the parameter sets at each temperature for three different behaviors: i) close to biaxial behavior i.e, lower f_1, ii)close to uniaxial behavior i.e., lower f_2, iii) compromise between uniaxial and biaxial i.e., f_1 and f_2 are almost similar (same percent error between experimental and numerical results). The choice of the parameter set can then be selected based on the desired application or type of loading that the material is going to experience.

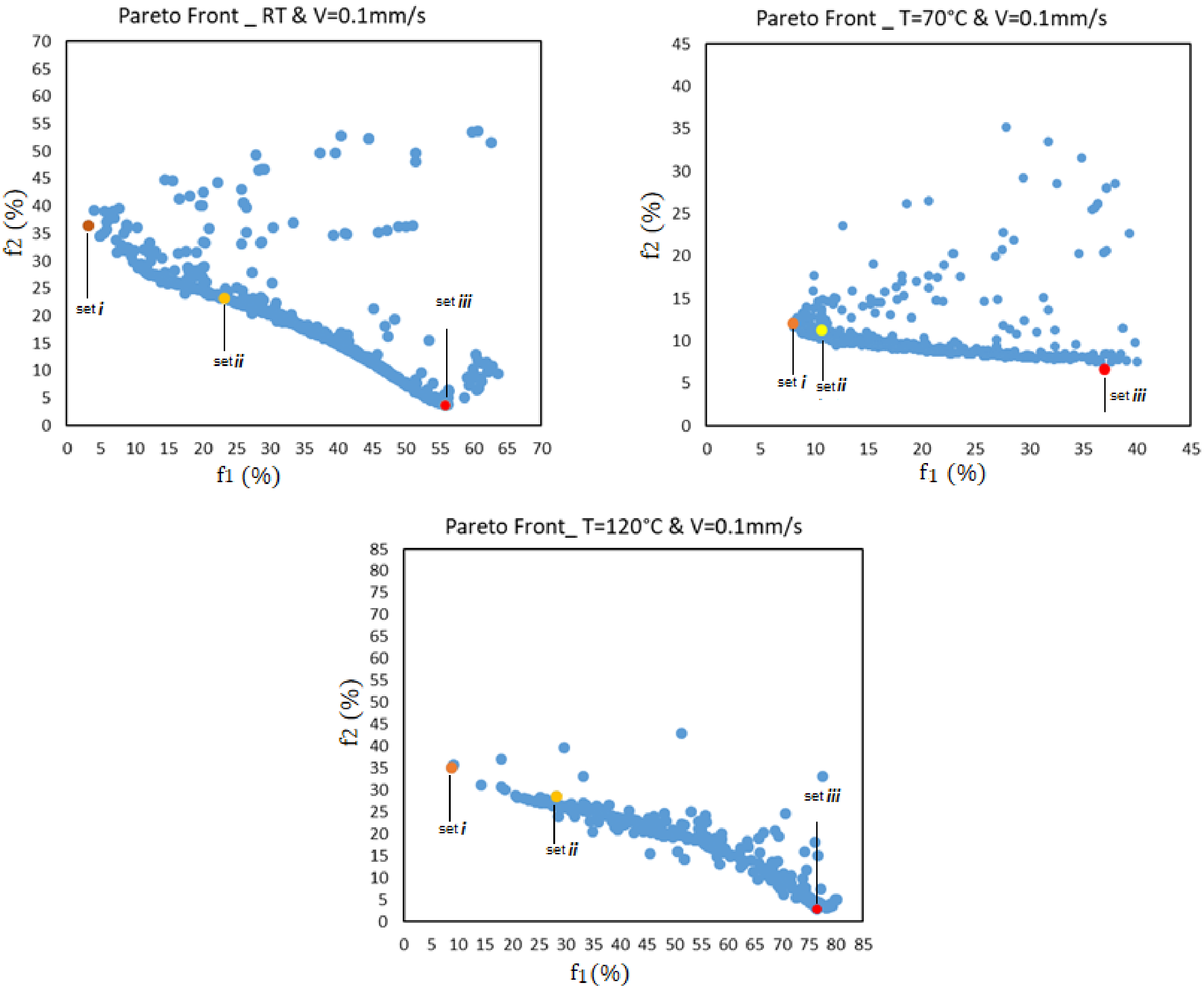

Figure 3.23: Pareto Front showing the uniaxial and biaxial cost functions

In certain scenarios such as forming applications, the type of loading is definitely biaxial in which the material is more likely to encounter a biaxial stress state. Therefore, for a higher calibration accuracy, it can be interesting to calibrate the rheological parameters when considering only the in-plane biaxial test results (excluding the uniaxial tensile test results from the optimization scheme). This is discussed in the next section.

Table 3.6: Parameter sets (defined in Figure 3.23) obtained by inverse analysis along with the percent error of the biaxial results with respect to the error of the uniaxial results

$T(°C)$	Set	$K(MPa)$	$W(/)$	$\sigma_y(MPa)$	f_1	f_2
RT	i	86	173	29	3.2%	36%
	ii	82	104	35	23.3%	23.1%
	iii	88	237	34	55%	3.7%
70	i	34	123	28	8%	12%
	ii	34	97	30	10.7%	11.3%
	iii	27	161	29	37%	6.7%
120	i	30	48	7	8.9%	35%
	ii	29	93	5	28.3%	28.6%
	iii	26	111	13	76%	2.78%

3.3.3.2 Calibration of parameters based on biaxial tests

For this identification, only the temporal evolutions of the experimental equivalent strain obtained from the in-plane biaxial tensile tests (DIC measurements) are used to calibrated the modified G'Sell and Jonas model.

SIMPLEX is applied as the optimization algorithm. It is a valuable tool for solving non-linear single-objective optimization problems. This algorithm uses the concept of a polyhedron comprising N+1 vertices within an N-dimensional space (where N signifies the number of input variables). It operates by systematically assessing the objective function's values at these N+1 vertices and progressively manipulating the polyhedron toward the optimal point. A Simplex run ends when it either reaches the maximum allowable number of evaluations or attains the desired termination accuracy, whichever occurs first. Simplex is sensitive to the lower and upper bound as well as the initial values of the parameters. It is more adapted for shorter parameter ranges. Contrary to MOGA, a faster convergence is achieved with SIMPLEX.

For this calibration strategy, the in-plane biaxial tests at quasi-static velocity of 0.1mm/s and a wider temperature range up to 140 °C are concerned. The optimization loop is illustrated in Figure 3.24. For temperature conditions of 100, 130, 135 and 140°C, Young's modulus is predicted according to equation 2.10, derived in Chapter 2 (the temperature effect on E is assumed to be the same whatever the strain state). Whereas for the strain rate sensitivity m, a value of 0.07 is considered. This assumption is based on the observations of the uniaxial tensile tests which showed that the effect of strain rate is negligible at elevated temperatures. The initial values of the variables K, W and σ_y along with the lower and upper bounds applied in the SIMPLEX algorithm are listed in Table 3.7.

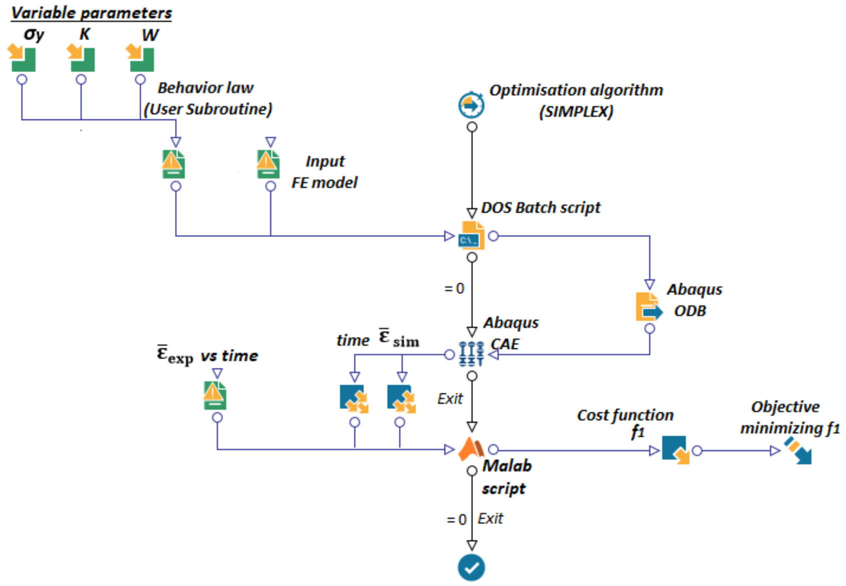

Figure 3.24: Optimization workflow to determine the material parameters from the in-plane biaxial test database

Table 3.7: SIMPLEX initial conditions

T(°C)	Parameter	Initial value	Lower bound	Upper bound
RT	σ_y (Mpa)	30	20	40
	K (Mpa)	80	30	100
	W (/)	130	50	200
70	σ_y (Mpa)	13	10	35
	K (Mpa)	51.3	20	70
	W (/)	290	30	300
100	σ_y (Mpa)	20	10	30
	K (Mpa)	37	30	50
	W (/)	55	50	170
120	σ_y (Mpa)	13	9	20
	K (Mpa)	27.3	15	40
	W (/)	35	40	60
130	σ_y (Mpa)	7	5	15
	K (Mpa)	25	20	30
	W (/)	30	10	55
135	σ_y (Mpa)	7	5	10
	K (Mpa)	25	10	30
	W (/)	30	10	40
140	σ_y (Mpa)	7	5	10
	K (Mpa)	20	10	30
	W (/)	10	3	20

The new optimized parameters of the modified G'Sell and Jonas model are summarized in Table 3.8. The temporal evolution of the simulated principal and equivalent strains for different conditions are compared with the experimental plots, as shown in Figure 3.25.

Table 3.8: Identified parameters based on the experimental equi-biaxial tensile tests

$T(°C)$	$K(Mpa)$	$\sigma_y(Mpa)$	$W(/)$	$f_1(\%)$
20	78.9	25	134.4	5.23
70	36.15	29.3	117.93	7.6
100	30.33	23.87	72.8	6.6
120	24.29	10.4	44.02	2.6
130	22.56	8.93	28.75	6.7
135	19.9	5.61	11.23	5.26
140	17.46	6.03	7.07	2.56

It can be noted that the identified model based on the in-plane biaxial tensile tests gives a well description of the temporal principal strains evolution in the tested temperature range. The prediction of $\bar{\varepsilon}$ is very accurate for all conditions. This is expected since the cost function was calculated based on this parameter. However, the correlation of ε_1^{sim} and ε_2^{sim} is relatively acceptable, even though these parameters are not directly targeted in the cost function.

Temperature sensitivity of the parameters

Figures 3.26a, 3.26b and 3.26c show the evolution of the identified parameters K, W and σ_y, respectively, with respect to temperature, ranging from 70 to 140°C. It is obvious from the plots that the identified parameters exhibit an approximately linear decrease. Based on this observation, a linear trend is proposed to characterize the temperature sensitivity of these parameters.This may not be an optimal description but such an approximation offers a compromise between the number of parameters involved and the precision of the results.

As mentioned earlier, the temperature sensitivity of Young's modulus is modeled based on equation 2.10. A generalized equation of G'Sell and Jonas model is then given as:

$$\begin{cases} \bar{\sigma}(\bar{\varepsilon}, \dot{\bar{\varepsilon}}, T) = E_1 \cdot \exp\left(A_E\left(\frac{1}{T} - \frac{1}{T_g}\right)\right) \cdot \dot{\bar{\varepsilon}}^m \cdot \bar{\varepsilon} & \text{for } \bar{\sigma} < \sigma_{\mathrm{y}} \\ \bar{\sigma}(\bar{\varepsilon}_p, \dot{\bar{\varepsilon}}, T) = [(C_1T + C_2) + (C_3T + C_4) \cdot (1 - \exp(-(C_5T + C_6) \cdot \bar{\varepsilon}_p))] \cdot \dot{\bar{\varepsilon}}^m & \text{for } \bar{\sigma} > \sigma_{\mathrm{y}} \end{cases} \tag{3.6}$$

Where the constants E_1, A_E, C_1, C_2, C_3, C_4, C_5 and C_6 are listed in Table 3.9.

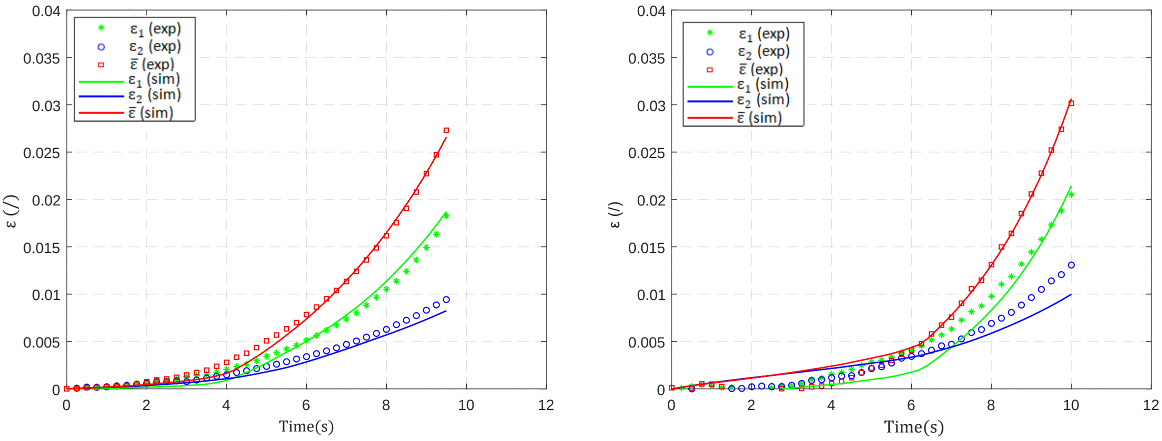

(a) RT and V=0.1mm/s

(b) T=70°C and V=0.1mm/s

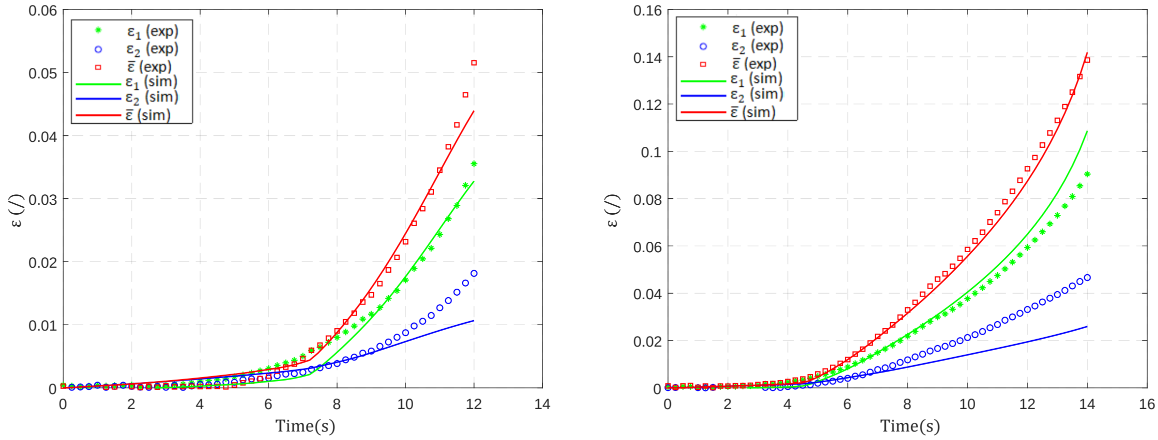

(c) T=100°C and V=0.1mm/s

(d) T=120°C and V=0.1mm/s

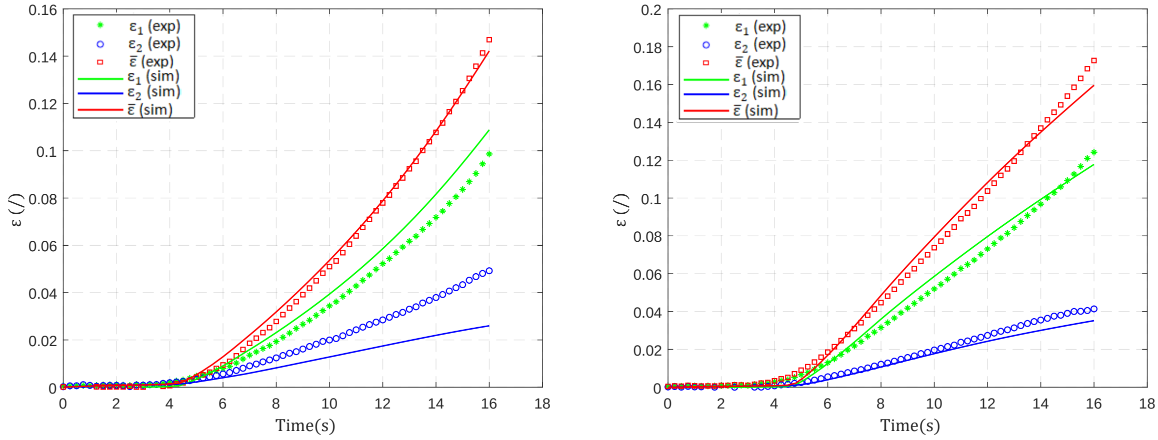

(e) T=130°C and V=0.1mm/s

(f) T=135°C and V=0.1mm/s

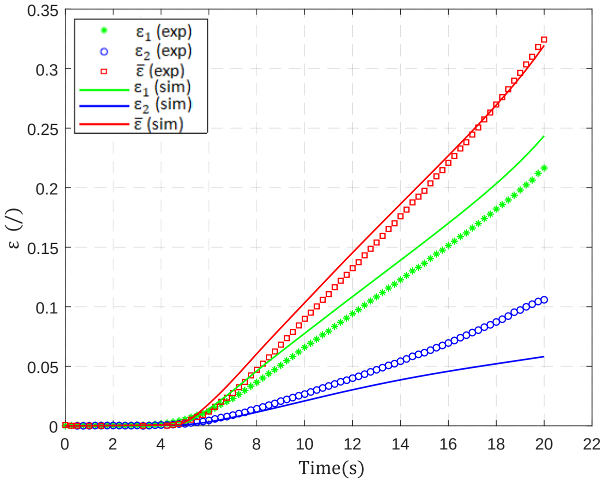

(g) T=140°C and V=0.1mm/s

Figure 3.25: Comparison of experimental and numerical deformation curves at temperatures ranging from RT to 140°C

Table 3.9: Temperature dependent model constants

E_1	A_E	C_1	C_2	C_3	C_4	C_5	C_6
12255	915	-0.37	57.5	-0.26	55.7	-1.57	229

Verification of the negligible strain rate sensitivity

As an attempt to check for the negligible strain rate effect at high temperatures, the new model equation is implemented to simulate an in-plane biaxial tensile test performed at T=120°C and a test velocity of 10mm/s (intermediate strain rate). Figure 3.27 shows the comparison between the simulated and experimental principal strains. The results indicate that the model calibrated from the quasi-static tests (velocity of 0.1mm/s) is capable of predicting the principle strains at a higher velocity (intermediate strain rate). In other words, the assumption of considering the strain rate sensitivity parameter m as a constant for tests at elevated temperature is verified.

3.4 Conclusion

The ability of a model identified from the conventional uniaxial tensile tests to accurately represent the behavior of the material subjected to multiaxial stress state can be questionable. Therefore, non-conventional mechanical characterization techniques such as biaxial

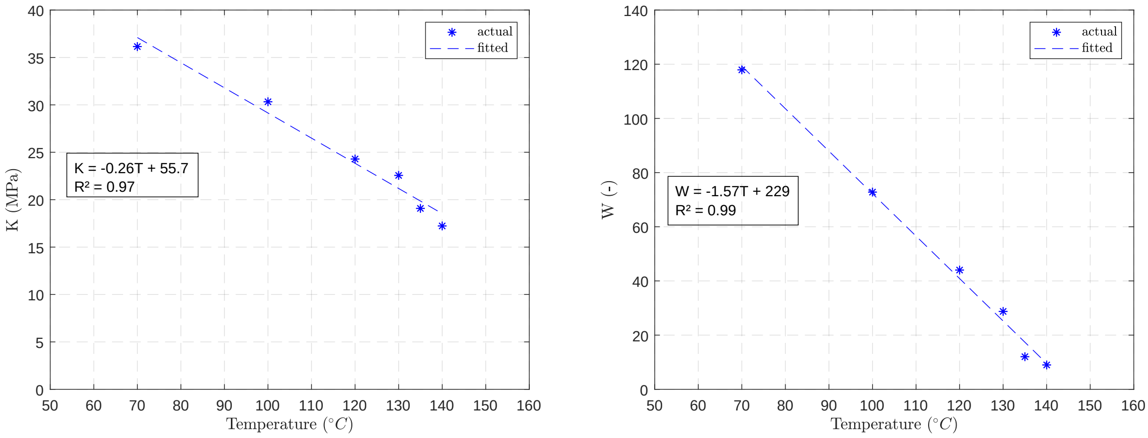

(a) Temperature variation of K

(b) Temperature variation of W

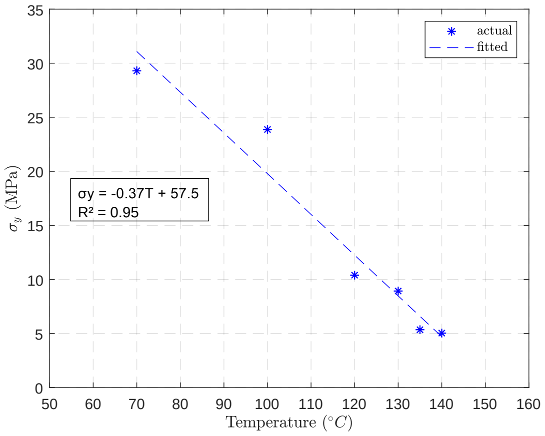

(c) Temperature variation of σ_y

Figure 3.26: Temperature sensitivity of model parameters K, W and σ_y

tensile tests might be applied for an accurate modeling of the material's behavior.

In this chapter, in-plane biaxial tensile tests on a dedicated cruciform specimen were performed at different loading conditions (two load velocities 0.1mm/s and 10mm/s are tested at RT, 70 and 120°C). Experimental temporal evolution of principal strains obtained at these conditions showed that the temperature increase at a quasi-static load rate induces higher deformation levels than an intermediate load rate. This has lead to the conclusion that the formability of the material will be better at higher temperatures and at quasi-static strain rate.

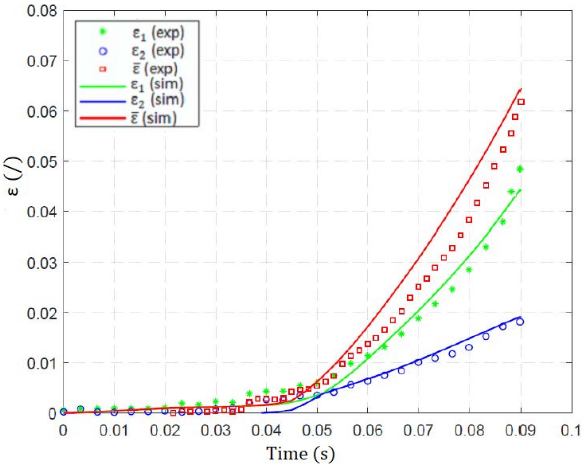

Figure 3.27: T=120°C and V=10mm/s

Consequently, additional quasi-static tests are conducted at higher temperatures reaching 140°C. The latter induced an equivalent deformation level up to failure of 33%. This parameter increased exponentially with temperature increase, whereas, the maximal biaxial average load attained decreases linearly with temperature.

On the other hand, the material model calibrated from the uniaxial tensile tests in Chapter 2 is applied to simulate the in-plane biaxial tensile test. The poor agreement between the numerical and experimental principal strains was as expected. Therefore, it was proposed to re-calibrate the model parameters according to the biaxial tensile tests database using the FEMU approach. Two different optimization strategies were considered. The first one consisted in including both uniaxial and biaxial test results in the optimization scheme. The second relied on the biaxial results only. The first strategy introduced the Pareto Front concept which, in this case, can serve as a tool to select the model parameters based on the expected material behavior, i.e. uniaxial, biaxial or a compromise between both.

For cases where the material is certainly subjected to a biaxial stress state (e.g. during forming), calibrating the parameters with the second strategy gives more accurate description of the behavior. The temperature evolution of the identified parameters issued from this calibration strategy, was evaluated . A generalized formulation of the model was then generated for other simulation purposes.

In the next chapter, the effect of the material characterization technique i.e. the parameter calibration strategy will be evaluated by simulating a hot forming process.

Chapter 4

INVESTIGATIONS ON THE HEAT ASSISTED INCREMENTAL SHEET FORMING

4.1 Introduction

In the preceding chapters, identifications of the thermo-mechanical behavior of a reinforced thermoplastic were carried out, making certain simplifying assumptions regarding the formulation of the behavior law. The model was calibrated based on two experimental databases: uniaxial and in-plane biaxial tensile tests using cruciform specimens.

The objective of this chapter is to explore the influence of the identified constitutive equations on the simulation of a forming process (in particular the forming forces and shaped profile). In other words, check which material characterization technique (uniaxial or biaxial) is more adapted for this application. An innovative technique for the forming process is adopted, which is Heat Assisted Incremental Sheet Forming (HAISF). This method is still under research and development, especially for thermoplastic polymers and fiber reinforced thermoplastics. In this work, a HAISF device is developed and tests are conducted at specified conditions that align with the ones of the material characterization. A truncated cone is formed. Then, the experimental and numerical results in terms of forming force and the final shape of the piece are compared to evaluate their consistency. The chapter begins with a concise overview on HAISF, its working principle, application, heating techniques... After that, the experimental set-up used to carry out the HAISF of a fiber reinforced polypropylene cone is detailed. Then, the numerical approach of this topic is addressed. It starts with a parametric study performed on a simplified FE model (forming 1/4 of the plate), where the effect of the behavior law and forming temperature is addressed. Thereafter, a simulation of the forming process is carried out, with conditions comparable to those applied during the experimental forming operation. The experimental and numerical results are subsequently compared. This verifies the reliability of the identified phenomenological model in accurately predicting the previously-mentioned forming outcomes of glass fiber reinforced polypropylene.

4.2 Incremental sheet forming (ISF)

Incremental sheet forming (ISF) is an innovative, non-traditional sheet forming process that uses relatively simple, non-expensive tools [148]. ISF can be an interesting technique for prototyping and low-volume production of complex shapes ([149], [150]). Common concerns of this process are the relatively high production times involved and the dimensional accuracy of the formed part. The springback after unclamping the formed part is also debatable in this type of sheet forming ([151][152]). The primary principle of ISF involves moving a generic shaped tool along a defined path to progressively shape the entire part through localised deformations. There are three primary categories of ISF processes [153]: single-point, two-points, and double-sided ISF. The first relies on a single generic tool for the forming process. For the second, an additional partial or full die is required. The last involves the use of two generic tools, with one of them serving as a kinematic support on the lower side of the sheet. The choice between the three depends on the specific requirements of the part being formed, such as its geometry, depth, and material properties. Figure 4.1 illustrates the ISF (single-point) principle, which will be regarded in this work. Various trajectories can be applied to shape the desired form, including truncated cones or pyramids, which are often considered as reference geometries. Computer aided manufacturing (CAM) software is generally used to generate the trajectories. For instance, in the case of cone shaping, the most frequently used trajectories for the tool along $Zaxis$ (depth direction) are (see Figure 4.2):

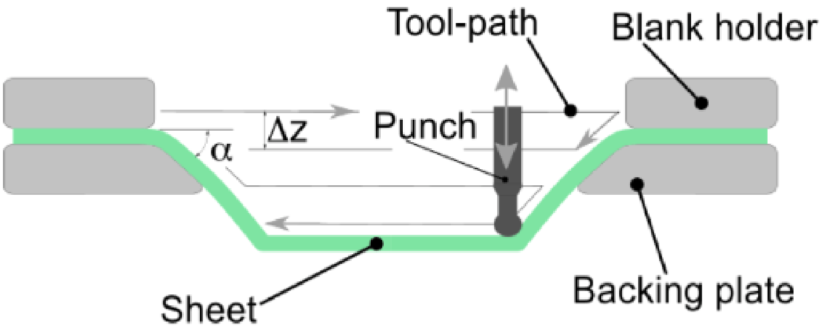

Figure 4.1: Principle of Incremental Sheet Forming [154]

a)Helical: The tool head follows a continuous path that defines the geometry. A helix pattern is created in the formed part as the tool moves along the X, Y, and Z axes.
b)Stepped: The transition of the tool from one level to the next begins by moving in the XY plane first, then stepping down along Z axis (with a constant depth increment Δ_Z).

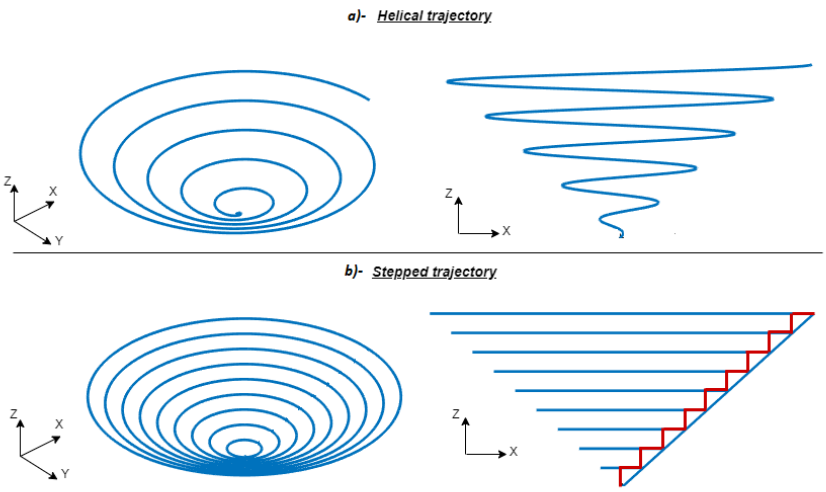

Figure 4.2: Common strategies applied in ISF

Traditionally, incremental sheet forming involved modifying a CNC machine to accommodate the punch or forming tool [155]. On the other hand, advancements in robotics have enabled the utilization of robots as programmable tools for incremental forming. This can be accomplished by attaching the punch to the robot's end, enabling it to draw the desired shape ([156],[157]). Figure 4.3 shows both setups for possible ISF configurations. Research efforts in the domain of ISF have been centered on metals ([156], [160], [161]). For example, Fratini et al. [160] investigated the formability of three steel grades undergoing

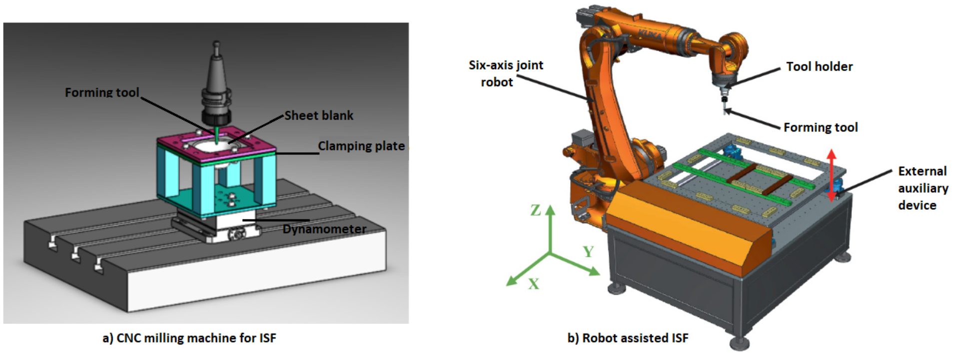

a) CNC milling machine for ISF

b) Robot assisted ISF

Figure 4.3: CNC milling machine [158] and robot assisted ISF [159]

ISF. Trzepiecinski et al. [161] reviewed the recent developments and future challenges in the ISF of aluminium alloy sheets. Moreover, this process has also started to make its way towards the automotive sector. Amino Corp. [162] employed the incremental sheet forming process to fabricate the hood of the Honda S800. Also, this technique has been recently introduced in the biomedical field. It presented an interesting option for producing single-use, customised parts like skull implants or ankle brackets [163].

Apart from metals, there is an expanding scope for ISF application to other materials. Franzani et al.[164] were among the first to conduct incremental forming for polymers (PVC sheets). Their study aimed to provide a thorough exploration of characterizing and assessing the formability limits of the process. This investigation considered variables such as the type of polymer and key operational parameters as factors influencing the outcomes. Zhu et al.[165] reviewed recent research on thermoplastic-focused ISF processes.

It's worth noting that traditional incremental sheet forming might not be the optimal choice for materials with poor overall ductility at room temperature, such as fiber reinforced polymers (FRP). Consequently, researchers have developed various methods of HAISF with the intention of enhancing the formability of such materials [166].

4.3 Heat assisted incremental sheet forming (HASIF)

By introducing heat during the ISF forming process of fiber reinforced thermoplastics, the matrix material softens, allowing for easier deformation and shaping. This can be beneficial for creating complex geometries and achieving tight radii while minimizing shape inaccuracies. However, it's crucial to keep in mind that for thermoplastics, careful control of temperature and heating duration is essential to prevent thermal degradation of the matrix. Researchers ([166], [167]) have reviewed the latest advancements in incremental sheet forming, including potential effective heating methods. Among the existing heating techniques, electric, hot air, optical and friction stir are briefly discussed.

Electric heating - Joule heat This type of local heating allows good control of the heat, which ensures a constant temperature on the lower surface of the sheet. The heating system employs an electric resistance element as its heat source. Within this system, a thermally insulated chamber is constructed to retain the sheet material. Subsequently, the electrical resistance generates thermal energy, warming the air within the chamber to facilitate heat transfer between the air and the thermoplastic material. To monitor and regulate the temperature of the sheet's upper surface, a thermal camera and a control unit are utilized. Figure 4.4 shows a schematic diagram of an electric heating system. Conte et al.[169] and Ambrogio et al.[168] designed this heating system to form a sheet made of a short glass fiber reinforced polyamide-6 sheet. Forming temperatures of 150°C and 200°C are tested.

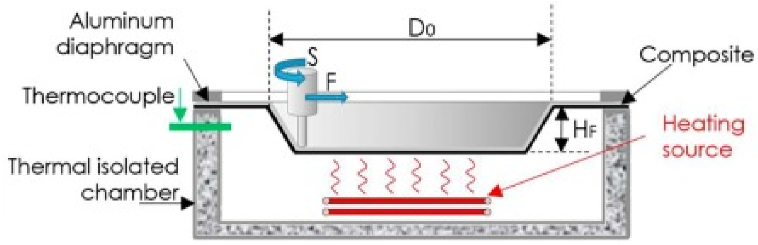

Figure 4.4: Schematic of an Electric HAISF ([168], [169])

Hot air heating - Convection The hot air heating system includes an isolation chamber and comprises a hot air blower positioned alongside the clamping device. The resistance heaters coupled with the air blower provide hot air to the holding fixture. Hot air heating is considered as a global heating technique. The temperature is controlled by an analog controller linked to a thermocouple.
The setup shown in Figure 4.5 was used by Al-Obaidi et al. [170] to form a hybrid laminated composite made of basalt fiber reinforced polyamide-6 combined with aluminum sheets. The same authors [171] also applied this technique to form glass fiber reinforced polyamide-6. The hot air temperature was regulated to maintain the formed part at a temperature around 150°C.

Optical heating - Radiation This method is a local heating technique that uses halogen lamps to heat the sheet in a reciprocating motion of the forming tool. The halogen lamp is located on the same axis as the tool but on the opposite side of the sheet. According to the review conducted by Liu [166], a maximum temperature of 300°C can be achieved with the halogen lamp optical heating technique. A schematic of this heating method is shown in Figure 4.6. This setup was developed by Okada et al.[172] to perform

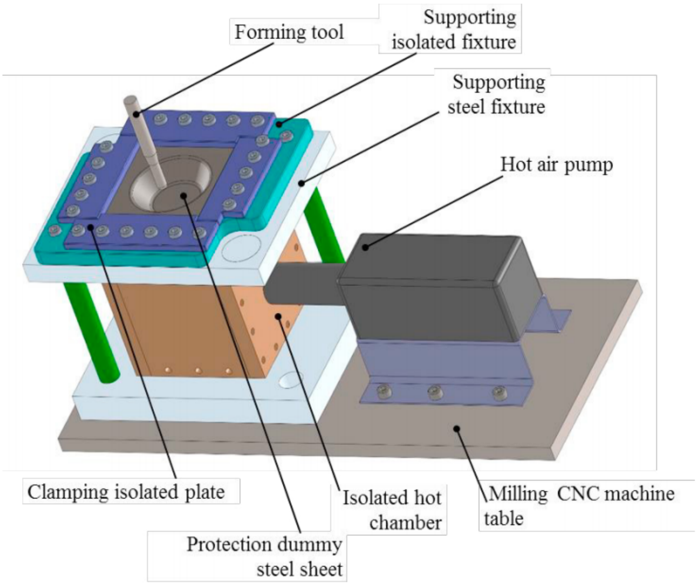

Figure 4.5: Schematic of a hot air HAISF [170]

HAISF of discontinuous carbon fiber reinforced polyamide-6. The sheet reached a forming temperature of approximately 200°C.

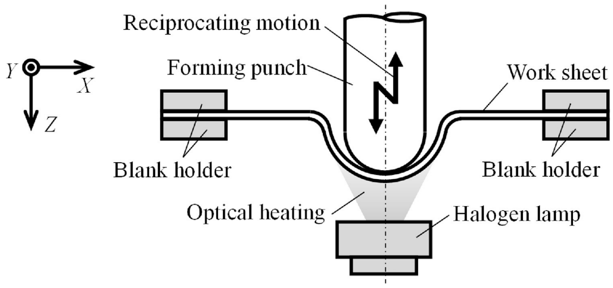

Figure 4.6: Schematic of a Optical HAISF [172]

Friction stir heating - Friction Friction stir is the simplest heating technique applied in HAISF (Figure 4.7) which is known for the lowest cost of hardware configuration. This method consists in softening the material with the localized heat generated from the friction at the interface between the rotating tool and the workpiece. The amount of friction-induced heat is mainly related to the tool rotation speed ([173],[174]). However, the challenge in controlling the temperature, the poor surface finish and severe tool wear are factors that limit the use of this technique [166]. The concept of frictional heating was investigated by Lozano-Sánchez et al.[175] to shape a conic geometry made of Carbon

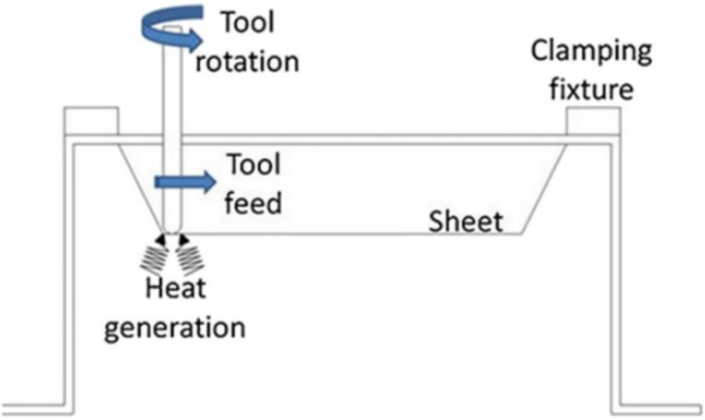

Figure 4.7: Schematic of friction stir incremental forming [166]

Nanotube polypropylene composite. The authors compared two different forming scenarios. In the first case, forming was conducted without any heating, which means there was no tool rotation (0 rpm). In the second scenario, a tool rotation speed of 2000 rpm was applied.

This technique can be combined with the previously mentioned heating methods. In a study conducted on a thermoplastic polymer (polymethyl methacrylate), Conte et al.[176] formed the part using the electric heating setup discussed earlier combined with a frictional heating achieved with the rotating tool (speed range: 100-6000 RPM). The initial temperature range imposed by the electric heating was ranging from 80°C to 100°C. They concluded that the impact of external electric heating, responsible for attaining the forming temperature, has a more significant effect on product quality compared to the internal friction heating generated from the rotating forming tool.

It can be concluded that any of these techniques can be used for thermoplastics and fiber reinforced thermoplastics, as long as the right forming temperature required for the tested thermoplastic is attained. The choice of the heating method depends mainly on the material as well as the overall forming set-up used.

In this study, the incremental forming of a 40% glass fiber reinforced polypropylene plate takes place after heating the part with hot air until reaching the desired forming temperature. More details on the forming process and test apparatus will be provided in the subsequent sections.

4.4 Experimental testing of HAISF

This section focuses on the experimental forming operation. It begins with details on the tested material, as well as the chosen geometry and theoretical tool path. It then discusses the heating phase prior to forming. Next, it presents the forming stage, with a description of the experimental set-up. Finally, the section concludes by discussing the experimental results.

4.5 Material, geometry and methodology

In this work, it is intended to apply HAISF for shaping a flat 40%GF/PP sheet with thickness of 2mm into a 45° cone, as shown in Figure 4.8. This geometry has been investigated in a previous study [156]. As mentioned earlier, the conical shape serves as a reference geometry often used in ISF. The sheet is securely clamped onto a rigid backing fixture, which holds the sheet in place while enabling the required tool movement. The clamping system comprises a cylindrical frame and clamp, both made of steel (Figure 4.9). During ISF, a helix trajectory of the tool can be better than a stepped trajectory. The gradual and continuous motion of the helix trajectory can result in improved surface finish of the formed part. This is particularly important when working with delicate sheet

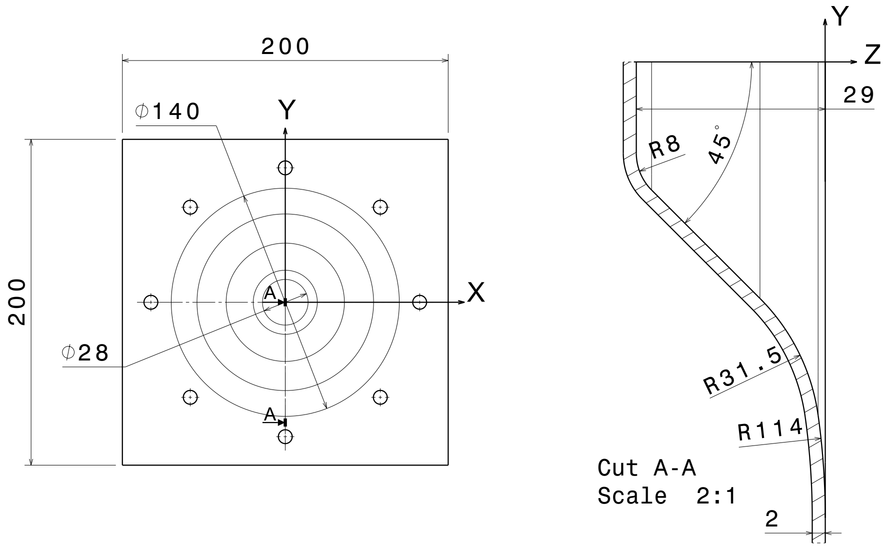

Figure 4.8: Geometry of formed cone (Dimensions in mm)

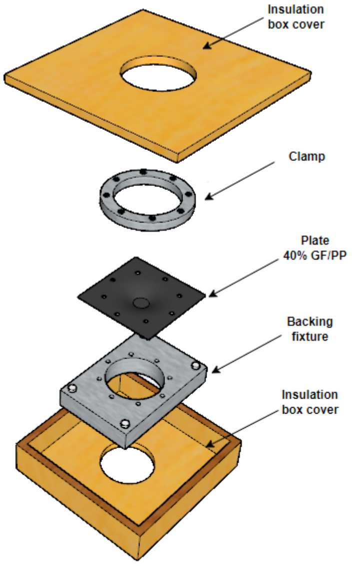

Figure 4.9: Clamping and insulation system

surfaces such as fiber reinforced polymers. Also, the material flow is thought to be more uniform, preventing localized thinning or wrinkling of the material. The part of the trajectory applied experimentally down until the end of forming (maximum depth attained before fracture occurs) is shown in Figure 4.10.

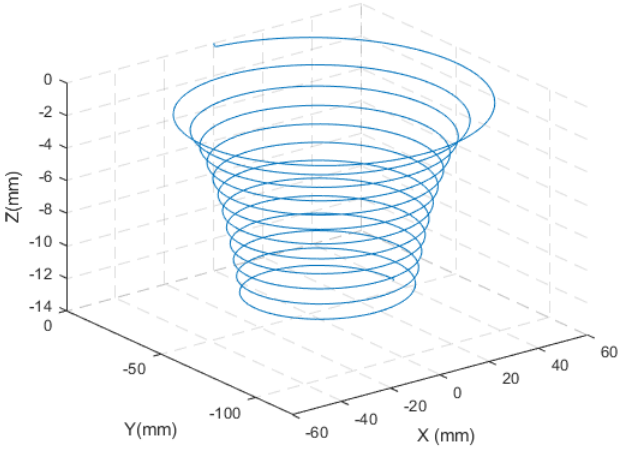

Figure 4.10: Helix trajectory applied in the experimental setup

The tool used in this HAISF process is a hemispherical-ended punch with a diameter of 15 mm. This shape facilitates effective localized deformation of the sheet by concentrating the force at a specific point. The tool is made of a high-strength material to withstand the

mechanical loading and thermal fluctuations encountered throughout the forming process. The tool is mounted on a robust and adjustable support system to ensure stability and precise control of the forming operation. This support system allows for controlled tool motion and provides the necessary force for the incremental forming.
The hot air heating system used to heat the plate up to the desired forming temperature is described in the following section.

4.5.1 Heating stage

Prior to forming, the plate undergoes a heating phase, as illustrated in the schematic diagram presented in Figure 4.11. The heating device consists of a hot air generator that can provide a temperature range of -75°C to 200°C. Heated air flows through an inlet pipe connected to the lower part of the set-up (plate+clamping system). The upper part is closed with the outlet pipe where the air returns to the generator. This forms a closed heating loop resulting in an efficient, faster and global heating of the plate. Two Thermocouples fixed to the upper and lower surfaces of the plate are employed to monitor the temperature of these surfaces. Additionally, a probe situated inside the insulated box (at the entrance of the hot air) measures the temperature within it. This probe is used for temperature regulation.

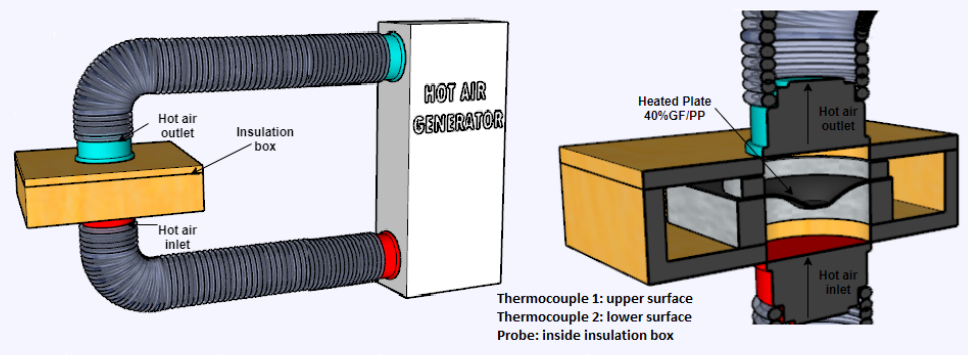

Figure 4.11: Heating system prior to forming

Based on the thermal properties of glass fiber reinforced polypropylene, particularly the material's melt temperature, as well as taking into account the equivalent strain levels achieved during the in-plane characterization (discussed in Chapter 3), a decision is made to conduct the forming process of the plate at a temperature around 140°C. At this point, the tested material becomes sufficiently malleable without reaching the melt temperature, which would have damaging effects on the material.

Heating trials are conducted to check for the temperature required inside the insulated box which enables the plate to reach the desired temperature. It was found that maintaining the insulated box at 155°C (measured with the probe) guarantees that the plate reaches an upper and lower surface temperatures of 135°C and 140°C (measured with thermocouples), respectively. The evolution of the measured temperatures with respect to heating time are presented in Figure 4.12. The target temperature of the insulated box is approximately reached after 80 min of heating. 15 min later, the lower and upper surfaces of the plate achieve a desired temperature range. Heating is then held for an additional 25 min. In spite of this, the temperature gradient of 5°C remains apparent between the lower and upper surfaces.

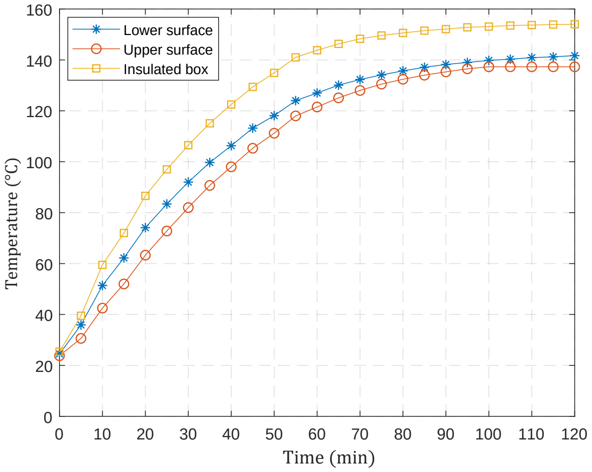

Figure 4.12: Heating temperature variation before forming process

4.5.2 Forming stage

The HAISF operation is carried out on the robot-assisted experimental setup shown in Figure 4.13. The schematic diagram of whole experimental setup is presented in Figure 4.14 for a better visualization. At the end of the heating stage, the outlet pipe of the hot air is removed, uncovering the circular opening at the top of the insulation box. Then, the robot arm hovers over this opening to bring the tool into the initial forming position. It's important to note that the tool is not preheated before the forming operation; however, it does experience moderate heating during the test. This occurs as soon as the tool gets exposed to the hot air coming from the opening at the top of the insulation box. The

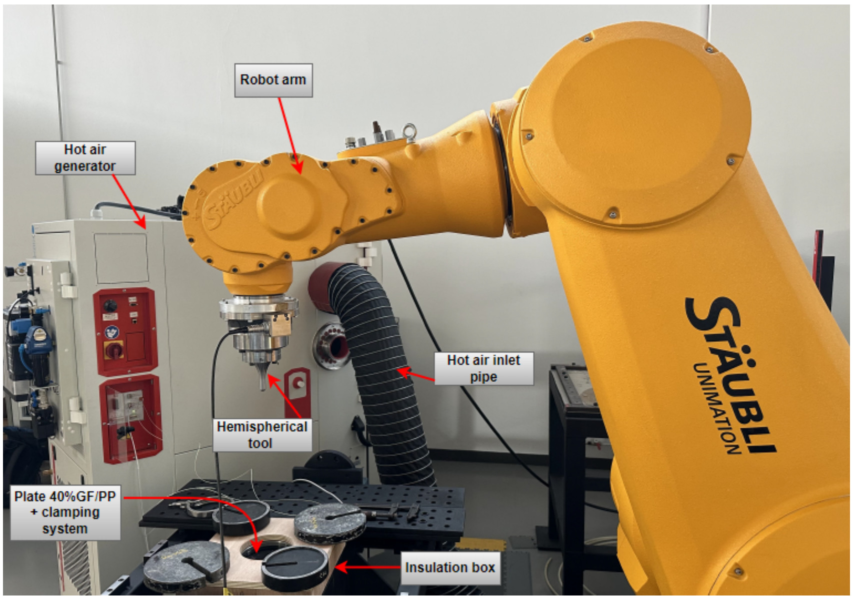

Figure 4.13: Experimental setup of HAISF

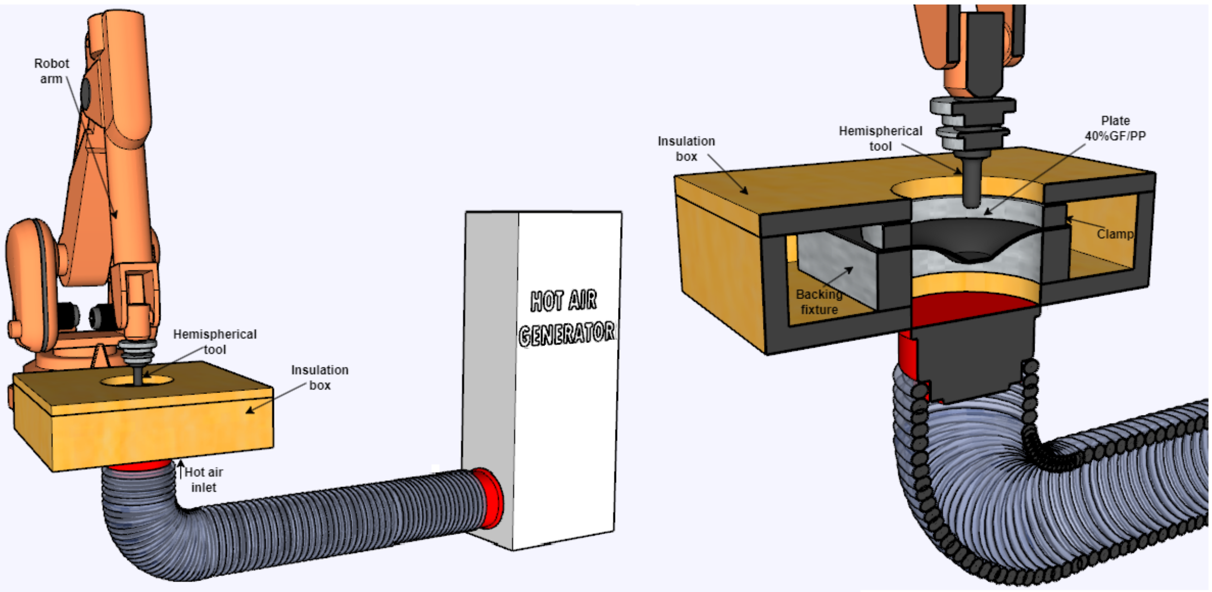

Figure 4.14: Schematic diagram of HAISF experimental setup in formage stage

clamping system is designed to sustain a continuous flow of hot air in a way that ensures the upper surface of the plate remains heated, even after the outlet pipe has been removed. A lubrication layer is applied to the contact surface between the plate and the forming tool. This reduces friction and facilitates smoother deformation.

The conical workpiece is deformed according to the test parameters listed in Table 4.1.

The tool is at room temperature at the beginning of the forming.

Table 4.1: Parameters applied in the experimental tests of the HASIF

Tool	Shape	Hemispherical
	Diameter (mm)	15
	Velocity (mm/s)	10
Sheet	Dimensions (mm)	200 × 200
	Thickness (mm)	2
	Material	40% GF/PP

The force applied by the tool to the plate is measured by a load cell positioned between the forming tool and the robot arm. This sensor has a load capacity of ± 9000 N along the axial direction, ± 3600 N along the radial direction and ± 700 Nm for measuring moments with a resolution of ± 3 N along the axial direction, ± 1.5 N along the radial directions and ± 0.2 Nm for the moments. The force is recorded at a frequency of 40 Hz with acquisition cards coupled to LabView software.

The shaped profile obtained before unclamping the formed plate is measured using a 3D (laser) scan technique which consists in projecting a laser beam onto the surface of the plate. The laser reflects off the surface, and the scanner captures the reflected light to create a point cloud representation of the surface. Each point in the cloud is defined by XYZ coordinates.

4.5.3 Results and discussion

The following section presents the results of the robot-executed HAISF. These results include the forming forces measured on the tool along with the obtained deformed profiles. The experimental data will be compared with the FE simulation results in section 4.6.5.

4.5.3.1 Forming forces

The axial and radial forces, F_Z and F_R applied by the tool are with respect to the axial tool displacement Z are presented in Figures 4.15a and 4.15b, respectively. The axial force F_Z reaches a maximum of 135N, whereas the radial force increases to 45N. The sudden drop in F_Z along with the constant F_R after 200s, indicates the end of forming or beginning of rupture within the plate. This forming time of 200s (approximately 3min) is equivalent to an axial tool displacement of 9mm along Z axis.

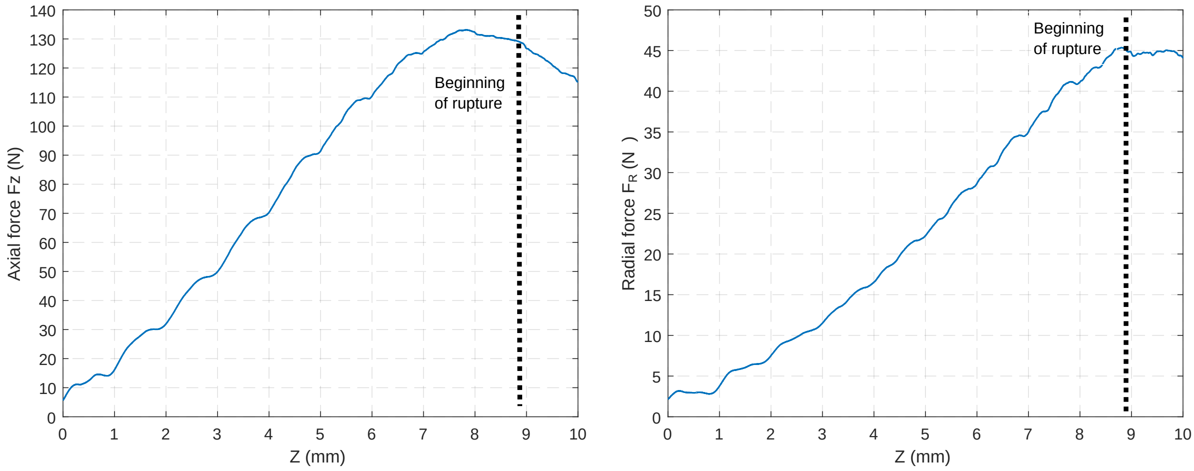

(a) Axial tool force F_Z.

(b) Radial tool force F_R.

Figure 4.15: Axial and radial tool forces measured experimentally with respect to Z.

4.5.3.2 Profiles of the shaped part

The formed part is presented in Figure 4.16a. As mentioned earlier, the profiles in XZ and YZ planes are obtained using the 3D scanning technique. Figure 4.16b shows the depth (along Z) of the cone with respect to the diameter (along X or Y). A maximum forming depth of approximately 9mm is achieved. When this value is exceeded, it causes the formation of a crack that propagates along the YZ plane. The profile measurements along this plane exhibit scattering, primarily due to the fracture's location, which extends along a 30mm radius in the Y direction. This scattering contributes to the observed deviation between both profiles.

The same forming operation is repeated under identical operational conditions in order to check for repeatability. The measured forming forces and profiles remains consistent.

4.6 Finite element modeling of HAISF

In this section, a FE model of the ISF process is developed with the primary purpose of conducting a parametric study to investigate the influence of parameters such as temperature and behavior law on the forming forces and final form of the workpiece. This is beneficial to optimize the operating conditions. Also, one can have a good prediction of the maximum forming force which in turn, serves for the dimensioning of the robot, i.e. choos-

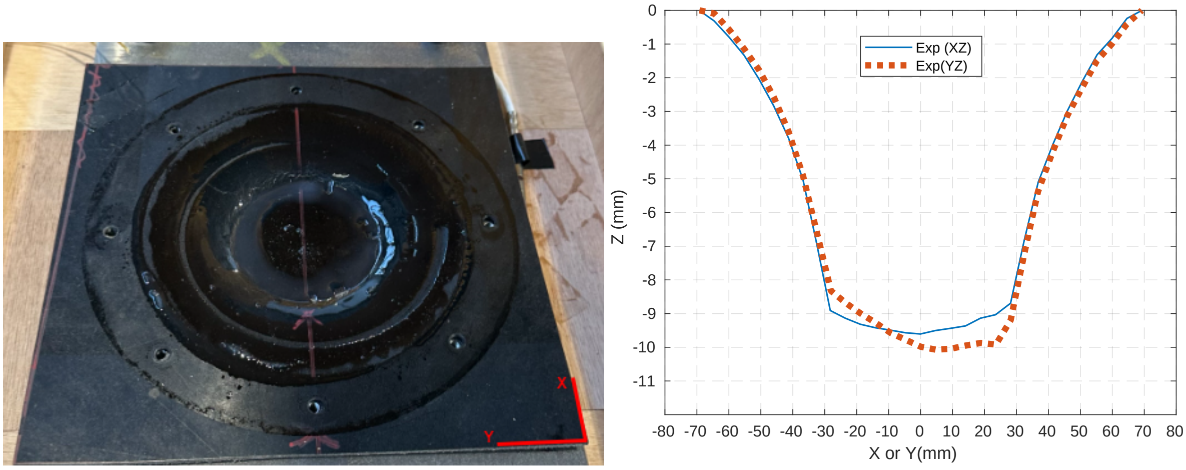

(a) Formed part (b) Post processed profile in XZ and YZ planes

Figure 4.16: Profile of the formed part obtained from the incremental sheet forming of the 40%GF/PP plate

ing an appropriate capacity and evaluating precision by analysing its elastic response. For the parametric study, a simple FE model of the incremental sheet forming is established using ABAQUS software (static-implicit solver), based on the commonly employed assumptions found in the literature. These assumptions involve considering shell elements and clamped sheet edges as boundary conditions ([156], [177], [178]). In a subsequent step, the simulation of the process with the previous conditions will be proposed.

4.6.1 Tool trajectory and Boundary conditions

In order to simplify and reduce the computational time, the parametric study is carried out using a quarter of the model. The stepped tool path shown in Figure 4.17 is considered. Such trajectory enables the modelling of only 1/4 of the plate, making it easy to input the transition between the tool's withdrawal and entry points. In each cycle, the tool maintains a maximum axial or radial depth of increment of 1mm.

Fixed edges are usually applied in the literature. In reality, local bending or sliding can occur at the junction between the sheet and the clamping system and reduce the predicted force level. Belchior [156] modelled the clamping system by considering two distinct boundary conditions. The first approach defined fixed conditions at the sheet boundaries. The second approach utilized a uniform pressure field applied to the contact between the sheet and the clamping device.

Upon comparing the simulated tool reaction forces (axial and radial) to experimental ones,

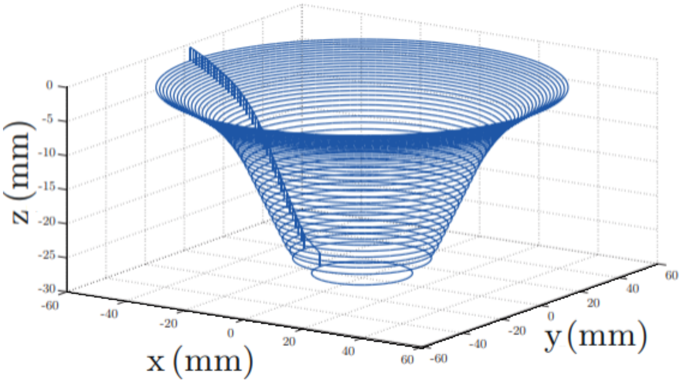

Figure 4.17: Desired Trajectory / Tool trajectory with successive circular contours (constant Δ_z)

Belchior found that up to a forming depth of 20mm, there was a relatively minor difference in simulation force levels between both boundary condition models. However, for greater forming depths (>20mm), a relatively larger disparity emerged, with the results of the second boundary condition model closer to experimental values compared to the fixed conditions.

Additionally, their study assessed the impact of defining a friction condition between the tool and the sheet. Comparing a frictionless model to a model with a specified friction coefficient, shows no significant differences in the radial forces [156].

Considering the maximum forming depth expected for the material examined in this work (less than 20mm), and given the lower rigidity of the tested material compared to metals like aluminum (as seen in the case of Belchior [156]), the chosen boundary conditions will likely have a low impact on the overall behavior. Therefore, in the present study, fixed sheet edges and a frictionless tool-sheet contact condition are chosen.

4.6.2 Elements and mesh

The hemispherical punch is discretized using discrete rigid elements R3D4 (4-node 3-D bilinear rigid quadrilateral). In the work of Belchior [156], different simulation parameters were evaluated to enhance the accuracy of predicting the forming force in metal processing. The force levels achieved in a model meshed with shell elements, were compared to those in a model meshed with 3D elements. In relation to the experimental axial and radial forces, the shell model consistently overestimated the force levels to a greater extent than the 3D model. This overestimation became more pronounced for depths exceeding 20mm.

Below this value, the disparity between the shell and 3D models was not significant. In this study, building upon the behavior investigations of fiber-reinforced polypropylene conducted in previous chapters, it is anticipated that lower forming depths will be achieved (significantly less than 20mm). Accordingly, the sheet is discretized using S4R elements (4-node doubly curved thin or thick shell, reduced integration, hourglass control, finite membrane strains). A total of 1109 shell elements are employed for a quarter of the sheet (See Figure 4.18).

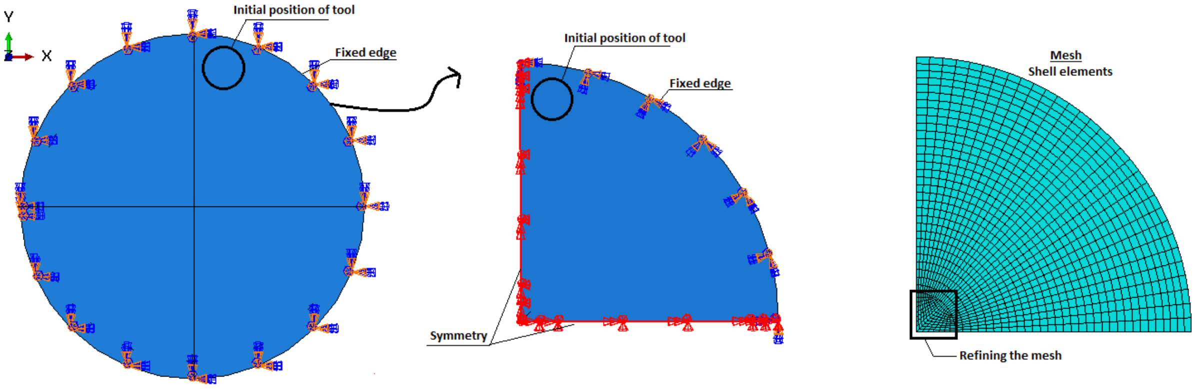

Figure 4.18: Representation of the the FE mesh

4.6.3 Material model

As mentioned earlier, one of the purposes of this chapter is to assess the pertinence of the material model in relation to the level of forming force, final profile and thickness variation. The FE simulations for heat-assisted incremental sheet forming are executed using the material models identified in Chapter 2 (equation 2.18) and Chapter 3 (equation 3.6). Based on these models, simulations are carried out at various temperatures to investigate the impact of temperature on the tool force, thickness variation and final profile. It's important to note that the temperature will be incorporated in the material model equation (temperature variation of model parameters), meaning that the simulation is conducted with a static general analysis (no thermal analysis involved i.e., coupled temperature-displacement).

4.6.4 Results and discussion

The simulated results presented in this section are the axial and radial tool reaction forces, the thickness variation, as well as the deformed profile of the cone. The effect of temperature and behavior law on the mentioned parameters are investigated.

4.6.4.1 Representation of tool reaction force

The simulated force shows a cyclic response of the tool. Each cycle corresponds to 1/4 pass at a constant depth Δ_Z, starting from the indentation till the withdrawal of the tool. For a better reading, the original evolution is replaced by a smoothed evolution (staircase signal) as presented in Figure 4.19. This representation will be applied to all simulation forces presented in this section. The force along the tool axis (Z) is defined by F_Z. The magnitude of the radial forces F_R is defined as:

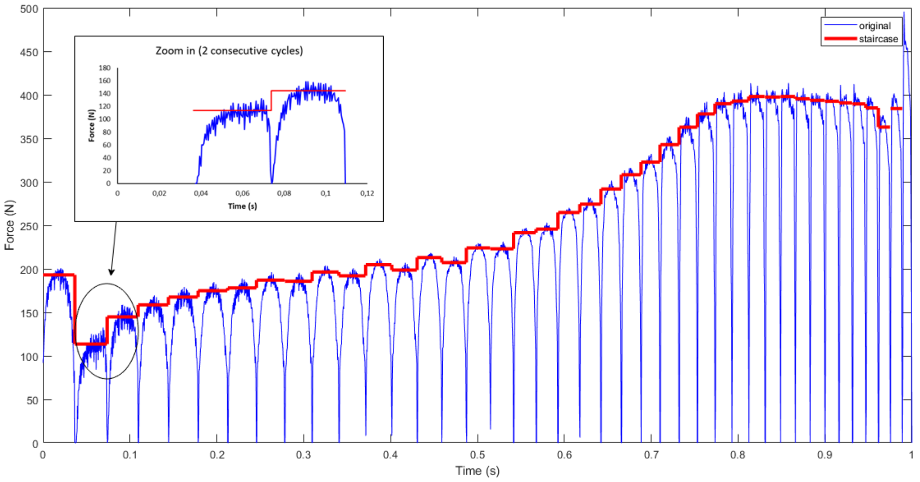

Figure 4.19: Smoothed simulated force signal

$$F_R = \sqrt{F_X^2 + F_Y^2} \tag{4.1}$$

4.6.4.2 Effect of behavior law

The influence of the material behavior law on the tool axial force is clearly shown in Figure 4.20. For T=70°C (Figure 4.20a), The difference between the simulated maximum axial force using the law identified from uniaxial tests and the one from in-plane biaxial tests is 3% relative to the maximum force obtained using the law from in-plane biaxial tests. For a higher temperature of T=120°C (Figure 4.20b) the difference in the maximum force level is 11%. For T=130°C (Figure 4.20c) the difference in the maximum force level is 21.7%. A similar difference of 22% is obtained at a temperature of 140°C (Figure 4.20d).

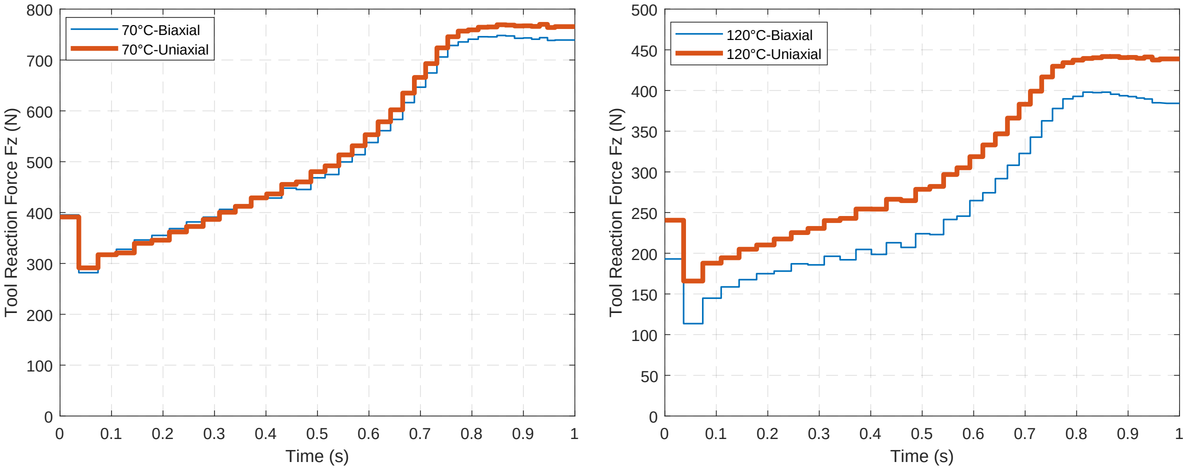

(a) T=70°C

(b) T=120 ° C

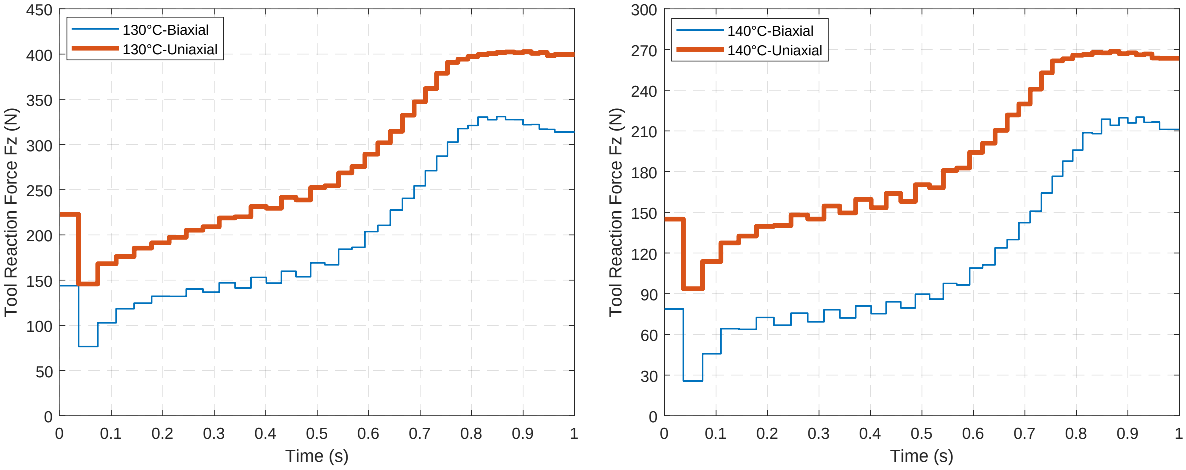

(c) T=130°C

(d) T=140°C

Figure 4.20: Effect of behavior law on the tool reaction forces Fz for different test temperatures

The results show that the behavior law effect on the tool force is clearly more pronounced at higher temperatures. This is also the case for the thickness variation as it can be seen in Figure 4.21. The disparities are the greatest at higher temperatures, especially near the central zone of the formed plate i.e. zones subjected to strong deformations, far from the fixed edges.

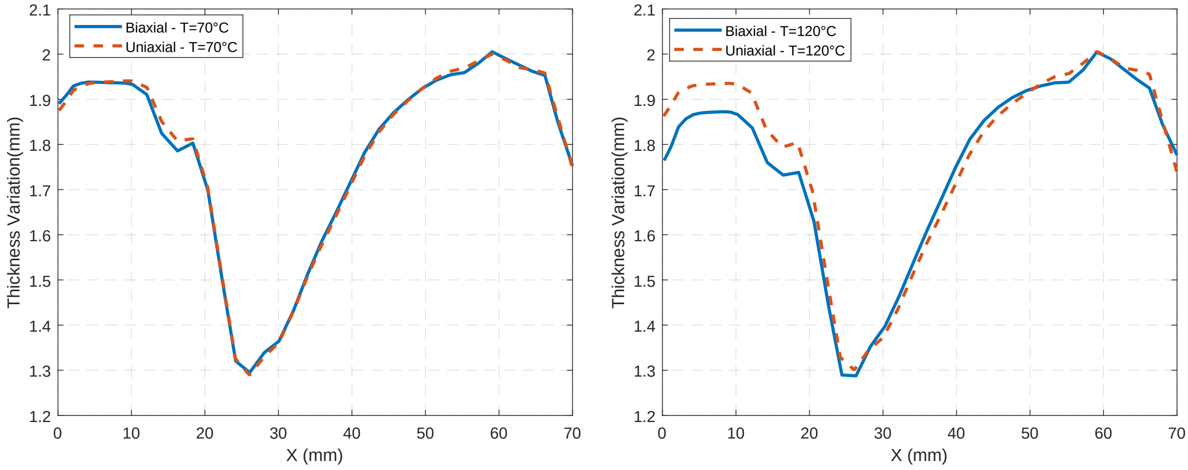

(a) T=70°C

(b) T=120° C

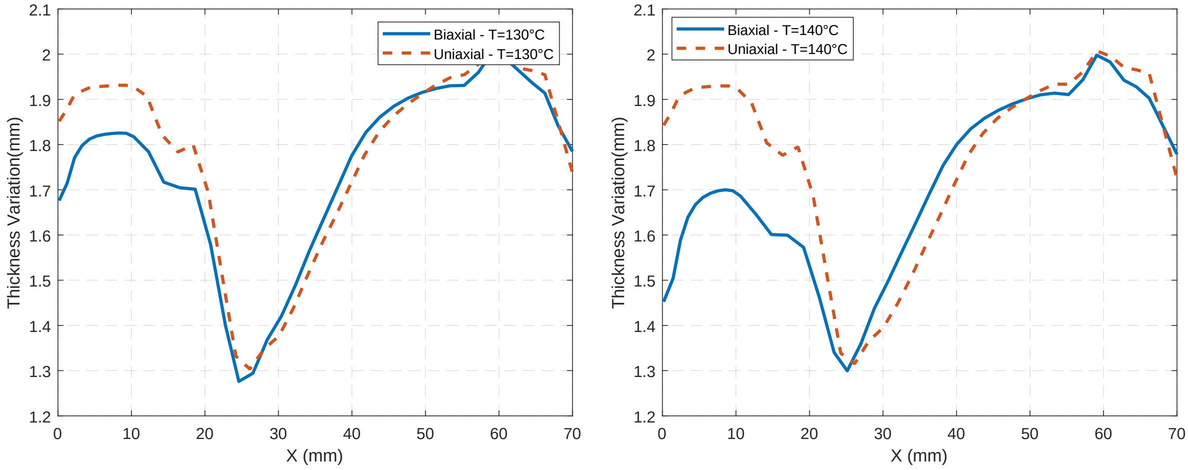

(c) T=130°C

(d) T=140°C

Figure 4.21: Effect of behavior law on the thickness variation for different test temperatures

Contrarily, the behavior law has a negligible effect on the simulated final shape for all tested temperatures as shown in Figure 4.22.

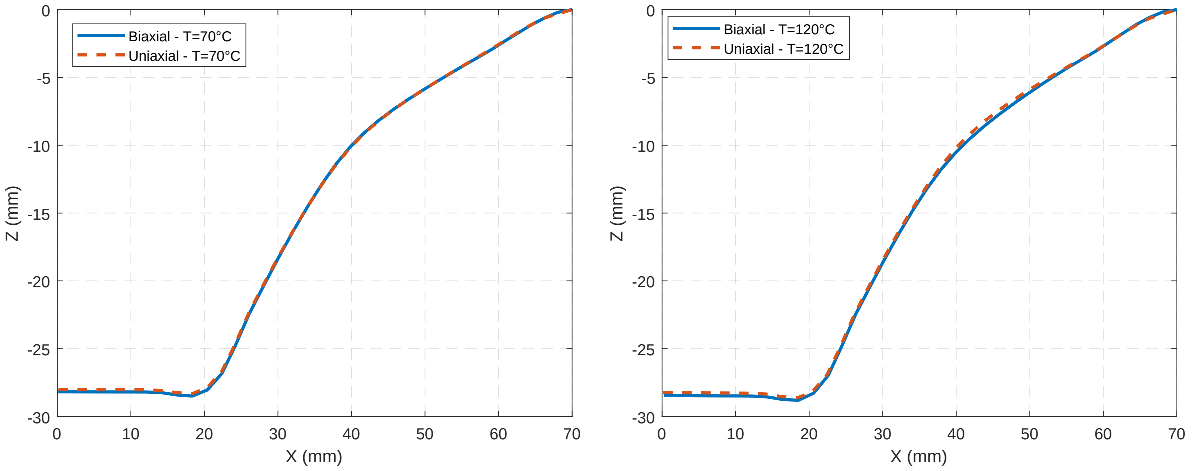

(a) T=70°C

(b) T=120°C

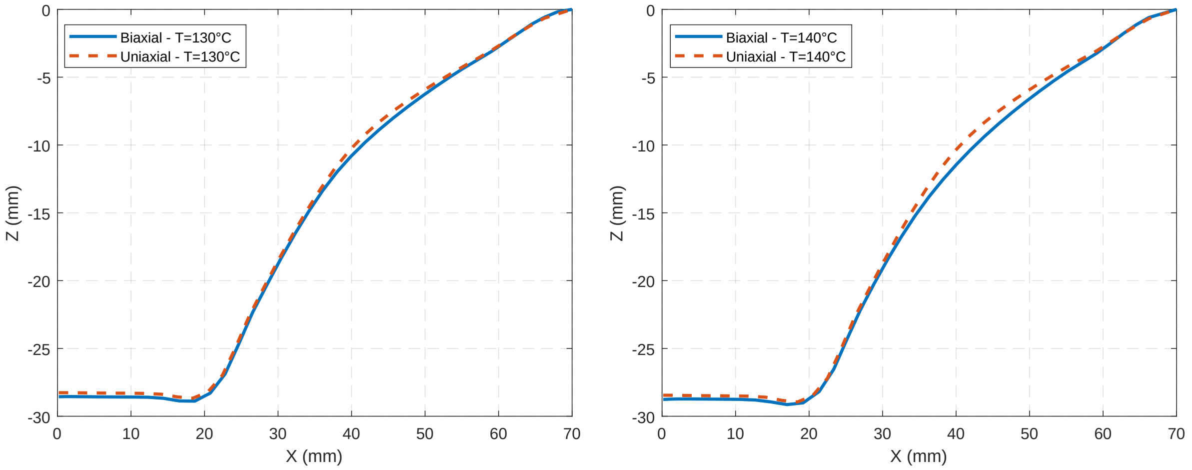

(c) T=130°C

(d) T=140°C

Figure 4.22: Effect of behavior law on the profile for different test temperatures.

4.6.4.3 Effect of anisotropy

In this work, Hill's criterion is selected to represent the anisotropic behavior of the material (Chapter 2, section (2.3.2)). In order to check the effect of this criterion to represent the forming behavior of the material, a FE simulation is conducted using the G'Sell and Jonas hardening law identified from the biaxial tensile tests with the isotropic von Mises criterion. The results of the latter are compared to those obtained using anisotropic Hill's plasticity criterion. Figure 4.23 shows the clear difference between the tool axial force Fz for both Hill and von Mises criteria simulated at a temperature of 120°C. The difference between maximum force levels at the end of forming is 200N which is a deviation of 50% relative to the maximum force level obtained with Hill's criterion. This shows that applying G'Sell and Jonas law as an isotropic model with a von Mises plasticity criterion causes a significant increase in the tool reaction force.

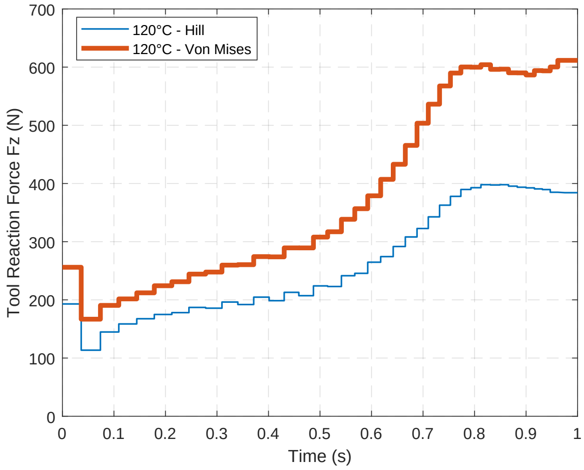

Figure 4.23: Effect of the plasticity criterion (Hill or von Mises) on the tool reaction force Fz at T=120°C.

4.6.4.4 Effect of Temperature

In this section, the G'Sell and Jonas model identified from the biaxial tensile tests combined with Hill's plasticity criterion is applied. Simulations at different temperatures, e.g. 70, 120, 130 and 140 °C are performed. Figure 4.24a and 4.24b show the clear effect of the temperature on the axial and radial forces, respectively. Obviously, as temperature increases, the maximum force level at the end of forming decreases down to the lowest value of approximately 200N for axial force and 75N for radial force, at T=140°C. The impact of temperature is also visible on the thickness variation along the radius of the plate, especially far from the fixed edge, as shown in Figure 4.25a. On the other hand, the formed shape of the plate is not affected by the temperature (Figure 4.25b).

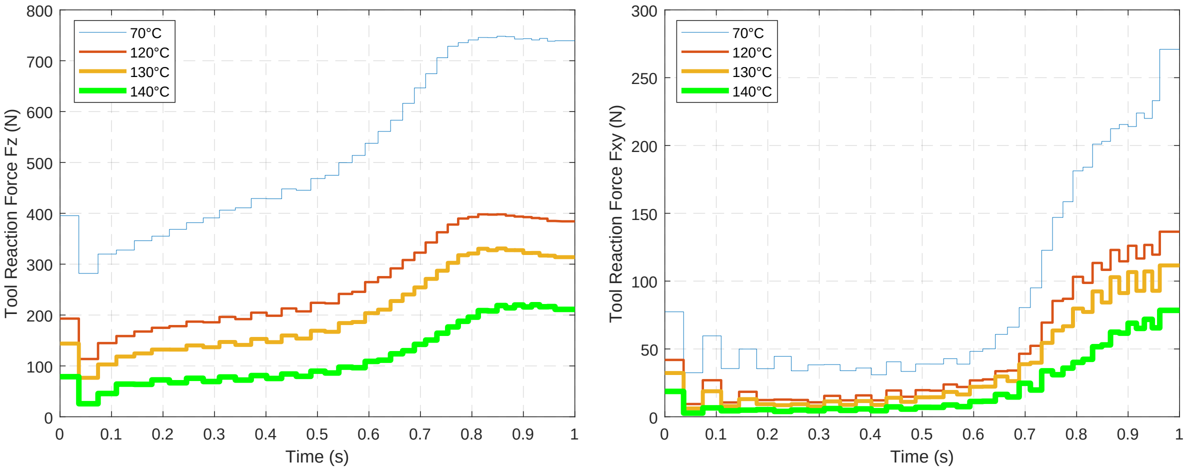

(a) Fz (b) F_R

Figure 4.24: Effect of temperature on the tool reaction forces F_Z and F_R

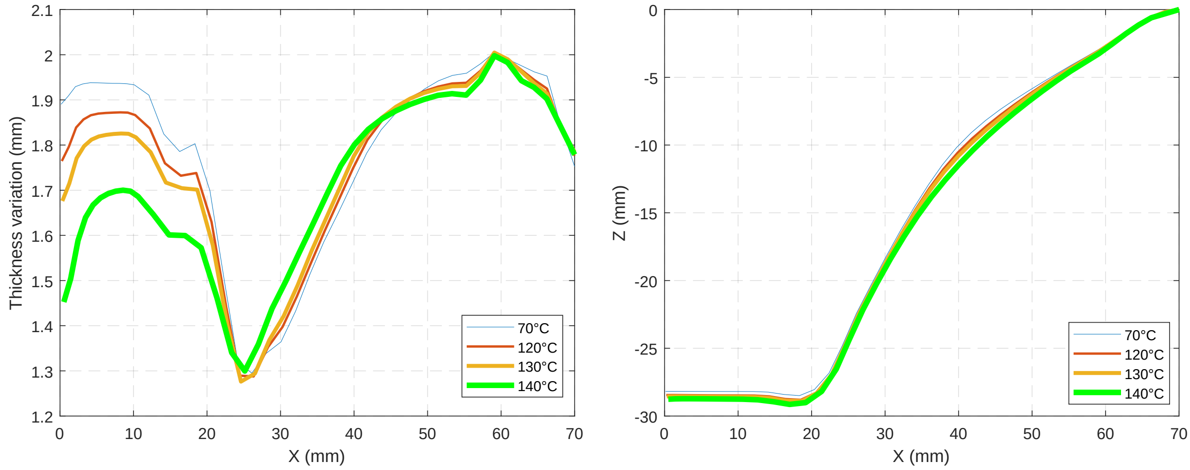

(a) Thickness variation (b) Final form

Figure 4.25: Effect of temperature on the thickness variation and final form of the part

In conclusion, the parametric study on a quarter of the model indicates that the simulation forming outcomes, particularly forming forces and thickness variation, are significantly influenced by temperature and the choice of the behavior law or calibration strategy for model parameters. However, these factors do not impact the final shape of the part. Additionally, taking anisotropy into account notably affects the forming force.

The next section consists in performing a numerical simulation of the forming operation and comparing the simulation outcomes with the experimental data.

4.6.5 Comparison with experimental results

In this section, the experimental spiral trajectory (Figure 4.10) is implemented in the numerical simulations to predict the forces required to form the entire sheet. The FE model of the plate is presented in Figure 4.26. The plate is clamped at the edges and the tool trajectory is attributed to the reference point located at the center of the hemispherical tool. The latter is considered as a rigid element, whereas the plate is meshed with 4061 linear quadrilateral elements of S4R type. Concerning the material model, the behavior law identified in Chapter 3 from the in-plane biaxial tensile tests (combined with Hill anisotropic criterion) is kept.

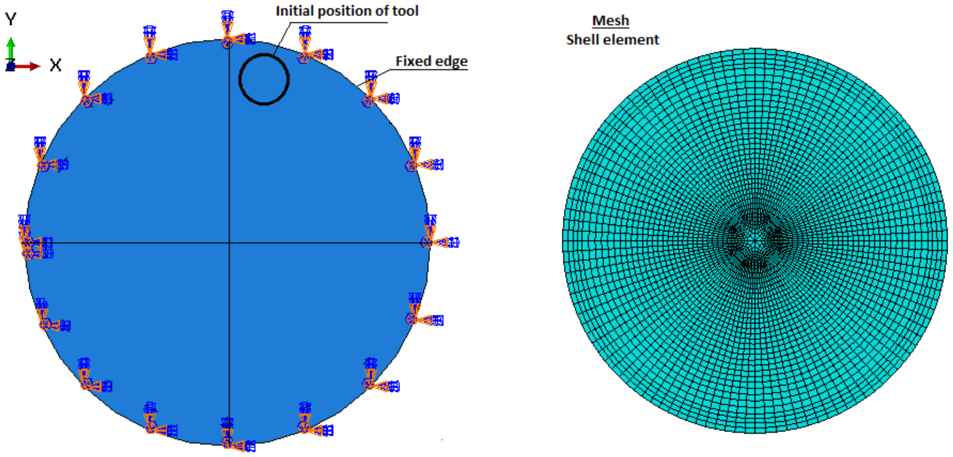

Figure 4.26: FE model of the experimental HAISF forming operation

4.6.5.1 Forces

As a reminder, the experimental forming operation took place when the plate reached a temperature of approximately 135-140°C. For the purpose of comparison between the simulated and experimental results, three constant temperatures are selected for the FE simulations: T=130°C, T=135°C and T=140°C. Figure 4.27 shows the evolution (with respect to time and tool displacement) of the axial force obtained from the simulations at the three mentioned temperatures. The experimental curve is represented by the starred line. The latter is located within the simulated force curves at T=130°C and T=135°C. The simulation at T=140°C obviously underestimates the rigidity of the material. A potential drop in the surface temperatures may have occurred at the sudden removal of the outlet hot air pipe, followed by the contact with the tool which was clearly at a lower temperature than the initial one of the plate. Moreover, the experimental force curve exhibits a noticeable drop in force towards the end of the forming process, which corresponds to fracture of the material. In contrast, the numerical simulations, which lacks a damage criterion, displays a progressive increase in force.

Relying on the parametric study conducted earlier, applying an isotropic von Mises criterion will overestimate the force and increase the gap between experimental and numerical forces. This makes the choice of Hill48 as a plasticity criterion a relatively good representation for the anisotropic behavior of the material. Also, a simulation at the same temperature but in conjunction with the behavior law identified from the uniaxial tensile tests will not give good prediction of the forming force. The law identified from the in-plane biaxial tensile test results is more adapted in this case since similar strain states are encountered in both applications. Therefore, the G'Sell and Jonas model calibrated from in-plane biaxial tensile test database coupled with Hill48 anisotropy can fairly predict the forming force. Incorporating a damage model into the FE simulations contributes to more accurate representation of the actual forming forces.

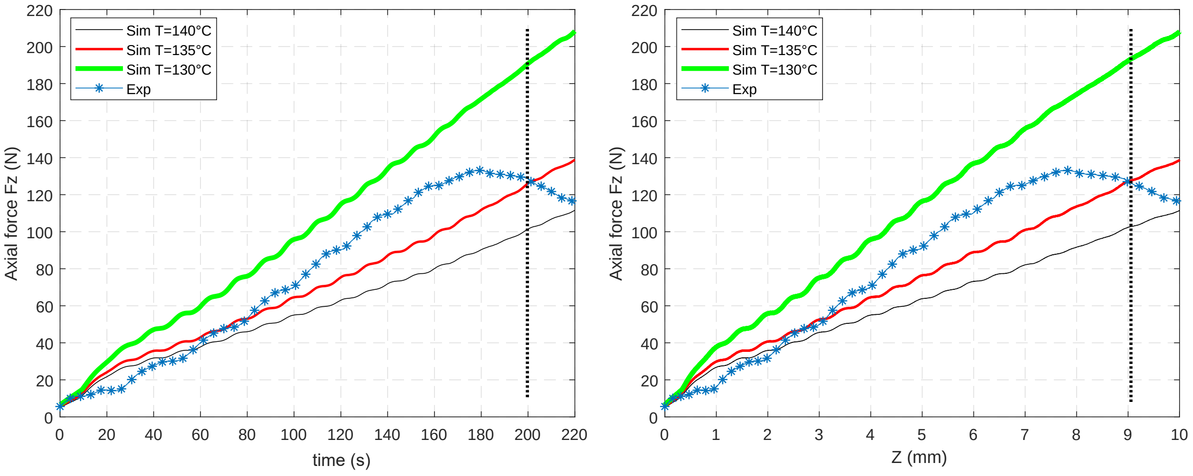

(a) Axial tool force Fz with respect to time (b) Axial tool force Fz with respect to Z

Figure 4.27: Axial tool force: Comparison between experimental and simulations performed at different temperatures (130, 135 and 140 °C)

4.6.5.2 Profiles

It was shown earlier that the simulated profile is not affected by neither the temperature nor the behavior law. Therefore, the simulation result for T=135°C using the model calibrated from the in-plane biaxial tests database (coupled with Hill48) is considered for the comparison with the experimental measurements. Figure 4.28 shows the simulated and experimental profiles. A small discrepancy is observed where the diameter of the simulated cone is slightly larger than the measured one, for each depth increment. For instance, at a forming depth of -5mm, a gap of (11%) is calculated, relative to the experimental profiles. The discrepancy can be attributed to many potential factors. Inaccurate modeling of the springback in the simulation is considered as a principle cause. In the present case, the simulation results overestimates the final geometry and dimensions of the formed part. Moreover, the possibility of uneven heating across the part usually affects the formability of the part resulting in unexpected outcomes in terms of the final shape and depth. This factor is not regarded in the simulation, leading to the inconsistency between the results. Additionally, the real friction between the tool and the part, as well as lubrication, is not perfectly addressed in the simulation conditions. Also, tolerances and precision of the robot arm may introduce slight variations in the final shape. However, it can be noted that the disparities observed are relatively minor. These differences are considered acceptable, especially considering the use of a simplified FE model and an experimental

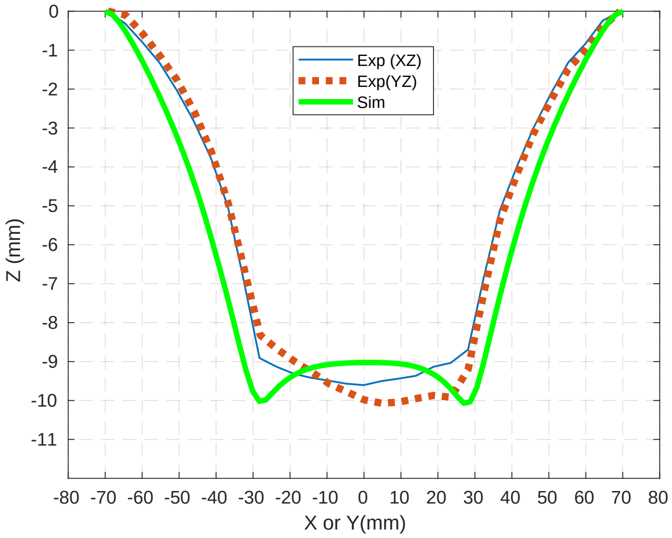

Figure 4.28: Comparison between the final shape obtained experimentally and the one obtained from simulation at T=135°C

setup, which represents a preliminary attempt in the incremental hot forming of this particular material.

4.6.5.3 Forming limits

Considering the simulation results at a temperature of T=135°C, Figures 4.29a and 4.29b illustrates the displacement and the thickness variation fields. Based on the simulation, the thickness of the formed cone varies between a minimum value of 1.86mm and a maximum of 2mm. However, in the scope of this study, experimental measurements of this particular parameter were not conducted.

Figure 4.29c and Figure 4.29d display the distribution of the maximum principle strain, equivalent plastic strain at the end of forming (step time t=200 s), respectively. At a depth of approximately 9 mm, the maximum principal strain reaches a value of 19%, whereas the equivalent plastic strain achieves 26%. The strain levels achieved at the end of the forming process closely align with those obtained in the in-plane biaxial tensile tests on cruciform specimens at T=135°C (refering to the results of Chapter 3). This similarity is attributed to the biaxial loading conditions experienced in both scenarios. The strain states and levels obtained during the forming process are comparable to those reached in the central zone of the cruciform specimen.

4.7 Conclusion

In conclusion, this chapter focused on the subject of HAISF of a 40% glass fiber reinforced polypropylene plate, building upon the phenomenological constitutive material behavior model established in the preceding chapters.

A parametric study was performed numerically (FE simulations on 1/4 of a forming model) to explore the impact of both the behavior law and temperature on the forming behavior. Notably, the material exhibited remarkable sensitivity to alterations in the behavior law and temperature, which was clearly demonstrated through clear changes in forming force and thickness variation.

Finally a FE model was established and configured to obtain a relatively close representation of the experimental setup including considerations for the entire plate rather than just a quarter. The investigation extended to a range of temperatures, allowing for a careful assessment of the degree of alignment between the simulated results and the empirical findings. The simulated results at T=135°C showed a fair correlation with the experimen-

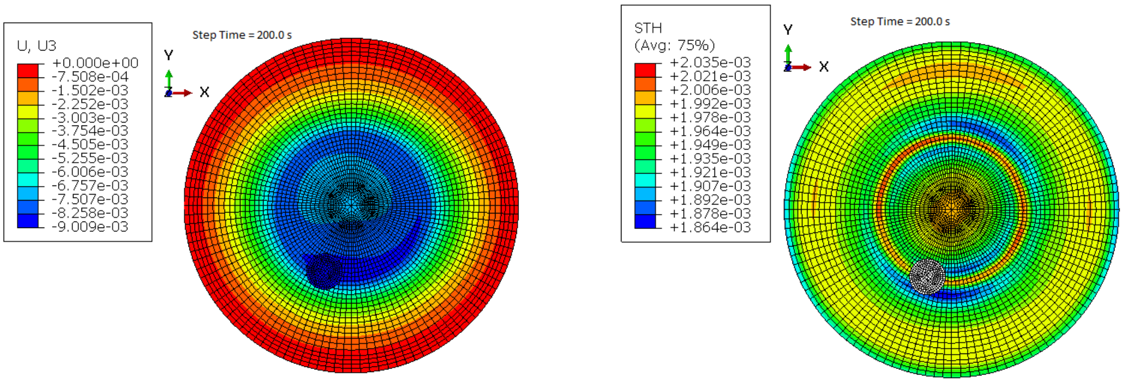

(a) Displacement field along Z axis (b) Thickness variation field

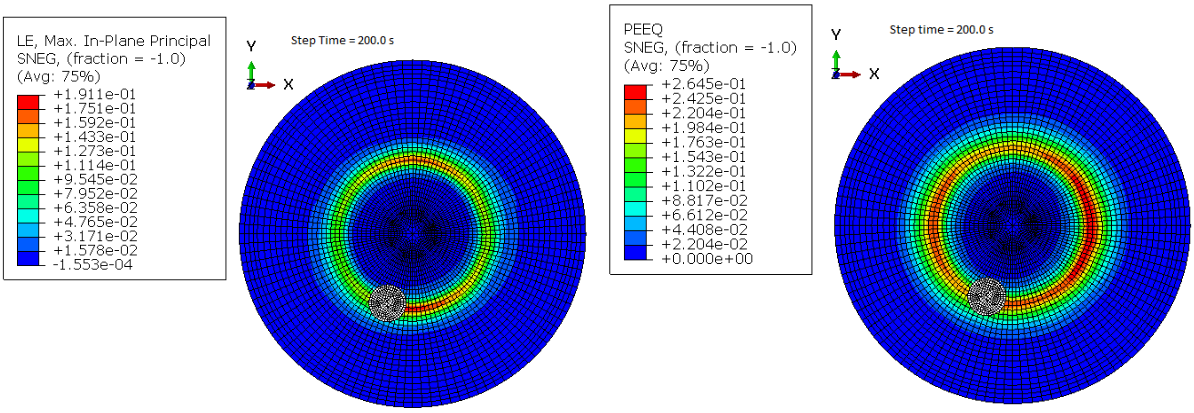

(c) Maximum principle strain field (d) Equivalent plastic strain field

Figure 4.29: Displacement, maximum principle strain and equivalent plastic strain fields at T=135°C.

tal measurements, knowing that the unaccurate modeling of springback, the absence of a damage criterion, along with other simplifying assumptions caused the observed deviation in the results.

From another point of view, it was clear that the behavior law derived from in-plane biaxial tensile tests offered a more accurate representation of the forming behavior, outperforming the behavior law derived from uniaxial tests. This can be attributed to the similarity in the strain states and levels experienced by the material during both scenarios.

CONCLUSION AND PERSPECTIVES

The main objective of this work was to conduct a comprehensive investigation of the mechanical behavior of glass fiber reinforced polypropylene under various conditions of temperatures and strain rates, resulting in the evaluation of its performance in heat-assisted incremental sheet forming.

The main contributions of this work are summarized as follows:

- The tensile properties of the studied material are sensitive to temperature and strain rate. The strain rate effect becomes less pronounced at high temperatures. The G'Sell and Jonas model, adapted to account for temperature and strain rate effects within the scope of this study, succeeded in predicting the mechanical behavior of glass fiber reinforced polypropylene. The calibration of the model parameters was performed using the experimental database, alongside the examination of material anisotropy through uniaxial tests along various orientations.

- By using a dedicated cruciform specimen, the biaxial testing machine equipped with an air flow generator successfully measured the tensile forces and strain fields within the central region of the specimen at various temperatures, ranging from 20°C to 140°C, and tensile velocities of 0.1mm/s and 10mm/s (corresponding to strain rates ranging between quasi-static up to 1/s).

- Apart from the identification of the parameters from the uniaxial tensile tests, two optimization strategies were tested: either a calibration based on both uniaxial and biaxial test results or a calibration that regards the biaxial results only. Depending on the strategy chosen, simulating the process with different parameters affects the forming outcomes.

- Building upon the established phenomenological constitutive model, FE simulations are employed to gain insights into the forming process. The HAISF was implemented experimentally to form a truncated cone from a flat glass fiber reinforced polypropylene sheet. A hot air heating system was included in the setup to heat the sheet prior to forming up to an approximate forming temperature of 135-140 °C. Instead of a traditional CNC machine, the forming tool was operated by a robot arm. This forming operation provided the basis for numerical validation, highlighting the dependence of the process to the temperature and material modeling strategy. Simulated results (forming force and final form), aligned with the behavior law derived from biaxial tensile tests, offer a more accurate representation of the forming process than the behavior law derived from uniaxial tests.

Future perspectives are suggested as follows:

- The selected cruciform specimen, originally designed for metallic materials, may not be optimal for discontinuous fiber reinforced thermoplastics. This consideration arises due to the critical nature of material removal or milling in the central zone of the specimen for such materials. For this reason, other designs can be tested, for instance, those that does not require material removal.

- In the material model identified in this study, the representation of springback was not accurately captured. The model assumed a linear elastic unloading behavior for springback. However, it's important to note that the actual springback behavior for the studied material may differ from this assumption. Furthermore, it's worth noting that the model did not account for material damage as well, which explains the observed increase in the gap between the experimentally obtained forming force and the simulation results at the end of the forming stage. This gap is attributed to the reduction in force levels towards the end of forming due to potential material failure or damage, a factor that was not considered in the model.
  Modeling these factors can induce better prediction of the forming force and final geometry prediction during HAISF.

- In this study, a basic setup of Heat Assisted Incremental Sheet Forming was established as an initial approach to form glass fiber reinforced polypropylene. This forming technique shows promise and it could be interesting to contribute in the enhancement of this innovative process. The improvement involves addressing various aspects. Regarding heating, the method can be optimized to obtain more efficient and uniform heating throughout the part. For example, testing other techniques or even combining different heating systems as well as pre-heating the tool. Optimizing the heating time and improving temperature control during the process to maintain consistent temperatures are also important factors to consider.

- The present work was conducted on a synthetic fiber reinforced thermoplastic which is widely spread and has a moderate level of complexity compared to other materials. Bio-sourced material (ease of recycling) on the other hand can be interesting for this present investigation. These material exhibit more complex behaviors than synthetic materials. However, the in-plane biaxial test on cruciform specimen is a comprehensive technique capable of accurately characterizing challenging materials whose complexity might require a more advanced experimental database. With the in-plane biaxial tensile test on cruciform specimens, various strain paths can be imposed by varying the applied displacement ratios. This allows for a more extensive examination of the material's response to different loading scenarios.

BIBLIOGRAPHY

[1] J. Bachmann, C. Hidalgo, and S. Bricout, “Environmental analysis of innovative sustainable composites with potential use in aviation sector—a life cycle assessment review”, *Science China Technological Sciences*, vol. 60, *9*, pp. 1301–1317, 2017.

[2] N. M. Aly, “A review on utilization of textile composites in transportation towards sustainability”, *in IOP Conference Series: Materials Science and Engineering*, IOP Publishing, vol. 254, 2017, p. 042 002.

[3] A. K. Sharma, R. Bhandari, A. Aherwar, and R. Rimašauskienė, “Matrix materials used in composites: a comprehensive study”, *Materials Today: Proceedings*, vol. 21, pp. 1559–1562, 2020.

[4] P. D. Pastuszak and A. Muc, “Application of composite materials in modern constructions”, *in Key Engineering Materials*, Trans Tech Publ, vol. 542, 2013, pp. 119–129.

[5] P. Mallick, “Thermoplastics and thermoplastic–matrix composites for lightweight automotive structures”, *in Materials, design and manufacturing for lightweight vehicles*, Elsevier, 2021, pp. 187–228.

[6] J. S. Chohan, K. S. Boparai, R. Singh, and M. Hashmi, “Manufacturing techniques and applications of polymer matrix composites: a brief review”, *Advances in Materials and Processing Technologies*, vol. 8, *1*, pp. 884–894, 2022.

[7] E. Morici and N. T. Dintcheva, “Recycling of thermoset materials and thermoset-based composites: challenge and opportunity”, *Polymers*, vol. 14, *19*, p. 4153, 2022.

[8] W. Ferdous, A. Manalo, P. Yu, C. Salih, R. Abousnina, T. Heyer, and P. Schubel, “Tensile fatigue behavior of polyester and vinyl ester based gfrp laminates—a comparative evaluation”, *Polymers*, vol. 13, *3*, p. 386, 2021.

[9] J. M. Khare, S. Dahiya, B. Gangil, L. Ranakoti, S. Sharma, M. R. M. Huzaifah, R. A. Ilyas, S. P. Dwivedi, S. Chattopadhyaya, H. C. Kilinc, *et al.*, “Comparative analysis of erosive wear behaviour of epoxy, polyester and vinyl esters based thermosetting polymer composites for human prosthetic applications using taguchi design”, *Polymers*, vol. 13, *20*, p. 3607, 2021.

[10] I. S. Abbood, S. aldeen Odaa, K. F. Hasan, and M. A. Jasim, “Properties evaluation of fiber reinforced polymers and their constituent materials used in structures - a review”, *Materials Today: Proceedings*, vol. 43, pp. 1003–1008, 2021.

[11] B. A. Alshammari, M. S. Alsuhybani, A. M. Almushaikeh, B. M. Alotaibi, A. M. Alenad, N. B. Alqahtani, and A. G. Alharbi, “Comprehensive review of the properties and modifications of carbon fiber-reinforced thermoplastic composites”, *Polymers*, vol. 13, *15*, p. 2474, 2021.

[12] R. Stewart, “Thermoplastic composites—recyclable and fast to process”, *Reinforced Plastics*, vol. 55, *3*, pp. 22–28, 2011.

[13] R. Weiss, “Fabrication techniques for thermoplastic composites”, *Cryogenics*, vol. 31, *4*, pp. 319–322, 1991.

[14] D. Mathijsen, “Leading the way in thermoplastic composites”, *Reinforced Plastics*, vol. 60, *6*, pp. 405–407, 2016.

[15] *Thermoplastic composites market size and forecast*, 2023. [Online]. Available: `https://www.verifiedmarketresearch.com/product/thermoplastic-composites-market/`.

[16] H. Ning, N. Lu, A. A. Hassen, K. Chawla, M. Selim, and S. Pillay, “A review of long fibre thermoplastic (lft) composites”, *International Materials Reviews*, vol. 65, *3*, pp. 164–188, 2020.

[17] D. Vaes and P. Van Puyvelde, “Semi-crystalline feedstock for filament-based 3d printing of polymers”, *Progress in Polymer Science*, vol. 118, p. 101 411, 2021.

[18] M. Abasalizadeh, R. Hasanzadeh, Z. Mohamadian, T. Azdast, and M. Rostami, “Experimental study to optimize shrinkage behavior of semi-crystalline and amorphous thermoplastics”, *Iran. J. Mater. Sci. Eng*, vol. 15, pp. 41–51, 2018.

[19] *Thermoplastics*, 2014. [Online]. Available: `https://polymers.com.au/thermoplastics/`.

[20] N. Billon and J.-L. Bouvard, *Propriétés et comportement mécanique des polymères thermoplastiques*, 2015.

[21] M. Nasraoui, P. Forquin, L. Siad, and A. Rusinek, “Influence of strain rate, temperature and adiabatic heating on the mechanical behaviour of poly-methyl-methacrylate: experimental and modelling analyses”, *Materials & Design*, vol. 37, pp. 500–509, 2012.

[22] O. Atmani, F. Abbès, Y. Li, S. Batkam, and B. Abbès, “Experimental investigation and constitutive modelling of the deformation behaviour of high impact polystyrene for plug-assisted thermoforming”, *Mechanics & Industry*, vol. 21, *6*, p. 607, 2020.

[23] Z. Wang, Y. Zhou, and P. Mallick, “Effects of temperature and strain rate on the tensile behavior of short fiber reinforced polyamide-6”, *Polymer Composites*, vol. 23, *5*, pp. 858–871, 2002.

[24] S. Duan, F. Mo, X. Yang, Y. Tao, D. Wu, and Y. Peng, “Experimental and numerical investigations of strain rate effects on mechanical properties of lgfrp composite”, *Composites Part B: Engineering*, vol. 88, pp. 101–107, 2016.

[25] J. Cui, S. Wang, S. Wang, G. Li, P. Wang, and C. Liang, “The effects of strain rates on mechanical properties and failure behavior of long glass fiber reinforced thermoplastic composites”, *Polymers*, vol. 11, *12*, p. 2019, 2019.

[26] L. Yu and Y. Ma, “Loading rate and temperature dependence of flexural behavior in injection-molded glass fiber reinforced polypropylene composites”, *Composites Part B: Engineering*, vol. 161, pp. 285–299, 2019.

[27] J. Thomason, “The influence of fibre length and concentration on the properties of glass fibre reinforced polypropylene. 6. the properties of injection moulded long fibre pp at high fibre content”, *Composites Part A: Applied Science and Manufacturing*, vol. 36, *7*, pp. 995–1003, 2005.

[28] M. Rabbi, T. Islam, and G. S. Islam, “Injection-molded natural fiber-reinforced polymer composites–a review”, *International Journal of Mechanical and Materials Engineering*, vol. 16, pp. 1–21, 2021.

[29] C. Bonten and E. Haberstroh, “Processing of plastics into structural components”, 2012.

[30] S.-J. Liu, “Injection molding in polymer matrix composites”, *in Manufacturing techniques for polymer matrix composites (PMCs)*, Elsevier, 2012, pp. 15–46.

[31] Y. Song, U. Gandhi, T. Sekito, U. K. Vaidya, S. Vallury, A. Yang, and T. Osswald, “Cae method for compression molding of carbon fiber-reinforced thermoplastic composite using bulk materials”, *Composites Part A: Applied Science and Manufacturing*, vol. 114, pp. 388–397, 2018.

[32] J. Sherwood, K. Fetfatsidis, J. Gorczyca, and L. Berger, “Fabric thermostamping in polymer matrix composites”, *in Manufacturing Techniques for Polymer Matrix Composites (PMCs)*, Elsevier, 2012, pp. 139–181.

[33] U. Sachs, *Friction and bending in thermoplasctic composites forming processes.* University of Twente Enschede, Netherlands, 2014.

[34] X. Xiao, J.-J. Kim, M.-P. Hong, S. Yang, and Y.-S. Kim, "Rsm and bpnn modeling in incremental sheet forming process for aa5052 sheet: multi-objective optimization using genetic algorithm", *Metals*, vol. 10, *8*, p. 1003, 2020.

[35] E. Ghossein and M. Lévesque, "A comprehensive validation of analytical homogenization models: the case of ellipsoidal particles reinforced composites", *Mechanics of Materials*, vol. 75, pp. 135–150, 2014.

[36] R. M. Jones, *Mechanics of composite materials.* CRC press, 2018.

[37] P. Joseph, G. Mathew, K. Joseph, S. Thomas, and P. Pradeep, "Mechanical properties of short sisal fiber-reinforced polypropylene composites: comparison of experimental data with theoretical predictions", *Journal of Applied Polymer Science*, vol. 88, *3*, pp. 602–611, 2003.

[38] J. Ashton, J. C. Halpin, and P. H. Petit, "Primer on composite materials: analysis", *(No Title)*, 1969.

[39] J. Halpin, "Stiffness and expansion estimates for oriented short fiber composites", *Journal of composite materials*, vol. 3, *4*, pp. 732–734, 1969.

[40] M. Loos, "Fundamentals of polymer matrix composites containing cnts", *Carbon nanotube reinforced composites*, pp. 125–170, 2015.

[41] E. Osoka and O. Onukwuli, "A modified halpin-tsai model for estimating the modulus of natural fiber reinforced composites", *Int. J. Eng. Sci. Invent*, vol. 7, *5*, pp. 63–70, 2018.

[42] Y. Benveniste, "A new approach to the application of mori-tanaka's theory in composite materials", *Mechanics of materials*, vol. 6, *2*, pp. 147–157, 1987.

[43] T. Mori and K. Tanaka, "Average stress in matrix and average elastic energy of materials with misfitting inclusions", *Acta metallurgica*, vol. 21, *5*, pp. 571–574, 1973.

[44] J. D. Eshelby, "The determination of the elastic field of an ellipsoidal inclusion, and related problems", *Proceedings of the royal society of London. Series A. Mathematical and physical sciences*, vol. 241, *1226*, pp. 376–396, 1957.

[45] P. R. Budarapu, X. Zhuang, T. Rabczuk, and S. P. Bordas, "Multiscale modeling of material failure: theory and computational methods", *Advances in applied mechanics*, vol. 52, pp. 1–103, 2019.

---

[46] M. Nachtane, F. Meraghni, G. Chatzigeorgiou, L. Harper, and F. Pelascini, “Multiscale viscoplastic modeling of recycled glass fiber-reinforced thermoplastic composites: experimental and numerical investigations”, *Composites Part B: Engineering*, vol. 242, p. 110 087, 2022.

[47] Z. M. Huang, “A unified micromechanical model for the mechanical properties of two constituent composite materials. part i: elastic behavior”, *Journal of Thermoplastic Composite Materials*, vol. 13, *4*, pp. 252–271, 2000.

[48] Z.-M. Huang, “Simulation of the mechanical properties of fibrous composites by the bridging micromechanics model”, *Composites Part A: applied science and manufacturing*, vol. 32, *2*, pp. 143–172, 2001.

[49] H.-B. Huang and Z.-M. Huang, “Micromechanical prediction of elastic-plastic behavior of a short fiber or particle reinforced composite”, *Composites Part A: Applied Science and Manufacturing*, vol. 134, p. 105 889, 2020.

[50] G. Carman and K. Reifsnider, “Micromechanics of short-fiber composites”, *Composites science and technology*, vol. 43, *2*, pp. 137–146, 1992.

[51] A. Meddad, J. Azaiez, A. Ait-Kadi, and R. Guenette, “Micromechanical modeling of tensile behavior of short fiber composites”, *Journal of composite materials*, vol. 36, *4*, pp. 423–441, 2002.

[52] J. Cha, H. Y. Song, K. Hyun, and J. S. Go, “Rheological measurement of the nonlinear viscoelasticity of the abs polymer and numerical simulation of thermoforming process”, *The International Journal of Advanced Manufacturing Technology*, vol. 107, pp. 2449–2464, 2020.

[53] X. Peng, H. Yin, J. Chen, and X. Liu, “A phenomenological thermal-mechanical viscoelastic constitutive modeling for polypropylene wood composites”, *Advances in Materials Science and Engineering*, vol. 2012, 2012.

[54] R. d. S. Escarpini Filho and S. P. C. Marques, “A model for homogenization of linear viscoelastic periodic composite materials with imperfect interface”, *Latin American Journal of Solids and Structures*, vol. 13, pp. 2706–2735, 2016.

[55] B. Chang, X. Wang, Z. Long, Z. Li, J. Gu, S. Ruan, and C. Shen, “Constitutive modeling for the accurate characterization of the tension behavior of peek under small strain”, *Polymer Testing*, vol. 69, pp. 514–521, 2018.

[56] J. Reis, L. Pacheco, and H. da Costa Mattos, “Influence of the temperature and strain rate on the tensile behavior of post-consumer recycled high-density polyethylene”, *Polymer testing*, vol. 32, *8*, pp. 1576–1581, 2013.

[57] J. Reis, F. Chaves, and H. da Costa Mattos, “Tensile behaviour of glass fibre reinforced polyurethane at different strain rates”, *Materials & Design*, vol. 49, pp. 192–196, 2013.

[58] M. Mooney, “A theory of large elastic deformation”, *Journal of applied physics*, vol. 11, *9*, pp. 582–592, 1940.

[59] R. S. Rivlin, “Large elastic deformations of isotropic materials iv. further developments of the general theory”, *Philosophical Transactions of the Royal Society of London. Series A, Mathematical and Physical Sciences*, vol. 241, *835*, pp. 379–397, 1948.

[60] X.-T. Pham, F. Thibault, and L.-T. Lim, “Modeling and simulation of stretch blow molding of polyethylene terephthalate”, *Polymer Engineering & Science*, vol. 44, *8*, pp. 1460–1472, 2004.

[61] X.-T. Pham, P. Bates, and A. Chesney, “Modeling of thermoforming of low-density glass mat thermoplastic”, *Journal of reinforced plastics and composites*, vol. 24, *3*, pp. 287–298, 2005.

[62] G. R. Cowper, P. S. Symonds, *et al.*, “Strain-hardening and strain-rate effects in the impact loading of cantilever beams”, 1957.

[63] S. Wang, Y. Yao, C. Tang, G. Li, and J. Cui, “Mechanical characteristics, constitutive models and fracture behaviors of short basalt fiber reinforced thermoplastic composites under varying strain rates”, *Composites Part B: Engineering*, vol. 218, p. 108 933, 2021.

[64] P. Ludwik, *Elemente der technologischen Mechanik*. Springer, 1909.

[65] E. Voce, “The relationship between stress and strain for homogeneous deformation”, *Journal of the Institute of Metals*, vol. 74, pp. 537–562, 1948.

[66] T. Gates and C. Sun, “Elastic/viscoplastic constitutive model for fiber reinforced thermoplastic composites”, *AIAA Journal*, vol. 29, *3*, pp. 457–463, 1991.

[67] C. Sun and J. Chen, “A simple flow rule for characterizing nonlinear behavior of fiber composites”, *Journal of Composite materials*, vol. 23, *10*, pp. 1009–1020, 1989.

[68] Y. Duan, A. Saigal, R. Greif, and M. Zimmerman, “A uniform phenomenological constitutive model for glassy and semicrystalline polymers”, *Polymer Engineering & Science*, vol. 41, *8*, pp. 1322–1328, 2001.

[69] N. Achour, G. Chatzigeorgiou, F. Meraghni, Y. Chemisky, and J. Fitoussi, “Implicit implementation and consistent tangent modulus of a viscoplastic model for

polymers”, *International Journal of Mechanical Sciences*, vol. 103, pp. 297–305, 2015.

[70] T. Deng, W. Zhang, W. Jiang, H. Zhou, Z. Huang, X. Peng, H. Zhou, and D. Li, “A hybrid lamination model for simulation of woven fabric reinforced thermoplastic composites solid-state thermo-stamping”, *Materials & Design*, vol. 200, p. 109 419, 2021.

[71] C. G’sell and J. Jonas, “Determination of the plastic behaviour of solid polymers at constant true strain rate”, *Journal of materials science*, vol. 14, *3*, pp. 583–591, 1979.

[72] M. Schoßig, C. Bierögel, W. Grellmann, and T. Mecklenburg, “Mechanical behavior of glass-fiber reinforced thermoplastic materials under high strain rates”, *Polymer testing*, vol. 27, *7*, pp. 893–900, 2008.

[73] D.-C. Trufasu, M.-A.-C. Besnea, G. Andrei, and D. Dima, “Parameters identification of mechanical behaviour law for polyether-ether-ketone composites.”, *Annals of DAAAM & Proceedings*, 2011.

[74] F. Irgens, *Continuum mechanics.* Springer Science & Business Media, 2008.

[75] P. H. Holmström, O. S. Hopperstad, and A. H. Clausen, “Anisotropic tensile behaviour of short glass-fibre reinforced polyamide-6”, *Composites Part C: Open Access*, vol. 2, p. 100 019, 2020.

[76] P. H. Holmström, A. H. Clausen, T. Berstad, D. Morin, and O. S. Hopperstad, “A pragmatic orthotropic elasticity-based damage model with spatially distributed properties applied to short glass-fibre reinforced polymers”, *International Journal of Solids and Structures*, vol. 230, p. 111 142, 2021.

[77] S. W. Tsai, *Strength characteristics of composite materials.* NASA Washington, DC, 1965.

[78] V. Azzi and S. W. Tsai, “Anisotropic strength of composites: investigation aimed at developing a theory applicable to laminated as well as unidirectional composites, employing simple material properties derived from unidirectional specimens alone”, *Experimental mechanics*, vol. 5, pp. 283–288, 1965.

[79] S. W. Tsai and E. M. Wu, “A general theory of strength for anisotropic materials”, *Journal of composite materials*, vol. 5, *1*, pp. 58–80, 1971.

[80] O. Hoffman, “The brittle strength of orthotropic materials”, *Journal of Composite materials*, vol. 1, *2*, pp. 200–206, 1967.

---

[81] R. Hill, “A theory of the yielding and plastic flow of anisotropic metals”, *Proceedings of the Royal Society of London. Series A. Mathematical and Physical Sciences*, vol. 193, *1033*, pp. 281–297, 1948.

[82] S. Mortazavian and A. Fatemi, “Effects of fiber orientation and anisotropy on tensile strength and elastic modulus of short fiber reinforced polymer composites”, *Composites part B: engineering*, vol. 72, pp. 116–129, 2015.

[83] J. Choi, H. Lee, H. Lee, and N. Kim, “A methodology to predict the fatigue life under multi-axial loading of carbon fiber-reinforced polymer composites considering anisotropic mechanical behavior”, *Materials*, vol. 16, *5*, p. 1952, 2023.

[84] B. Erice, D. Thomson, S. A. Ponnusami, M. V. Pathan, and N. Petrinic, “On the rate-dependent plasticity modelling of unidirectional fibre-reinforced polymeric matrix composites”, *in EPJ Web of Conferences*, EDP Sciences, vol. 183, 2018, p. 01 055.

[85] A. Merneedi, L. Natrayan, S. Kaliappan, D. Veeman, S. Angalaeswari, C. Srinivas, and P. Paramasivam, “Experimental investigation on mechanical properties of carbon nanotube-reinforced epoxy composites for automobile application”, *Journal of Nanomaterials*, vol. 2021, pp. 1–7, 2021.

[86] C. Röhrig, T. Scheffer, and S. Diebels, “Mechanical characterization of a short fiber-reinforced polymer at room temperature: experimental setups evaluated by an optical measurement system”, *Continuum Mechanics and Thermodynamics*, vol. 29, pp. 1093–1111, 2017.

[87] D. E. Walrath and D. F. Adams, “The losipescu shear test as applied to composite materials”, *Experimental mechanics*, vol. 23, pp. 105–110, 1983.

[88] M. Selezneva and L. Lessard, “Characterization of mechanical properties of randomly oriented strand thermoplastic composites”, *Journal of composite materials*, vol. 50, *20*, pp. 2833–2851, 2016.

[89] M. Y. Chiang and J. He, “An analytical assessment of using the losipescu shear test for hybrid composites”, *Composites Part B: Engineering*, vol. 33, *6*, pp. 461–470, 2002.

[90] Y. M. Tarnopol’skii, A. Arnautov, and V. Kulakov, “Methods of determination of shear properties of textile composites”, *Composites Part A: Applied Science and Manufacturing*, vol. 30, *7*, pp. 879–885, 1999.

[91] D. E. Weber, N. Graupner, and J. Müssig, “Manufacturing of flax-and glass-fibre reinforced thin-walled tubes and measuring their interlaminar shear properties by torsion tests”, *Composite Structures*, p. 117 191, 2023.

[92] G. Vallee and R. Short, “Design and development of an economical torsion testing machine”, *in Proceedings of the ASEE New England Section 2006 Annual Conference*, 2006.

[93] P. Wang, N. Hamila, P. Pineau, and P. Boisse, “Thermomechanical analysis of thermoplastic composite prepregs using bias-extension test”, *Journal of Thermoplastic Composite Materials*, vol. 27, *5*, pp. 679–698, 2014.

[94] D. Brands, S. Wijskamp, W. Grouve, and R. Akkerman, “In-plane shear characterization of unidirectional fiber reinforced thermoplastic tape using the bias extension method”, *Frontiers in Materials*, vol. 9, p. 863 952, 2022.

[95] Y. Nakashima, S. Yamashita, X. Zhang, H. Suganuma, and J. Takahashi, “Analytical modelling of the behaviour and scatter of the flexural modulus of randomly oriented carbon fibre strand thermoplastic composites”, *Composite Structures*, vol. 178, pp. 217–224, 2017.

[96] G. M. Munakaampe, S. B. Kanyanga, P. Myler, and C. G. Chizyuka, “Response of natural sisal reinforced polyester composites to three-point and four-point bending”, *Procedia Manufacturing*, vol. 7, pp. 327–332, 2017.

[97] C. Andriss, A. Kenf, T. Donhauser, and S. Schmeer, “Characterization and modeling of continuous carbon fiber-reinforced polycarbonate under multiaxial loads”, *Composites Part B: Engineering*, vol. 235, p. 109 740, 2022.

[98] S. Amijima, T. Fujii, and M. Hamaguchi, “Static and fatigue tests of a woven glass fabric composite under biaxial tension-torsion loading”, *Composites*, vol. 22, *4*, pp. 281–289, 1991.

[99] C. Lee, W. Hwang, H. Park, and K. Han, “Failure of carbon/epoxy composite tubes under combined axial and torsional loading 1. experimental results and prediction of biaxial strength by the use of neural networks”, *Composites Science and Technology*, vol. 59, *12*, pp. 1779–1788, 1999.

[100] D. Hitt and M. Gilbert, “A machine for the biaxial stretching of polymers”, *Polymer testing*, vol. 13, *3*, pp. 219–237, 1994.

[101] Z. Xie, G. Liao, J. Liu, B. Li, L. Cui, and Y. Liu, “Relaxation behavior of biaxially stretched pla film during the heat setting stage”, *Frontiers in Materials*, vol. 10, p. 1 241 104, 2023.

[102] S. Ouchiar, G. Stoclet, C. Cabaret, A. Addad, and V. Gloaguen, “Effect of biaxial stretching on thermomechanical properties of polylactide based nanocomposites”, *Polymer*, vol. 99, pp. 358–367, 2016.

[103] G. Ferron and A. Makinde, “Design and development of a biaxial strength testing device”, *Journal of testing and evaluation*, vol. 16, *3*, pp. 253–256, 1988.

[104] J. Boehler, S. Demmerle, and S. Koss, “A new direct biaxial testing machine for anisotropic materials”, *Experimental mechanics*, vol. 34, pp. 1–9, 1994.

[105] A. Makinde, L. Thibodeau, and K. Neale, “Development of an apparatus for biaxial testing using cruciform specimens”, *Experimental mechanics*, vol. 32, pp. 138–144, 1992.

[106] J. Chen, J. Zhang, and H. Zhao, “Development and experimental verification of a high-temperature and in-plane biaxial testing apparatus”, *Machines*, vol. 10, *11*, p. 1054, 2022.

[107] S. Demmerle and J. Boehler, “Optimal design of biaxial tensile cruciform specimens”, *Journal of the Mechanics and Physics of Solids*, vol. 41, *1*, pp. 143–181, 1993.

[108] Y. Ohtake, S. Sato, K. Hatanaka, H. Masumoto, and Y. Matsumura, “Biaxial deformation behaviors of c/c composite at high temperatures”, *JSME International Journal Series A Solid Mechanics and Material Engineering*, vol. 43, *4*, pp. 384–392, 2000.

[109] I. 16842, “Metallic materials-sheet and strip-biaxial tensile testing method using a cruciform test piece”, 2021.

[110] L. Nasdala and A. H. Husni, “Determination of yield surfaces in accordance with iso 16842 using an optimized cruciform test specimen”, *Experimental Mechanics*, vol. 60, *6*, pp. 815–832, 2020.

[111] I. Zidane, D. Guines, L. Leotoing, and E. Ragneau, “Development of an in-plane biaxial test for forming limit curve (flc) characterization of metallic sheets”, *Measurement Science and Technology*, vol. 21, *5*, p. 055 701, 2010.

[112] X. Song, L. Leotoing, D. Guines, and E. Ragneau, “Characterization of forming limits at fracture with an optimized cruciform specimen: application to dp600 steel sheets”, *International Journal of Mechanical Sciences*, vol. 126, pp. 35–43, 2017.

[113] R. Xiao, X.-X. Li, L.-H. Lang, Q. Song, and K.-N. Liu, “Forming limit in thermal cruciform biaxial tensile testing of titanium alloy”, *Journal of Materials Processing Technology*, vol. 240, pp. 354–361, 2017.

[114] N. Deng, T. Kuwabara, and Y. Korkolis, “Cruciform specimen design and verification for constitutive identification of anisotropic sheets”, *Experimental Mechanics*, vol. 55, pp. 1005–1022, 2015.

[115] W. Liu, D. Guines, L. Leotoing, and E. Ragneau, “Identification of sheet metal hardening for large strains with an in-plane biaxial tensile test and a dedicated cross specimen”, *International Journal of Mechanical Sciences*, vol. 101, pp. 387–398, 2015.

[116] W. Liu, D. Guines, L. Leotoing, and E. Ragneau, “Identification of strain rate-dependent mechanical behaviour of dp600 under in-plane biaxial loadings”, *Materials Science and Engineering: A*, vol. 676, pp. 366–376, 2016.

[117] J. S. Welsh and D. F. Adams, “An experimental investigation of the biaxial strength of im6/3501-6 carbon/epoxy cross-ply laminates using cruciform specimens”, *Composites Part A: Applied Science and Manufacturing*, vol. 33, *6*, pp. 829–839, 2002.

[118] D. Green, K. Neale, S. MacEwen, A. Makinde, and R. Perrin, “Experimental investigation of the biaxial behaviour of an aluminum sheet”, *International journal of plasticity*, vol. 20, *8-9*, pp. 1677–1706, 2004.

[119] A. Smits, D. Van Hemelrijck, T. Philippidis, and A. Cardon, “Design of a cruciform specimen for biaxial testing of fibre reinforced composite laminates”, *Composites science and technology*, vol. 66, *7-8*, pp. 964–975, 2006.

[120] P. Hopgood, J. Cook, and A. Clarke, “Multi-axial testing of planar composite specimens”, *in Proceedings of the 12th International Conference on Composite Materials, Paris, France*, 1999, pp. 5–9.

[121] A. Kobeissi, P. Rahme, L. Leotoing, and D. Guines, “Strength characterization of glass/epoxy plain weave composite under different biaxial loading ratios”, *Journal of Composite Materials*, vol. 54, *19*, pp. 2549–2563, 2020.

[122] J. Liang, D. Guines, and L. Leotoing, “Thermo-viscoplastic behavior of aa6061 under dynamic biaxial loadings”, *in AIP Conference Proceedings*, AIP Publishing, vol. 2113, 2019.

[123] H. Lau, S. Bhattacharya, and G. Field, “Melt strength of polypropylene: its relevance to thermoforming”, *Polymer Engineering & Science*, vol. 38, *11*, pp. 1915–1923, 1998.

[124] P. Martin, C. Tan, K. Tshai, R. McCool, G. Menary, C. Armstrong, and E. Harkin-Jones, “Biaxial characterisation of materials for thermoforming and blow moulding”, *Plastics, rubber and composites*, vol. 34, *5-6*, pp. 276–282, 2005.

[125] S. K. Alavi, M. Ayatollahi, J. Jamali, and M. Petru, “On the applicability of digital image correlation method in extracting the higher order terms in stress field around blunt notches”, *Theoretical and Applied Fracture Mechanics*, vol. 121, p. 103 436, 2022.

[126] R. Bigger, B. Blaysat, C. Boo, *et al.*, “A good practices guide for digital image correlation”, 2018.

[127] I. (O. for Standardization), *Plastics—determination of tensile properties—part 1: general principles, iso 527-1: 2019*, 2019.

[128] C. G’sell, N. Aly-Helal, and J. Jonas, “Effect of stress triaxiality on neck propagation during the tensile stretching of solid polymers”, *Journal of Materials Science*, vol. 18, *6*, pp. 1731–1742, 1983.

[129] B. Abbès, O. Zaki, and L. Safa, “Experimental and numerical study of the aging effects of sorption conditions on the mechanical behaviour of polypropylene bottles under columnar crush conditions”, *Polymer testing*, vol. 29, *7*, pp. 902–909, 2010.

[130] F. Abbès, N. G. Tran, B. Abbès, and Y.-Q. Guo, “Modelling of the degradation of mechanical properties of high-density polyethylene based-packaging exposed to amyl acetate solution”, *Polymer Testing*, vol. 59, pp. 449–461, 2017.

[131] G. Sala, L. Di Landro, and D. Cassago, “A numerical and experimental approach to optimise sheet stamping technologies: polymers thermoforming”, *Materials & design*, vol. 23, *1*, pp. 21–39, 2002.

[132] O. Atmani, B. Abbès, F. Abbès, Y. Li, and S. Batkam, “Identification of a thermo-elasto-viscoplastic behavior law for the simulation of thermoforming of high impact polystyrene”, *in AIP Conference Proceedings*, AIP Publishing, vol. 1960, 2018.

[133] N. A. Rahman, A. Hassan, R. Yahya, and R. Lafia-Araga, “Impact properties of glass-fiber/polypropylene composites: the influence of fiber loading, specimen geometry and test temperature”, *Fibers and Polymers*, vol. 14, pp. 1877–1885, 2013.

[134] J. Thomason and L. Yang, “Temperature dependence of the interfacial shear strength in glass–fibre polypropylene composites”, *Composites Science and Technology*, vol. 71, *13*, pp. 1600–1605, 2011.

[135] T. B. Van Erp, C. T. Reynolds, T. Peijs, J. A. Van Dommelen, and L. E. Govaert, “Prediction of yield and long-term failure of oriented polypropylene: kinetics and anisotropy”, *Journal of Polymer Science Part B: Polymer Physics*, vol. 47, *20*, pp. 2026–2035, 2009.

[136] M. Abida, J. Mars, F. Gehring, A. Vivet, and F. Dammak, “Anisotropic visco-elastoplastic modeling of quasi-unidirectional flax fiber reinforced epoxy behavior: an investigation on low-velocity impact response”, *Journal of Renewable Materials*, vol. 6, *5*, pp. 464–476, 2018.

[137] A. Amiri-Rad, L. Pastukhov, L. Govaert, and J. Van Dommelen, “An anisotropic viscoelastic-viscoplastic model for short-fiber composites”, *Mechanics of Materials*, vol. 137, p. 103 141, 2019.

[138] A. Amiri-Rad, M. Wismans, L. V. Pastukhov, L. E. Govaert, and J. A. van Dommelen, “Constitutive modeling of injection-molded short-fiber composites: characterization and model application”, *Journal of Applied Polymer Science*, vol. 137, *41*, p. 49 248, 2020.

[139] R. K. Joki, F. Grytten, and H. Osnes, “Coupling of plasticity and damage in glass fibre reinforced polymer composites”, *in EPJ Web of Conferences*, EDP Sciences, vol. 26, 2012, p. 04 028.

[140] L. Pastukhov and L. Govaert, “Plasticity-controlled failure of fibre-reinforced thermoplastics”, *Composites Part B: Engineering*, vol. 209, p. 108 635, 2021.

[141] L. Jiabin, G. Dominique, and L. Lionel, “Effect of temperature and strain rate on the plastic anisotropic behavior characterized by a single biaxial tensile test”, *Procedia Manufacturing*, vol. 47, pp. 1532–1539, 2020.

[142] S. Hartmann, R. R. Gilbert, and C. Sguazzo, “Basic studies in biaxial tensile tests”, *GAMM-Mitteilungen*, vol. 41, *1*, e201800004, 2018.

[143] S. Zhang, L. Leotoing, D. Guines, and S. Thuillier, “Potential of the cross biaxial test for anisotropy characterization based on heterogeneous strain field”, *Experimental Mechanics*, vol. 55, pp. 817–835, 2015.

[144] J. Liang, H. Xinhai, and T. Wenlong, “Micro-mechanical model for predicting the elasto-plastic behavior of composites based on secant formulation method”, *Chinese Journal of Aeronautics*, vol. 34, *1*, pp. 281–295, 2021.

[145] Y. Li, W. Shi, J. Li, C. Yang, T. Xia, X. Sheng, and X. Wang, “Structure and properties of glass fiber reinforced polypropylene/liquid crystal polymer blends”, *Journal of Macromolecular Science, Part B*, vol. 54, *9*, pp. 1144–1152, 2015.

[146] D. Zhang, M. He, H. Luo, S. Qin, J. Yu, and J. Guo, “Performance of long glass fiber-reinforced polypropylene composites at different injection temperature”, *Journal of Vinyl and Additive Technology*, vol. 24, *3*, pp. 233–238, 2018.

[147] F. Bre and V. D. Fachinotti, “A computational multi-objective optimization method to improve energy efficiency and thermal comfort in dwellings”, *Energy and Buildings*, vol. 154, pp. 283–294, 2017.

[148] V. Reddy, R. Lingam, and J. Cao, “Incremental metal forming processes in manufacturing”, *in Handbook of manufacturing engineering and technology*, Springer-Verlag London Ltd, 2015, pp. 411–452.

[149] J.-J. Park and Y.-H. Kim, “Fundamental studies on the incremental sheet metal forming technique”, *Journal of Materials Processing Technology*, vol. 140, *1-3*, pp. 447–453, 2003.

[150] G. Ambrogio, L. De Napoli, L. Filice, F. Gagliardi, and M. Muzzupappa, “Application of incremental forming process for high customised medical product manufacturing”, *Journal of materials processing technology*, vol. 162, pp. 156–162, 2005.

[151] L. Sevsek and T. Pepelnjak, “The review of the achievements in the field of incremental forming”, *Res. & Sci. Today*, vol. 17, p. 124, 2019.

[152] J. Jeswiet, F. Micari, G. Hirt, A. Bramley, J. Duflou, and J. Allwood, “Asymmetric single point incremental forming of sheet metal”, *CIRP annals*, vol. 54, *2*, pp. 88–114, 2005.

[153] A. Brosius, “Incremental forming”, *CIRP Encyclopedia of Production Engineering*, pp. 689–692, 2014.

[154] G. Medina-Sanchez, A. Garcia-Collado, D. Carou, and R. Dorado-Vicente, “Force prediction for incremental forming of polymer sheets”, *Materials*, vol. 11, *9*, p. 1597, 2018.

[155] J. Kopac and Z. Kampus, “Incremental sheet metal forming on cnc milling machine-tool”, *Journal of materials processing technology*, vol. 162, pp. 622–628, 2005.

[156] J. Belchior, “Développement d’une approche couplée matériau/structure machine: application au formage incrémental robotisé”, Ph.D. dissertation, INSA de Rennes, 2013.

[157] R. P. Singh, S. K. Gupta, P. K. Singh, and S. Kumar, “Robot assisted incremental sheet forming of al6061 under static pressure: preliminary study of thickness distribution within the deformation region”, *Materials Today: Proceedings*, vol. 47, pp. 2737–2741, 2021.

[158] R. Ortiz-Hernandez, N. A. Ulloa-Castillo, J. M. Diabb-Zavala, A. Estrada-De La Vega, J. Islas-Urbano, J. Villela-Castrejon, and A. Elias-Zuniga, “Advances in the

processing of uhmwpe-tio2 to manufacture medical prostheses via spif", *Polymers*, vol. 11, *12*, p. 2022, 2019.

[159] H. Wang, S. Zheng, H. Luo, G. Wei, X. Guo, A. Abd El-Aty, Y. Gu, and K. Guang, "Flexible incremental sheet metal forming technology", *in Flexible Metal Forming Technologies: Principles, Process and Equipment*, Springer, 2022, pp. 29–77.

[160] L. Fratini, G. Ambrogio, R. Di Lorenzo, L. Filice, and F. Micari, "Influence of mechanical properties of the sheet material on formability in single point incremental forming", *CIRP Annals*, vol. 53, *1*, pp. 207–210, 2004.

[161] T. Trzepieciński, S. M. Najm, V. Oleksik, D. Vasilca, I. Paniti, and M. Szpunar, "Recent developments and future challenges in incremental sheet forming of aluminium and aluminium alloy sheets", *Metals*, vol. 12, *1*, p. 124, 2022.

[162] M. Amino, M. Mizoguchi, Y. Terauchi, and T. Maki, "Current status of "dieless" amino's incremental forming", *Procedia Engineering*, vol. 81, pp. 54–62, 2014.

[163] Z. Cheng, Y. Li, C. Xu, Y. Liu, S. Ghafoor, and F. Li, "Incremental sheet forming towards biomedical implants: a review", *Journal of Materials Research and Technology*, vol. 9, *4*, pp. 7225–7251, 2020.

[164] V. Franzen, L. Kwiatkowski, J. Neves, P. Martins, and A. Tekkaya, "On the capability of single point incremental forming for manufacturing polymer sheet parts", *in ICTP2008, 9th International Conference on Theory of Plasticity*, 2008.

[165] H. Zhu, H. Ou, and A. Popov, "Incremental sheet forming of thermoplastics: a review", *The International Journal of Advanced Manufacturing Technology*, vol. 111, pp. 565–587, 2020.

[166] Z. Liu, "Heat-assisted incremental sheet forming: a state-of-the-art review", *The International Journal of Advanced Manufacturing Technology*, vol. 98, *9-12*, pp. 2987–3003, 2018.

[167] W. Li, M. M. Attallah, and K. Essa, "Heat-assisted incremental sheet forming for high-strength materials—a review", *The International Journal of Advanced Manufacturing Technology*, vol. 124, *7-8*, pp. 2011–2036, 2023.

[168] G. Ambrogio, R. Conte, F. Gagliardi, L. De Napoli, L. Filice, and P. Russo, "A new approach for forming polymeric composite structures", *Composite Structures*, vol. 204, pp. 445–453, 2018.

[169] R. Conte, G. Ambrogio, D. Pulice, F. Gagliardi, and L. Filice, "Incremental sheet forming of a composite made of thermoplastic matrix and glass-fiber reinforcement", *Procedia engineering*, vol. 207, pp. 819–824, 2017.

[170] A.-O. Amar, A. Graf, V. Kräusel, and M. Trautmann, "Heat supported single point incremental forming of hybrid laminates for orthopedic applications", *Procedia Manufacturing*, vol. 29, pp. 21–27, 2019.

[171] A.-O. Amar, A. Kunke, and V. Kräusel, "Hot single-point incremental forming of glass-fiber-reinforced polymer (pa6gf47) supported by hot air", *Journal of Manufacturing Processes*, vol. 43, pp. 17–25, 2019.

[172] M. Okada, T. Kato, M. Otsu, H. Tanaka, and T. Miura, "Development of optical-heating-assisted incremental forming method for carbon fiber reinforced thermoplastic sheet—forming characteristics in simple spot-forming and two-dimensional sheet-fed forming", *Journal of Materials Processing Technology*, vol. 256, pp. 145–153, 2018.

[173] M. Durante, A. Formisano, A. Langella, and F. M. C. Minutolo, "The influence of tool rotation on an incremental forming process", *Journal of Materials Processing Technology*, vol. 209, *9*, pp. 4621–4626, 2009.

[174] Z. Liu, "Friction stir incremental forming of aa7075-o sheets: investigation on process feasibility", *Procedia engineering*, vol. 207, pp. 783–788, 2017.

[175] L. Lozano-Sánchez, A. Sustaita, M. Soto, S. Biradar, L. Ge, E. Segura-Cárdenas, J. Diabb, L. Elizalde, E. Barrera, and A. Elías-Zúñiga, "Mechanical and structural studies on single point incremental forming of polypropylene-mwcnts composite sheets", *Journal of Materials Processing Technology*, vol. 242, pp. 218–227, 2017.

[176] R. Conte, F. Gagliardi, G. Ambrogio, F. Filice, and P. Russo, "Performance analysis of the incremental sheet forming on pmma using a combined chemical and mechanical approach", *in AIP Conference Proceedings*, AIP Publishing, vol. 1896, 2017.

[177] R. Conte, G. Serratore, G. Ambrogio, and F. Gagliardi, "Numerical analyses of long fiber–reinforced polymeric sheets processed by single point incremental forming", *The International Journal of Advanced Manufacturing Technology*, vol. 123, *3-4*, pp. 1203–1214, 2022.

[178] A. Kharche and S. Barve, "Incremental sheet forming of composite material", *Materials Today: Proceedings*, vol. 63, pp. 176–184, 2022.

[179] F. Tanasa and M. Zanoaga, "Fiber-reinforced polymer composites as structural materials for aeronautics", *in Proceedings of the International Conference of Scientific Paper, Brasov, 23–25 May 2013*, 2013.

[180] G. Marsh, “Airbus takes on boeing with reinforced plastic a350 xwb”, *Reinforced plastics*, vol. 51, *11*, pp. 26–29, 2007.

[181] A. K. Sharma, R. Bhandari, A. Aherwar, and R. Rimašauskienė, “Matrix materials used in composites: a comprehensive study”, *Materials Today: Proceedings*, vol. 21, pp. 1559–1562, 2020.

[182] D. H. Kim, Y. S. Lee, and Y. Son, “Anomalous rheological behavior of long glass fiber reinforced polypropylene”, *Korea-Australia rheology journal*, vol. 24, *4*, pp. 307–312, 2012.

[183] T. Kuboki, Y. H. Lee, C. B. Park, and M. Sain, “Mechanical properties and foaming behavior of cellulose fiber reinforced high-density polyethylene composites”, *Polymer Engineering & Science*, vol. 49, *11*, pp. 2179–2188, 2009.

[184] J. Markarian, “Long fibre reinforcement drives automotive market forward”, *Plastics, Additives and Compounding*, vol. 7, *3*, pp. 24–29, 2005.

[185] B. Deng, Y. Shi, T. Yu, C. Kang, and P. Zhao, “Multi-response parameter interval sensitivity and optimization for the composite tape winding process”, *Materials*, vol. 11, *2*, p. 220, 2018.

[186] R. Akkerman and S. Haanappel, “Thermoplastic composites manufacturing by thermoforming”, *in Advances in Composites Manufacturing and Process Design*, Elsevier, 2015, pp. 111–129.

[187] R. W. Ogden, “Large deformation isotropic elasticity–on the correlation of theory and experiment for incompressible rubberlike solids”, *Proceedings of the Royal Society of London. A. Mathematical and Physical Sciences*, vol. 326, *1567*, pp. 565–584, 1972.

[188] J. Reis, L. Pacheco, and H. da Costa Mattos, “Tensile behavior of post-consumer recycled high-density polyethylene at different strain rates”, *Polymer testing*, vol. 32, *2*, pp. 338–342, 2013.

[189] P. K. Dutta, “Low-temperature compressive strength of glass-fiber-reinforced polymer composites”, 1994.

[190] *Thermoset composites market size and forecast*, 2023. [Online]. Available: `https://www.verifiedmarketresearch.com/product/thermoset-composites-market/`.

[191] L. Yang, V. Shim, and C. Lim, “A visco-hyperelastic approach to modelling the constitutive behaviour of rubber”, *International Journal of Impact Engineering*, vol. 24, *6-7*, pp. 545–560, 2000.

[192] X. Chen, Y. Li, Z. Zhi, Y. Guo, and N. Ouyang, “The compressive and tensile behavior of a 0/90 c fiber woven composite at high strain rates”, *Carbon*, vol. 61, pp. 97–104, 2013.

[193] J. Múgica, L. Aretxabaleta, I. Ulacia, and J. Aurrekoetxea, “Rate-dependent phenomenological model for self-reinforced polymers”, *Composites Part A: Applied Science and Manufacturing*, vol. 84, pp. 96–102, 2016.

[194] B. ISO *et al.*, “Plastics–determination of tensile properties”, *British Standard, Germany*, 1997.

[195] G. Vyas, S. Pinho, and P. Robinson, “Constitutive modelling of fibre-reinforced composites with unidirectional plies using a plasticity-based approach”, *Composites Science and Technology*, vol. 71, *8*, pp. 1068–1074, 2011.

[196] O. Atmani, F. Abbès, Y. Li, S. Batkam, and B. Abbès, “Experimental and numerical investigation of the effects of sheet material, plug-assist tool material, and process conditions on the mechanical pre-stretching stage of plug-assist thermoforming”, *The International Journal of Advanced Manufacturing Technology*, vol. 122, *7-8*, pp. 3217–3234, 2022.

[197] P. Duffo, B. Monasse, J. Haudin, C. G’sell, and A. Dahoun, “Rheology of polypropylene in the solid state”, *Journal of materials science*, vol. 30, pp. 701–711, 1995.

[198] A. Greco, R. Gennaro, and A. Maffezzoli, “Thermoforming of thermoplastics matrix composites”, *Wiley Encyclopedia of Composites*, pp. 1–15, 2011.

[199] S. Mortazavian and A. Fatemi, “Tensile behavior and modeling of short fiber-reinforced polymer composites including temperature and strain rate effects”, *Journal of Thermoplastic Composite Materials*, vol. 30, *10*, pp. 1414–1437, 2017.

[200] D. Lopez, S. Thuillier, and Y. Grohens, “Prediction of elastic anisotropic thermo-dependent properties of discontinuous fiber-reinforced composites”, *Journal of Composite Materials*, vol. 54, *14*, pp. 1913–1923, 2020.

[201] Z. Zhai, C. Groeschel, and D. Drummer, “Tensile behavior of quasi-unidirectional glass fiber/polypropylene composites at room and elevated temperatures”, *Polymer Testing*, vol. 54, pp. 126–133, 2016.

[202] A. Schug, J. Winkelbauer, R. Hinterhölzl, and K. Drechsler, “Thermoforming of glass fibre reinforced polypropylene: a study on the influence of different process parameters”, *in AIP Conference Proceedings*, AIP Publishing LLC, vol. 1896, 2017, p. 030 010.

[203] F. Torres and S. Bush, “Sheet extrusion and thermoforming of discrete long glass fibre reinforced polypropylene”, *Composites Part A: Applied Science and Manufacturing*, vol. 31, *12*, pp. 1289–1294, 2000.

[204] S. Lin and J. Ding, “Experimental study of the plastic yielding of rolled sheet metals with the cruciform plate specimen”, *International journal of plasticity*, vol. 11, *5*, pp. 583–604, 1995.

[205] R. Emami, M. J. Mirnia, M. Elyasi, and A. Zolfaghari, “An experimental investigation into single point incremental forming of glass fiber-reinforced polyamide sheet with different fiber orientations and volume fractions at elevated temperatures”, *Journal of Thermoplastic Composite Materials*, vol. 36, *5*, pp. 1893–1917, 2023.

[206] A. Formisano, L. Boccarusso, and M. Durante, “Optimization of single-point incremental forming of polymer sheets through fem”, *Materials*, vol. 16, *1*, p. 451, 2023.

[207] T. Trzepieciński, B. Krasowski, A. Kubit, and D. Wydrzyński, “Possibilities of application of incremental sheet-forming technique in aircraft industry”, *Advances in Mechanical and Materials Engineering*, vol. 35, *298 (1)*, pp. 87–100, 2018.

[208] D. H. Nimbalkar and V. Nandedkar, “Review of incremental forming of sheet metal components”, *Int J Eng Res Appl*, vol. 3, *5*, pp. 39–51, 2013.

[209] K. Protchenko, F. Zayoud, M. Urbański, and E. Szmigiera, “Tensile and shear testing of basalt fiber reinforced polymer (bfrp) and hybrid basalt/carbon fiber reinforced polymer (hfrp) bars”, *Materials*, vol. 13, *24*, p. 5839, 2020.

[210] J. H. Affdl and J. Kardos, “The halpin-tsai equations: a review”, *Polymer Engineering & Science*, vol. 16, *5*, pp. 344–352, 1976.

[211] Z. Xu, X. Shao, and Q. Huang, “A micromechanical model of multi-scale nano-reinforced composites”, *Polymer Testing*, p. 108 121, 2023.

[212] M.-m. Xu, G.-y. Huang, S.-s. Feng, G. J. McShane, and W. J. Stronge, “Static and dynamic properties of semi-crystalline polyethylene”, *Polymers*, vol. 8, *4*, p. 77, 2016.

[213] M. Machado, M. Fischlschweiger, and Z. Major, “A rate-dependent non-orthogonal constitutive model for describing shear behaviour of woven reinforced thermoplastic composites”, *Composites Part A: Applied Science and Manufacturing*, vol. 80, pp. 194–203, 2016.

[214] K. Ho and E. Krempl, “Extension of the viscoplasticity theory based on overstress (vbo) to capture non-standard rate dependence in solids”, *International Journal of Plasticity*, vol. 18, *7*, pp. 851–872, 2002.

[215] A. A. Skandani and M. Al-Haik, “Viscoplastic characterization and modeling of hybrid carbon fiber/carbon nanotubes reinforced composites”, *Composites Part B: Engineering*, vol. 99, pp. 63–74, 2016.

[216] R. Edwards, G. Coles, and W. Sharpe, “Comparison of tensile and bulge tests for thin-film silicon nitride”, *Experimental Mechanics*, vol. 44, pp. 49–54, 2004.

[217] E. Guades, T. Aravinthan, and M. M. Islam, “Characterisation of the mechanical properties of pultruded fibre-reinforced polymer tube”, *Materials & Design*, vol. 63, pp. 305–315, 2014.

[218] M. Barral, G. Chatzigeorgiou, F. Meraghni, and R. Léon, “Homogenization using modified mori-tanaka and tfa framework for elastoplastic-viscoelastic-viscoplastic composites: theory and numerical validation”, *International Journal of Plasticity*, vol. 127, p. 102 632, 2020.

[219] H. Uematsu, Y. Suzuki, Y. Iemoto, and S. Tanoue, “Effect of maleic anhydride-grafted polypropylene on the flow orientation of short glass fiber in molten polypropylene and on tensile properties of composites”, *Advances in Polymer Technology*, vol. 37, *6*, pp. 1755–1763, 2018.

COLLEGE
DOCTORAL SCIENCES
BRETAGNE POUR L'INGENIEUR

INSA INSTITUT NATIONAL
DES SCIENCES
APPLIQUÉES
RENNES

Titre : Caractérisation du comportement thermo-viscoplastique d'un thermoplastique renforcé soumis à un chargement biaxial plan : application au formage incrémental à chaud

Mot clés : Thermoplastiques renforcés, chargement biaxial plan, effet de la température et de la vitesse de déformation, modélisation numérique, caractérisation expérimentale, mise en forme à chaud

Résumé : Les thermoplastiques renforcés par des fibres présentent de bonnes propriétés mécaniques et une bonne aptitude à la recyclabilité. Néanmoins, la mise en forme de pièces complexes reste difficile. La mise en forme à chaud de ces matériaux est essentielle. La simulation par éléments finis des procédés est indispensable mais nécessite une caractérisation précise du matériau sous conditions réelles : chargement multiaxial avec grandes déformations, conditions variées de température et de vitesse de déformation. Les essais uniaxiaux classiques sont simples mais peuvent conduire à une caractérisation partielle du matériau sous chargement multiaxial. Les essais de traction biaxiale plane sur éprouvettes cruciformes permettent une caractérisation plus riche. Ce travail vise à caractériser le comportement mécanique d'un polypropylène renforcé de fibres de verre discontinues pour différentes températures et vitesses de déformation. Le modèle modifié de G'Sell et Jonas, associé au critère anisotrope de Hill48, est calibré à partir d'essais de traction uniaxiale pour diverses conditions de température (jusqu'à 120°C) et de vitesse de déformation (jusqu'à 10 s^{-1}). Les simulations numériques de l'essai biaxial, réalisées à partir d'un modèle de comportement calibré à partir des essais uniaxiaux, montrent un écart important avec les résultats expérimentaux. Il est donc nécessaire d'intégrer les résultats biaxiaux dans la procédure d'identification des paramètres rhéologiques du matériau, à partir d'une procédure d'analyse inverse. Finalement, les deux méthodes d'identification sont évaluées à partir de la prédiction des efforts de formage et de la forme finale d'une pièce formée par un procédé incrémental à chaud original.

Title: Characterization of the thermo-viscoplastic behavior of a reinforced thermoplastic subjected to in-plane biaxial loading: application to heat assisted incremental forming

Keywords: Reinforced thermoplastics, in-plane biaxial loading, temperature and strain rate dependence, numerical modeling, experimental characterization, heat assisted forming

Abstract: Fiber reinforced thermoplastics offer good mechanical properties and the ability to be recycled. However, shaping complex parts remains challenging. Hot forming of these materials is crucial. Finite element simulation of processes is essential, but it requires accurate characterisation of materials under real conditions: multiaxial loading with large deformations, varying temperature, and strain rates. Conventional uniaxial tests are simple but may lead to partial material characterization under multiaxial loading. In-plane biaxial tensile tests on cruciform specimens allow for a more comprehensive characterization. This work aims to characterize the mechanical behavior of discontinuous glass fiber reinforced polypropylene at different temperatures and strain rates. The modified G'Sell and Jonas model, coupled with the anisotropic Hill48 criterion, is calibrated based on uniaxial tensile tests under various temperature conditions (up to 120°C) and deformation speeds (up to 10 s^{-1}). Numerical simulations of the biaxial test, carried out using a behavior model calibrated from uniaxial tests, show a significant disagreement with the experimental results. Therefore, it is necessary to integrate biaxial results into the material's rheological parameter identification procedure through an inverse analysis process. Finally, both identification methods are evaluated based on the prediction of forming force and final geometry of a part formed using an original heat assisted forming process.